OUKA
Osaka University Knowledge Archive

Title	Study on the mechanism of protein aggregation based on new macroscopic views
Author(s)	Lin, Yuxi
Citation	大阪大学, 2017, 博士論文
Version Type	VoR
URL	https://doi.org/10.18910/61502
rights	
Note	

Osaka University Knowledge Archive : OUKA

https://ir.library.osaka-u.ac.jp/

Osaka University

Study on the mechanism of protein aggregation based on new macroscopic views

(新しい巨視的な観点に基づく蛋白質凝集の機構に関する研究)

A Doctoral Thesis

by

Yuxi Lin

Submitted to the Graduate School of Science

Osaka University

February, 2017

Acknowledgement

I would like to express my truly appreciation to Professor Yuji Goto (Osaka University). The enthusiasm that he has for his research was impressive and motivational for me. I still remembered those days in which he and I read the book entitled “The Protein Molecule” together, written by Professor Kozo Hamaguchi, for improving my background knowledge. I give my heartfelt thanks to his invaluable comments and enormous support throughout this process.

I am deeply indebted to Associate Professor Young-Ho Lee (Osaka University) for his nonstop contribution of time, ideas and advice to make my study more productive and stimulating. His motivation, enthusiasm and hard working for his research deeply inspired me to tackle and overcome any challenges in this whole process. I greatly appreciate his trust in me, providing me the opportunity to try everything and develop wide knowledge in Osaka University

I would like to thank Professors Katsumi Imada (Osaka University) and Hiroyasu Yamaguchi (Osaka University) for their accepting this dissertation.

I would like to express my great appreciation to Associate Professor Jozsef Kárdos (Eötvös Loránd University) for his valuable discussion and experimental support, and to Associate Professor Kazumasa Sakurai (Kinki Univeristy) and Assistant Professor Hisashi Yagi (Tottori University) for their helpful advice. I am also sincerely grateful to Dr. Yuichi Yoshimura (Hiroshima University), who taught me not only the way to conduct experiments, but also Japanese, and to Assistant Professor Masatomo So (Osaka University), Dr. Mayu Terakawa (Cornell University), Dr. Tatsuya Ikenoue (University of Cambridge) and Mr. Misaki Kinoshita (Osaka University) for helping my experiments and sharing their experience, and to Ms. Kyoko Kigawa for the assistances of protein expression and purification.

I would additionally acknowledge other past and present members of the Laboratory of Protein Folding for their plentiful suggestions and warmhearted accompany. They are very helpful to

color my life and make my life go smoothly in Osaka.

Special thanks are given to the Global 30 Program of Osaka University and the Research Fellowships of the Japan Society for the Promotion of Science for Young Scientists, which provided me a rare opportunity and platform to study in Japan.

Last, but certainly not the least, I owe more than thanks to my family members-Mom, Dad and my girlfriend Yan. Your unconditional support, encouragement and love lift me up and carry me forward throughout this whole process. To Yan, I'm so blessed to have you, and can't wait to see what's in the next chapter of our life. To Mom and Dad, thank you for the freedom that you have given me, which let me pursue what I love and interest in my life path. No words can express my honor for having you as my parents. Nothing but gratitude and respect.

Yuxi Lin

February 2017

Contents

Abbreviations

AFM	atomic force microscopy
Ag-apoCyt*c*	silver-bound apocytochrome *c*
ApoCyt*c*	apo cytochrome *c*
CD	circular dichroism
CMC	critical micelle concentration
Cyt*c*	cytochrome *c*
DTT	dithiothreitol
FTIR	fourier-transform infrared
HFIP	1,1,1,3,3,3-hexafluoro-2-propanol
HPLC	high-performance liquid chromatography
HoloCyt*c*	holo cytochrome *c*
ITC	isothermal titration calorimetry
NMR	nuclear magnetic resonance
SDS	sodium dodecyl sulfate
ThT	thioflavin T
TFE	2,2,2- trifluoroethanol

Chapter 1. General introduction

1-1. Protein folding and aggregation

The process by which an unstructured polypeptide chain forms a unique three-dimensional native structure is called protein folding. In the early 1960s, C.B. Anfinsen investigated the renaturation of ribonuclease A and proposed a well-known postulate, "Anfinsen's dogma".[1] This hypothesis stated that a native protein adopt the most thermodynamically stable structure according to its amino acid sequence. Since protein folding is a critical step for intrinsic functions of proteins, extensive studies on the molecular mechanism of protein folding have been carried out over the past several decades.

Meanwhile, it has been demonstrated that a lot of factors such as mutations and alternations in environmental conditions cause errors in protein folding, which often results in misfolded structures of proteins. Misfolded proteins have a high tendency to form aggregates. Protein aggregates may be largely classified two types based on their morphology and structure, amyloid fibrils and amorphous aggregates. Amyloid fibrils are highly-ordered aggregates and defined by their fibrillar morphology and structure (Figure 1A). They have received much more attention than amorphous aggregates due to relations to various diseases (Table 1). Amyloid fibrillation and the deposition of amyloid fibrils in the body have been shown to cause neurodegenerative diseases, such as Alzheimer's disease, Parkinson's disease and Huntington disease.[2, 3]

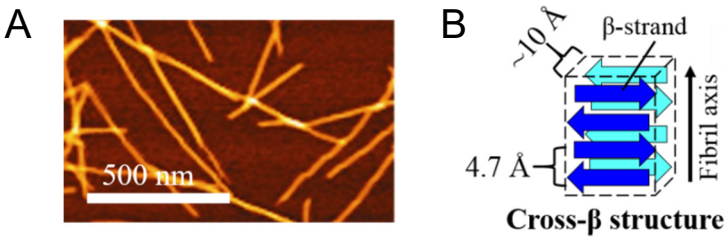

Figure 1. Conformational properties of amyloid fibrils. (A) Morphology of amyloid fibrils revealed by atomic force microscopy (AFM). White bar represents 500 nm. (B) Schematic representation of a typical cross-β structure in amyloid fibrils.

Table 1. Representative human diseases and their related proteins or peptides

Disease	Aggregating protein or peptide
Alzheimer's disease	Amyloid β peptides, Tau
Parkinson's disease	α-synuclein (wild type or mutants)
Dementia with Lewy bodies	α-synuclein (wild type or mutants)
Huntington's disease	Huntingtin
Amyotrophic lateral sclerosis	SOD1 (wild type or mutants), TDP-43 (wild type or mutants), FUS (wild type or mutants)
Frontotemporal dementia with Parkinsonism	Tau
Transthyretin amyloidosis	Transthyretin (mutants)
Transmissible spongiform encephalopathy	Prion (whole or fragments)
Type II diabetes	Amylin (fragments)
Hemodialysis-related amyloidosis	β2-microglobulin (wild type or mutants)

Interestingly, Dobson and coworkers have demonstrated that proteins which are not involved in amyloid diseases can also self-assemble into amyloid fibrils *in vitro* under certain experimental conditions, suggesting the formation of amyloid fibrils is a generic property of proteins.[2, 4] Recently, a variety of computational algorithms have been developed to predict the aggregation and amyloid propensity of proteins based on their primary sequence.[5-13] An insightful study among them, ZipperDB, proposed that all proteins contain potential segments of amyloidogenesis, although this is not evidenced by direct experiments in a systematical way.[14]

One more interesting point is that amyloidoigenic proteins and peptides are distinct in their primary sequence, structure and function; however amyloid fibrils formed all share the common characteristics as follows.[4, 15] First, amyloid fibrils can be stained with the fluorescence dyes such as Congo red and thioflavin T (ThT), which provides a useful and convenient way to detect and monitor amyloid formation in real-time using spectroscopic methods (Figure. 2). Second, amyloid fibrils show a hierarchical structure. Mature amyloid fibrils consist of bundles of several protofilaments.[16] A protofilament is further composed of ß-strands which are stabilized by hydrogen bonds and running

perpendicular to the fibril long axis, and therefore ß-sheet lies parallel to fibril axis, so to speak a cross-ß structure. X-ray fibril diffraction indicates that the inter-strand and inter-sheet spacing are 4.8 Å and 10 Å, respectively (Figure 1B).[2, 15, 17, 18]

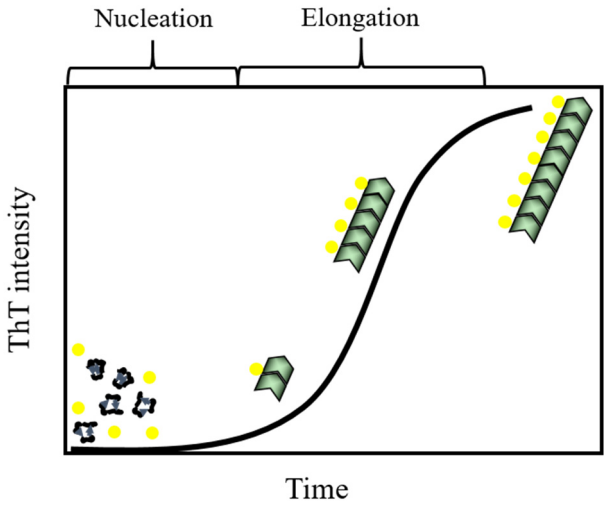

Figure 2. ThT-based observation of amyloid fibrillation process. ThT, shown as yellow circles, can bind to amyloid fibrils and thereby emitting fluorescence. A typical fibrillation process of two steps is depicted: nucleation and subsequent fibril elongation.

High stability and mechanical stiffness, as a result of the extensive hydrogen bond network in the tightly packed β-sheet structure, make amyloid fibers very attractive for a variety of applications in nanotechnology and biotechnology including the development of drug delivery system and scaffolding cell tissue.[19] Studies by Mezzenga and colleagues have practically highlighted the possible application and usage of amyloid fibrils by hybridizing amyloid fibrils with carbon-nanomaterials. Hybridized amyloid fibrils indeed showed high potency for water purification[20] and biosensors.[21] In addition, amyloid fibrils have shown biologically-beneficial roles, i.e., functional amyloids.[2, 22-24] For example, Pmel17, deposited as fibrillar structure *in vivo*, play a key role in regulating mammalian skin pigmentation.[22]

The underlying mechanisms of amyloid fibrillation have been revealed. Amyloid fibrils

formed via two sequential processes, i.e., spontaneous amyloid formation or seed-independent amyloid formation[4, 15] (Figure. 2) although much still remains to understand the detailed molecular and mechanical mechanism of amyloid formation. Rapid fibril growth phases appear following a lag time during which productive nuclei for amyloidogenesis formed. Therefore, the addition of preformed amyloid fibrils as a seed skips the rate-limit step of nucleation and exhibits generally elongation phases, i.e., seeded amyloid formation or seed-dependent amyloid formation. As nuclei are kinetically and thermodynamically unstable, their life span is very short, which hampers detailed investigation of the mechanism of nucleation and the structure of nuclei. Nuclei have been considered to be templates for amyloid fibrillation, which may determine types of amyloid fibrils.[25] Nucleation may be susceptible to ambient conditions. Thus, distinct types of nuclei formed depending on distinct conditions may produce polymorphic characters of amyloidogenesis.

Compared with amyloid fibrils, amorphous aggregates lack well-defined ordered structure. They often show spherical morphologies without characteristic secondary structures although recent studies have shown the presence of secondary structures in amorphous aggregates.[26] In the pharmaceutical industry, control of amorphous aggregates is a major task for purification and manufacture of therapeutic protein products.[27] Amorphous aggregation is also responsible for diseases such as amorphous aggregates of α-crystallin for cataracts[28] and for the problem in the immune system. In contrast to deleterious effects of amorphous aggregation, amorphous aggregates serve usefully as an initiator for the immune system.[29]

Amorphous aggregation and amyloid fibrillation have been distinguished by the kinetics of their formation.[30] Amyloid fibril formation occurs through nucleation-dependent process with a lag phase and growth phase as mentioned above while amorphous aggregates form rapidly without an appreciable lag phase due probable to tremendous heterogeneous nucleation. Thus, amorphous aggregation does not show seed-dependent kinetics.

Although unified terminology of protein aggregation is still required, investigation and characterization of each type of protein aggregates as well as their comparison are challenging and important for our deeper understanding of protein science and for providing basis and hint for prevention and cure of protein aggregation-related diseases.

1-2. Effects of alcohols on protein aggregations

Alcohols are moderately hydrophobic solvents useful for addressing the role of water in the conformation and stability of proteins. Previous studies demonstrated that alcohols can denature the rigid native structure of proteins and stabilize α-helical conformations by strengthening the local hydrogen bonds and weakening intermolecular hydrophobic interaction due mainly to the decreases in the polarity of the solvent relative to pure aqueous solution.[31-35] Moreover, two types of highly fluorinated alcohols, 2,2,2-trifluoroethanol (TFE) and 1,1,1,3,3,3-hexafluoro-2-propanol (HFIP), exhibit marked alcohol effects as a result of their dynamic cluster formation.[34, 36] Alcohols often cause protein precipitation at neutral pH by decreasing solubility of proteins. For example, ethanol-induced aggregation and precipitation have been well applied to generate functional therapeutic products by fractionating plasma proteins.[37, 38]

Since alcohols are convenient aggregation-inducing media which are compatible with a variety of biophysical techniques, alcohol-mediated formation of amyloid fibrils, particularly by TFE [39-50] and HFIP[36, 41, 49, 51], has been extensively examined for the last decade. Among them, Yamaguchi et al. explored details on alcohol effects on amyloid fibrillation. They revealed that amyloid formation of K3 fragment of β2-microglobulin (β2m) showed a bell-shaped dependence on the TFE concentration, which was simply induced by the decrease in hydrophobic interactions and the increase in polar interactions between amino acid residues in the peptide with increasing TFE concentration.[41] A similar mechanism was also applied to describe the bell-shaped dependence of islet amyloid polypeptide fibrillation on the concentration of HFIP.[36] In addition to the ability to regulate protein aggregation behavior, TFE and HFIP induce the structural polymorphism of amyloid fibrils. β2m monomers polymerized into amyloid fibrils with distinct structures in a concentration-dependent manner in the presence of TFE.[47] Assembly of peptide-naphthalenediimides conjugates in the absence

and presence of alcohols displayed the different handedness and morphology, which in turn led to the alternation in the assembly-dependent device functionality.[52-54]

Although extensive studies have been performed to elucidate the mechanism of alcohol-induced amyloid fibrillation, the linkage between an alcohol-induced decrease in solubility and amyloidgenesis has not been revealed. Furthermore, there is still no systematic investigation on the effects of TFE and HFIP on protein solubility and amyloidogenesis. Therefore, the study on alcohol-induced protein aggregation in terms of solubility will provide us with deeper understanding on the underlying mechanism of protein aggregation.

1-3. Effects of ultrasonication on protein aggregations

Ultrasonication has been commonly used for preparing fibril seeds. It breaks long fibrils into short fibrils with narrow distributions of the fibril length, leading to the dramatic increase in the number of active fibril ends where monomers are incorporated for fibril elongation.[55] It has been generally accepted that seeded amyloid formation provided more homogeneous amyloid fibrils than spontaneous amyloid formation based on kinetic adaptation of amyloid fibrillation in nature. Moreover, ultrasonication-treated short and homogeneous fibrils provided a chance to characterize overall structures of amyloid fibrils at the residue level using solution-state nuclear magnetic resonance (NMR) spectroscopy. β2m amyloid fibrils were largely characterized by flexible unstructured regions which were exposed to solution and rigid core regions which were buried and protected from solution.[56]

Recent studies showed that ultrasonication is a highly efficient agitation for generating amyloid fibrils.[57-60] Stathopulos and coworkers first proved that ultrasonication caused the formation of amyloid-like aggregates of various proteins.[57] Oohashi and colleagues next showed that ultrasonication promoted the structural conversion of β2m from monomers to fibrils.[58] The remarkable accelerating effect was mainly ascribed to ultrasonication-induced continuous growth and collapse of cavitation microbubbles,[61, 62] which induces the denaturation and condensation of proteins on the water-air interface of microbubbles. In addition, ultrasonication also generates large shearing force due to the solvent flow,[63-65] which favors the growth of amyloid fibrils through the secondary nucleation.

Recently, Yoshimura et al. has proposed that the formation of amyloid fibrils is analogous to protein crystallization occurred in a supersaturated solution. Accordingly, accelerated fibril formation is simply explained by ultrasonication-induced disruption of supersaturation.[30] In contrast, the kinetics

of amorphous aggregation do not depend on ultrasonication treatment. Thus, it was viewed that amyloid fibrillation and amorphous aggregation can be simply distinguished by their kinetics of formation. Overall, ultrasonciation, which disrupts persistant supersaturation, is an effective method to elucidate the real aggregation propensity and to compare different types of protein aggregation.

1-4. Content of this thesis

Recent progress in elucidating protein aggregation from microscopic viewpoints has revealed that subtle changes in molecular interactions can lead to two morphologically distinct aggregates, amyloid fibril and amorphous aggregate. However, the detailed mechanism how proteins can form these two types of aggregates based on macroscopic viewpoints is still unclear.

In chapter 2, I studied the alcohol-induced fibrillation of hen egg-white lysozyme at various concentrations of ethanol, TFE, and HFIP. Under the conditions where the alcohol-denatured lysozyme retained metastability, ultrasonication effectively triggered fibrillation. The optimal alcohol concentration depended on the alcohol species. HFIP showed a sharp maximum at 12-16%. For TFE, a broad maximum at 40-80% was observed. Ethanol exhibited only an increase of fibrillation above 60%. These profiles were opposite to the equilibrium solubility of lysozyme in water/alcohol mixtures. I proposed an alcohol-dependent protein misfolding funnel useful for describing protein aggregation.

In chapter 3, the aggregation behavior of the physiologically relevant two types of cytochrome *c* (Cyt*c*), metal-bound Cyt*c*, and its fragment with high amyloidogenicity as predicted in alcohol/water mixtures was examined. Based on the results, I addressed the biological implications of Cyt*c* aggregation based on the physiologically relevant and distinct conformational states of holo and apo Cyt*c*. The aggregation of Cyt*c* and its fragment has also been discussed in terms of metastability and the degree of supersaturation. I proposed that a phase diagram constructed by a macroscopic view of thermodynamic solubility with the incorporation of a microscopic view of the secondary structure content of monomers and aggregates is useful for understanding the aggregation behaviors of proteins.

In chapter 4, I will summarize the contents of my thesis to provide general conclusions.

Chapter 2. Solubility and supersaturation-dependent protein aggregation revealed by ultrasonication

2-1. Introduction

In the last decade, alcohol-induced formation of protein aggregates, particularly by TFE[40-49, 66] and HFIP,[36, 41, 49] has been focused on. It is noted that these alcohols not only promote fibrillation, but also induce amorphous aggregation of proteins,[34, 41] arguing that amyloid fibrillation and amorphous aggregation share a common mechanism, although they are distinct in their morphologies (Figure 1, Chapter 1).

Recent study revealed that amyloid fibrillation and amorphous aggregation are similar to the crystallization and glass formation of solutes, respectively, at concentrations above the solubility limit (i.e., critical concentration).[30, 36] When its concentration is above solubility, a solute is excluded from the solution, often precipitating as crystals. However, a high free energy barrier of crystallization retains supersaturation.[67, 68] In the metastable region of supersaturation, spontaneous nucleation does not occur and seeding is required for crystallization. In the labile region, spontaneous nucleation can occur after a certain lag time producing crystals. A further increase in the driving forces of precipitation causes glass transition producing glass. Although there is no considering of the supersaturation, the fibrillation above the solubility limit is similar to the helical polymerization model proposed by Oosawa and Kasai,[69] in which the equilibrium constant between monomers and helical aggregates is the critical concentration.

Analogies of crystallization and amyloid fibrillation[30, 36, 70, 71] suggest that alcohol-dependent amyloid fibrillation can be understood by the decreased solubility of polypeptides in alcohol/water mixtures. Although a decrease in protein solubility in alcohol/water or SDS/water mixtures was reported for lysozyme,[72] prion proteins,[73] and RNase Sa,[74] a linkage between the decreased solubility and amyloidogenicity has not been systematically argued. As far as I know, there is no report on the effects of TFE and HFIP on the solubility of peptides or proteins. In this study with hen egg-white

lysozyme, I examined the role of solubility and supersaturation in alcohol-dependent amyloid fibrillation. To verify supersaturation, I used ultrasonication, one of the most effective agitations for abolishing metastability and thus effectively producing amyloid fibrils.[30, 58, 59, 75, 76] The results show that amyloid fibrillation of lysozyme is largely determined by the equilibrium solubility, often difficult to achieve because of the metastability of supersaturation.

2-2. Materials and Methods

Materials. ThT was obtained from Wako Pure Chemical Industries, Ltd. Ethanol, TFE, HFIP and other reagents were obtained from Nacalai Tesque (Kyoto, Japan). Hen egg-white lysozyme was purchased from Nacalai Tesque (Kyoto, Japan) and used without further purification.

Sample preparation of hen egg-white lysozyme. Lysozyme was dissolved in 250 mM sodium acetate buffer (pH 4.8) at 15, 50 and 100 mg mL^{-1}. Then, the protein solutions were diluted with alcohols to desired alcohol concentrations with a final acetate buffer concentration of 25 mM. Although alcohols increased the pH because of their hydrophobicity, I did not adjust the pH. The apparent pH in 10% ethanol, TFE, and HFIP was all 4.8, and in 50% ethanol, TFE, and HFIP, was 5.7, 5.0, and 5.2, respectively. It should be noted that alcohol concentrations in this paper are (volume/volume) percentages. I also examined the effects of the order of sample preparation by initially dissolving the lyophilized lysozyme directly into 90% TFE and then decreasing the TFE concentration by dilution. The concentration of lysozyme was determined spectrophotometrically by using absorbance at 280 nm with an extinction coefficient of 2.63 mL mg^{-1} cm^{-1}.[77] The final concentrations of lysozyme used were 1.5, 5, and 10 mg mL^{-1}. Unless otherwise mentioned, the lysozyme concentration was 1.5 mg mL^{-1}.

Real-time monitoring of aggregation with and without agitation. The protein solutions with a total volume of 1.5 mL, containing 1.5 mg mL^{-1} or 5 mg mL^{-1} lysozyme, 5 μM ThT, and alcohol at various concentrations, were incubated in a 1-cm light path cuvette at 25 ºC in the absence and presence of agitation. Cuvettes were sealed tightly to prevent volatilization of alcohols, and firmly fixed in the spectrophotometer. ThT fluorescence and light scattering were measured using a Hitachi fluorescence spectrophotometer F4500 (Hitachi, Tokyo, Japan) with the excitation wavelengths at 445 nm and 350 nm, respectively. The lag time for aggregation was defined as the time at which the ThT

fluorescence or light scattering intensity reaches one-tenth of the maximum. Two types of agitation (i.e. stirring and ultrasonication) were employed. For agitation with a stirring magnet, the stirring speed was set at 600 rpm. For agitation with ultrasonic irradiation, the sample solution was irradiated with ultrasonic pulses by tightly attaching an ultrasonic generator (Elekon, Tokyo, Japan) to a sidewall of the cuvette as described previously.[30] Ultrasonic agitation was combined with continuous stirring with a magnet at 600 rpm and subjected to cycles of ultrasonication for 1 min at 2-min intervals. The frequency of the ultrasonic waves was 27.5 kHz. The aggregation processes agitated with stirring in the absence and presence of 5% (w/w) seed fibrils were also examined using a Hitachi F4500 fluorescence spectrophotometer. Fibril seeds, i.e. short lysozyme fibrils, were prepared by fragmentation of mature fibrils with manual sonication treatment.

Real-time monitoring of aggregation with microplate. Lysozyme at 10 mg mL^{-1} dissolved in 25 mM sodium acetate buffer (pH 4.8) containing alcohols at various concentrations (0-90%) was applied to each of the 96 wells of a microplate. Using the method established in our previous study,[75] the microplate placed at the center of a water bath-type ultrasonic transmitter (ELESTEIN SP070-PG-M; Elekon, Tokyo, Japan) was ultrasonicated from three directions. The microplate was subjected to cycles of ultrasonication for 1 min at 9-min intervals, and maintained at 25 °C throughout the experiment. The power and output of the sonication were set to 17–20 kHz and 350 W, respectively. Before and after 48 h incubation, a 1-μl aliquot of sample was added to 200 μL of a 50 mM glycine-NaOH buffer (pH 8.5) containing ThT at a final concentration of 5 μM, and the fluorescence intensity at 490 nm was measured with an excitation wavelength of 445 nm.

ThT assay at neutral pH. Aliquots (5 μL) of the sample solutions after reactions at pH 4.8 were added to 1 mL of the 50 mM glycine-NaOH buffer (pH 8.5) containing 5 μM ThT. Fibril formation was assayed based on the ThT intensity at 480 nm excited at 445 nm using a Hitachi F7000 fluorescence spectrophotometer.

Circular dichroism (CD) measurements. CD measurements of lysozyme solutions were performed at 0.15 mg mL^{-1} in 25 mM sodium acetate buffer (pH 4.8) containing various alcohol concentrations using a Jasco J820 spectropolarimeter at 25 ºC. The sample solution (1.5 mg mL^{-1}) was diluted 10 fold for far-UV CD experiments. Far-UV CD spectra were recorded using a quartz cuvette of 1-mm path length. The spectra were expressed as mean residue ellipticity, [θ] (deg cm^2 $dmol^{-1}$), after subtracting the solvent background.

Determination of concentrations of residual monomers. The sample solutions after reactions were centrifuged at 15,000 rpm and at 25 ºC for 30 min. Then, the concentration of residual monomers in the supernatant was determined spectrophotometrically.[77]

AFM measurements. Sample solutions of 1.5 mg mL^{-1} lysozyme after reactions were diluted 10 fold, then a 15-μL aliquot was spotted on a freshly-cleaved mica plate. The residual solution was blown off with compressed air and air-dried after 10 seconds. AFM images were obtained using a Nano Scope IIIa (Digital Instruments) as reported previously.[30, 41]

Dynamic light scattering measurements. To examine aggregation states of soluble proteins, dynamic light scattering measurements were performed using a Zetasizer instrument (DynaPro; Wyatt Technology Corporation, USA) at 25 °C using a standard cuvette with a path length of 1 cm. Lysozyme at 1.5 mg mL^{-1} was dissolved in 25 mM sodium acetate buffer (pH 4.8), containing 40% TFE, 16% HFIP, and 65% ethanol. Scattering data were collected as an average of 20 scans collected over 200 seconds. The data were processed in accordance with the manufacturer's software (DYNAMICS; Wyatt Technology Corporation). The Stoke–Einstein relationship, together with refractive indices and temperature-corrected viscosities of water provided by the DYNAMICS software, was used to calculate the hydrodynamic radius of protein solutions.

2-3. Results

Alcohol-Induced Transitions under Quiescent Conditions

The effects of TFE, HFIP, and ethanol on hen egg-white lysozyme at 1.5 mg mL^{-1} at pH 4.8, where the pH value is in the absence of alcohol, were examined by CD spectroscopy under quiescent conditions (Figure 1-4). The spectra were measured ~5 min and 48 h after sample preparation. In the absence of alcohols, lysozyme composed of predominantly α-helical and β-sheet domains had a CD spectrum with minima at 208 and 222 nm with an ellipticity of around −10 000 deg cm^2 $dmol^{-1}$ at 222 nm (Figure 1A).

The addition of TFE caused a cooperative transition at 30−40%, producing an α-helical conformation (Figure 1A,D), consistent with previous reports.[31, 35] The effects of HFIP, showing a highly cooperative transition at 10−16%, were stronger than those of TFE (Figure 1B,D). HFIP at 8% brought about the aggregation of the solution, resulting in a decrease in the CD intensity (Figure 1B,D). The effects of ethanol were weakest among the three alcohols, causing spectral changes above 60% (Figure 1C,D). Spectral changes at higher concentrations of ethanol indicated the formation of β structures (Figure 1C, Figure 4).

Upon incubation for 48 h without agitation, no change was observed for the solutions containing TFE (Figure 1D, Figure 2). The aggregates observed in the presence of 8−12% HFIP dissolved with time (Figure 1B,D, Figure 3B−D), suggesting that the aggregation is transient. The effects of ethanol were weakest among the three alcohols causing spectral changes above 60%, suggesting the formation of β structures (Figure 1C,D). In the presence of ethanol above 70%, aggregation was accompanied by a further decrease in the far-UV CD intensity (Figure 1C,D, Figure 4C−F). The aggregates that formed under quiescent conditions were examined by ThT binding at pH 4.8 and 8.5, light scattering, and CD (Figures 1−5). The transient aggregates that formed at 8−12%

HFIP had a high light scattering intensity but no ThT fluorescence, suggesting that they are amorphous aggregates probably of the native lysozyme.

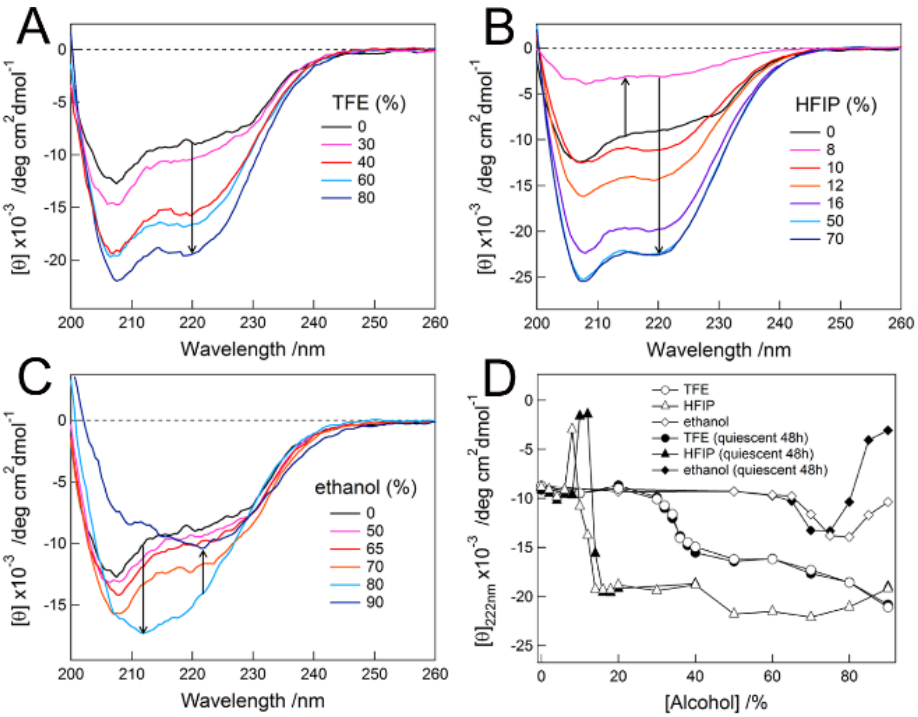

Figure 1. Alcohol-induced conformational transitions of lysozyme monitored by CD in the absence of agitation. Far-UV CD spectra of lysozyme at various concentrations of (A) TFE, (B) HFIP, and (C) ethanol. Arrows indicate increasing alcohol concentrations. The up arrows indicate the increase in ellipticity (B) from 0 to 8% HFIP and (C) from 80 to 90% ethanol. (D) Ellipticities at 222 nm obtained 5 min (○, Ä, ◊) and 48 h (●, ▲, ♦) after sample preparation plotted against TFE (○, ●), HFIP (Ä, ▲), and ethanol (◊, ♦) concentrate.

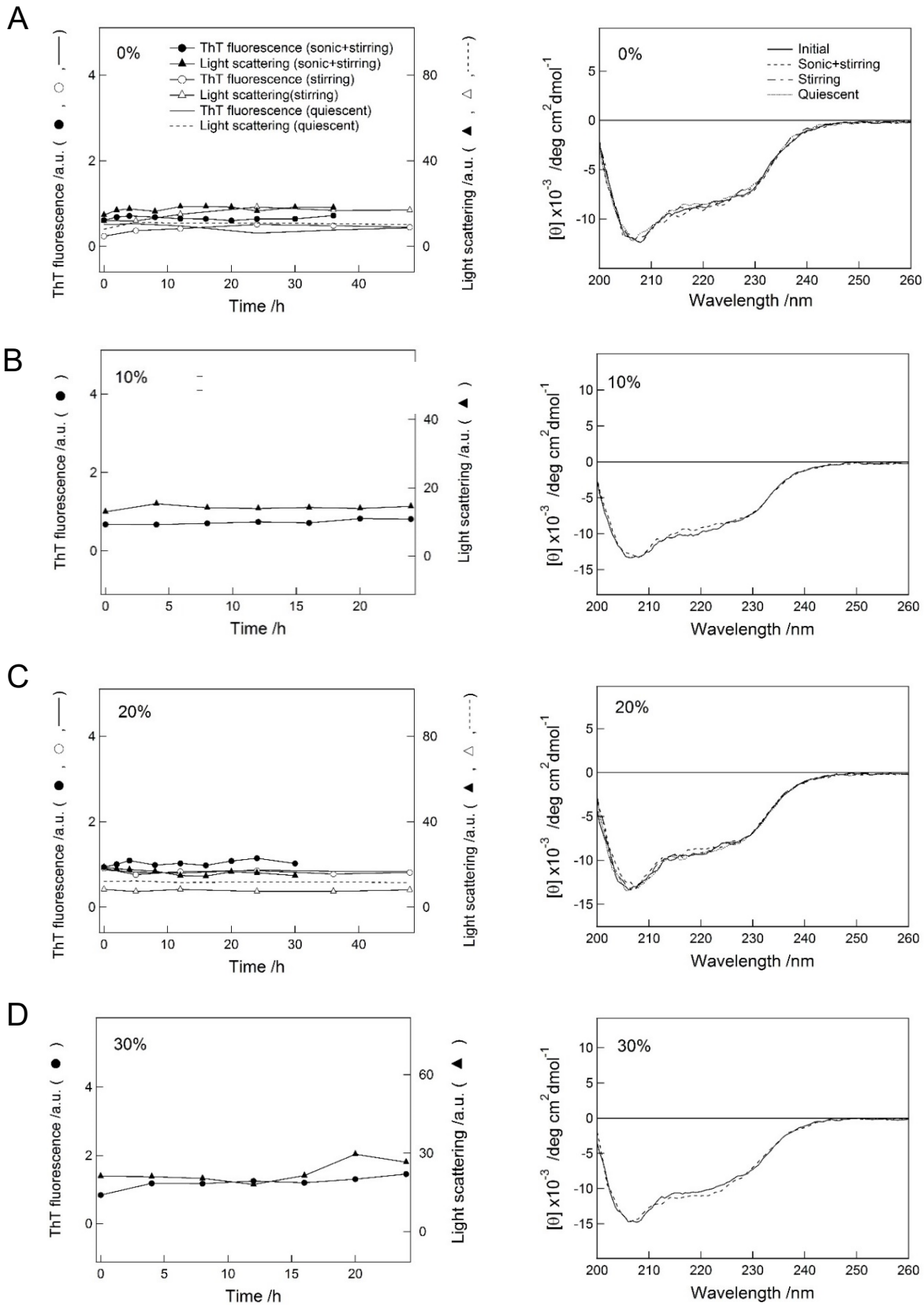
A
0%
ThT fluorescence (sonic+stirring)
Light scattering (sonic+stirring)
ThT fluorescence (stirring)
Light scattering(stirring)
ThT fluorescence (quiescent)
Light scattering (quiescent)
ThT fluorescence /a.u. (● , ○ , ——)
Light scattering /a.u. (▲ , △ , ------)
Time /h
0%
Initial
Sonic+stirring
Stirring
Quiescent
[θ] x10-3 /deg cm2dmol-1
Wavelength /nm
B
10%
ThT fluorescence /a.u. (●)
Light scattering /a.u. (▲)
Time /h
10%
[θ] x10-3 /deg cm2dmol-1
Wavelength /nm
C
20%
ThT fluorescence /a.u. (● , ○ , ——)
Light scattering /a.u. (▲ , △ , ------)
Time /h
20%
[θ] x10-3 /deg cm2dmol-1
Wavelength /nm
D
30%
ThT fluorescence /a.u. (●)
Light scattering /a.u. (▲)
Time /h
30%
[θ] x10-3 /deg cm2dmol-1
Wavelength /nm

E

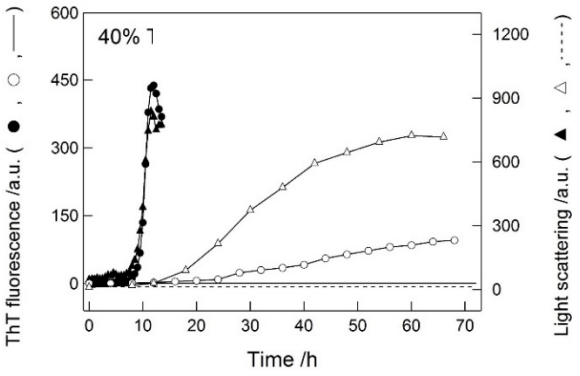
40%
ThT fluorescence /a.u. (● , ○ , ——)
Light scattering /a.u. (▲ , △ , ------)
Time /h

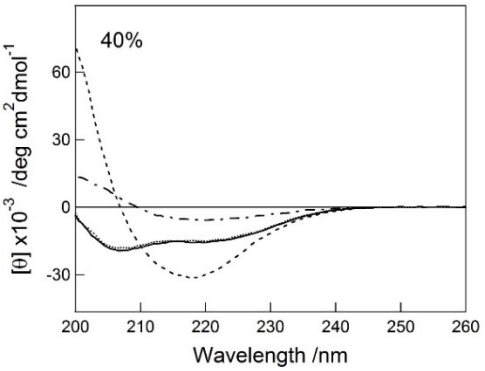
40%
[θ] x10^{-3} /deg cm^{2}dmol^{-1}
Wavelength /nm

F

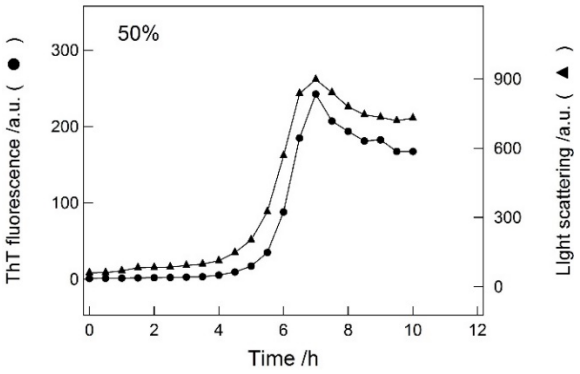
50%
ThT fluorescence /a.u. (●)
Light scattering /a.u. (▲)
Time /h

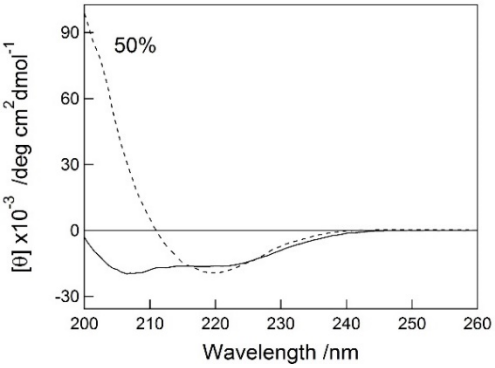
50%
[θ] x10^{-3} /deg cm^{2}dmol^{-1}
Wavelength /nm

G

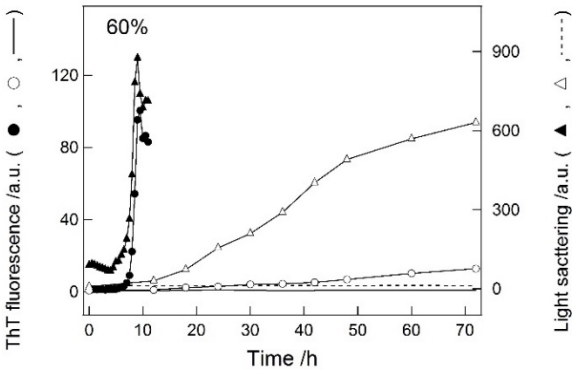
60%
ThT fluorescence /a.u. (● , ○ , ——)
Light sacttering /a.u. (▲ , △ , ------)
Time /h

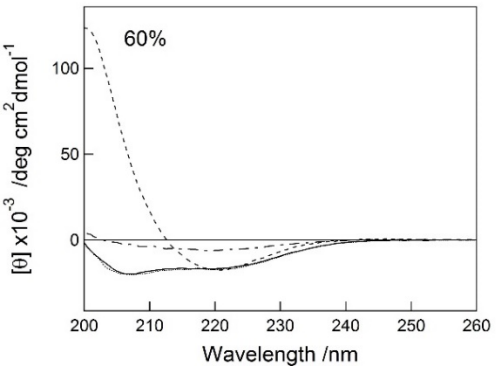
60%
[θ] x10^{-3} /deg cm^{2}dmol^{-1}
Wavelength /nm

H

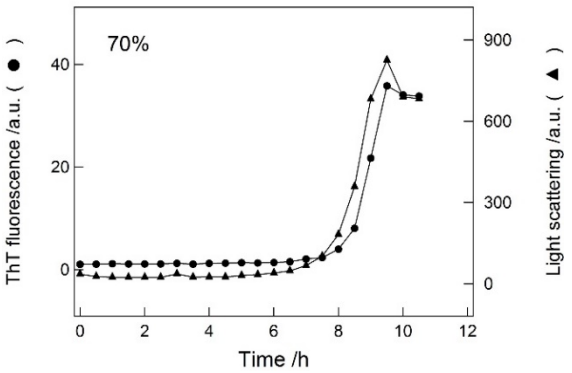
70%
ThT fluorescence /a.u. (●)
Light scattering /a.u. (▲)
Time /h

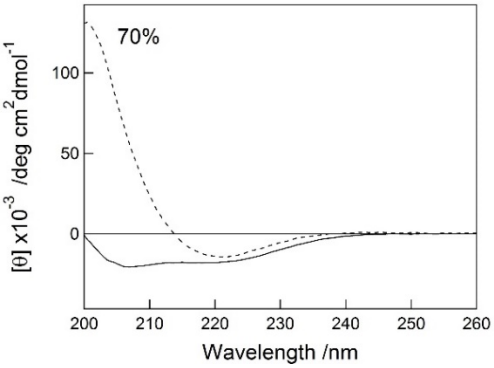
70%
[θ] x10^{-3} /deg cm^{2}dmol^{-1}
Wavelength /nm

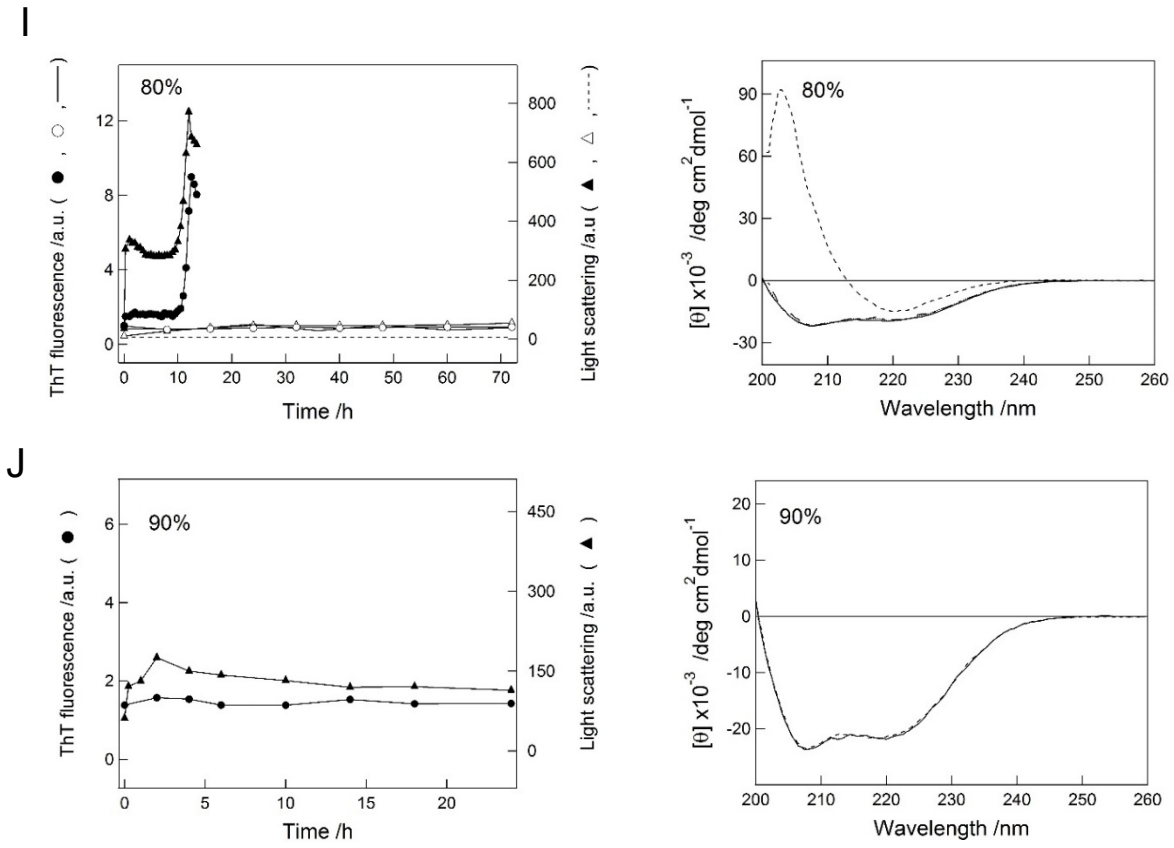

Figure 2. TFE-dependent aggregation kinetics of lysozyme with and without agitation. Aggregation at 1.5 mg mL^{-1} lysozyme was monitored by ThT fluorescence and light scattering (left) and far-UV CD (right) in 0 (A), 10 (B), 20 (C), 30 (D), 40 (E), 50 (F), 60 (G), 70 (H), and 80 (I) 90% (J)TFE. ThT (left axis) and light scattering (right axis) intensities with sonication plus stirring (●, ▲), with stirring (○, Δ), and without agitation (solid lines, broken lines) were plotted as a function of incubation time. The far-UV CD spectra with sonication plus stirring (broken lines), with stirring (broken and dotted lines), or without agitation (dotted lines) were recorded at 48 h after sample preparation. Spectra measured immediately (~5 min) after samples were dissolved are shown for comparison (solid lines).

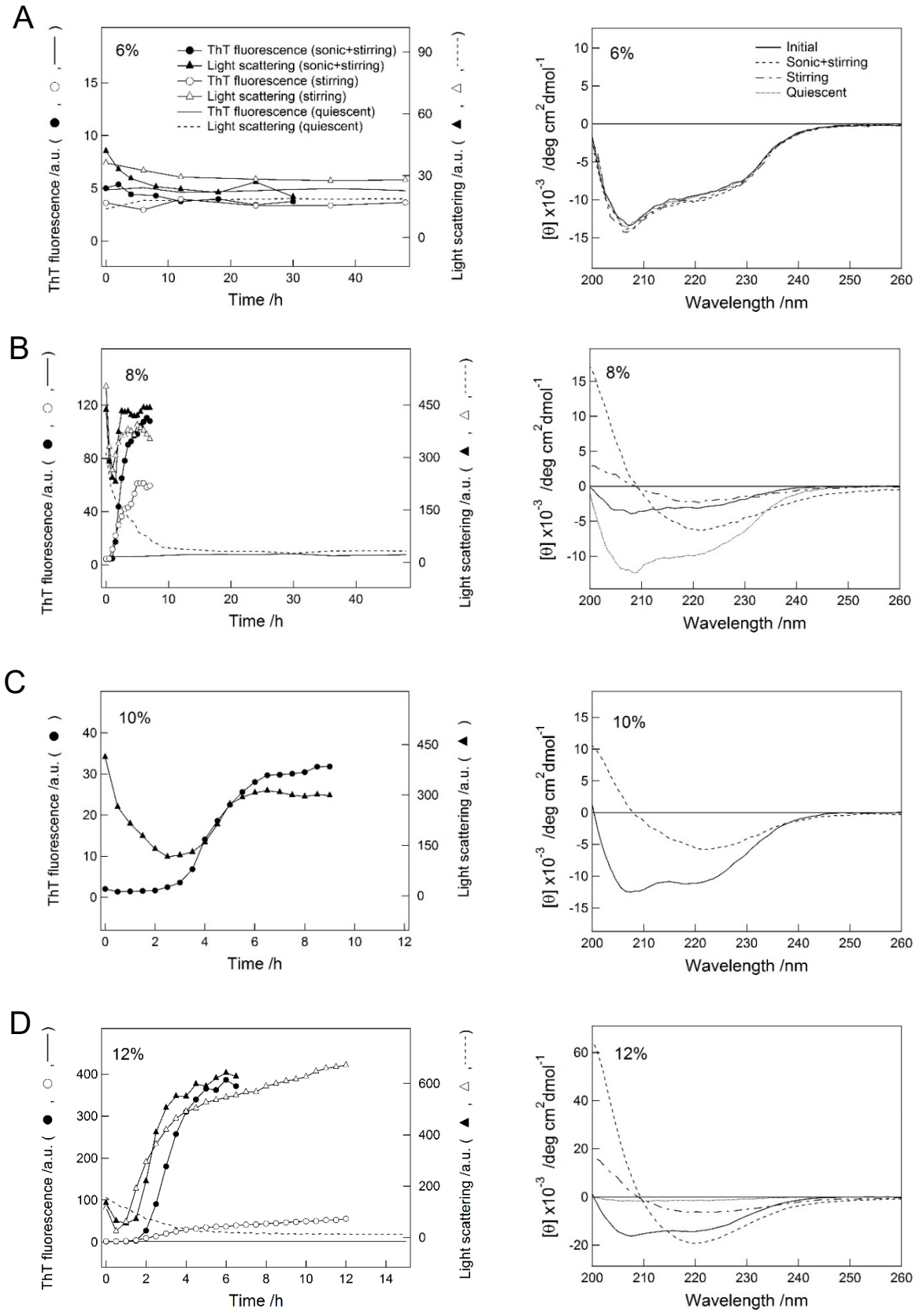
A
6%
ThT fluorescence (sonic+stirring)
Light scattering (sonic+stirring)
ThT fluorescence (stirring)
Light scattering (stirring)
ThT fluorescence (quiescent)
Light scattering (quiescent)
ThT fluorescence /a.u. (● , ○ , ——)
Light scattering /a.u. (▲ , △ , ----)
Time /h
6%
Initial
Sonic+stirring
Stirring
Quiescent
[θ] x10-3 /deg cm2dmol-1
Wavelength /nm
B
8%
8%
C
10%
10%
D
12%
12%

E

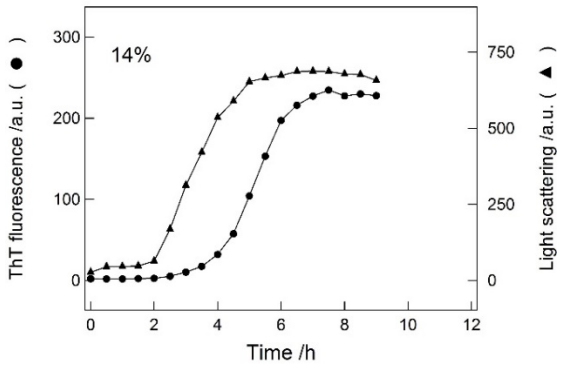
14%
ThT fluorescence /a.u. (●)
Light scattering /a.u. (▲)
Time /h

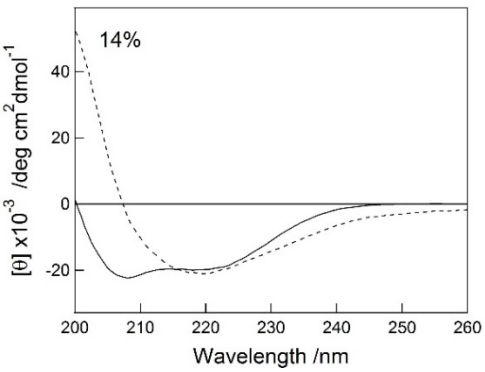
14%
[θ] x10^{-3} /deg cm^{2}dmol^{-1}
Wavelength /nm

F

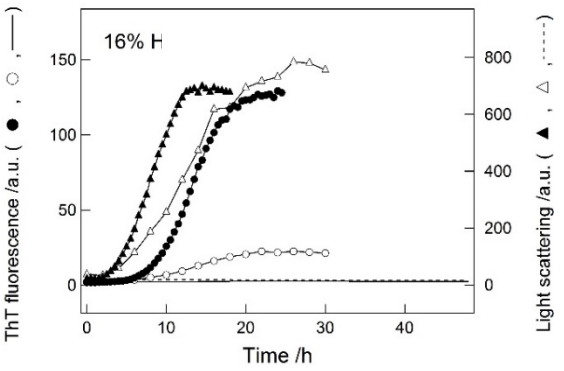
16% H
ThT fluorescence /a.u. (● , ○ , ——)
Light scattering /a.u. (▲ , △ , ------)
Time /h

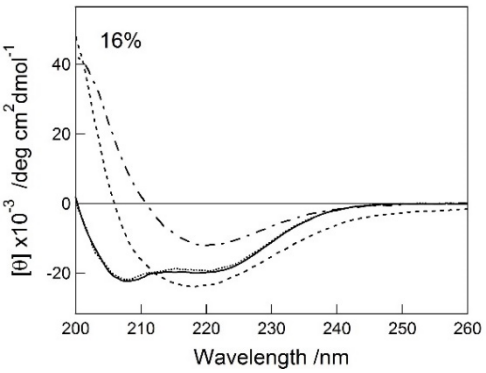
16%
[θ] x10^{-3} /deg cm^{2}dmol^{-1}
Wavelength /nm

G

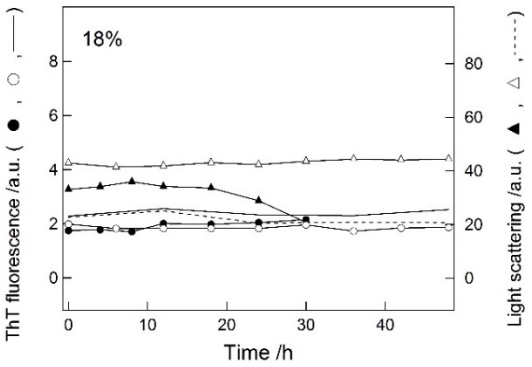
18%
ThT fluorescence /a.u. (● , ○ , ——)
Light scattering /a.u. (▲ , △ , ------)
Time /h

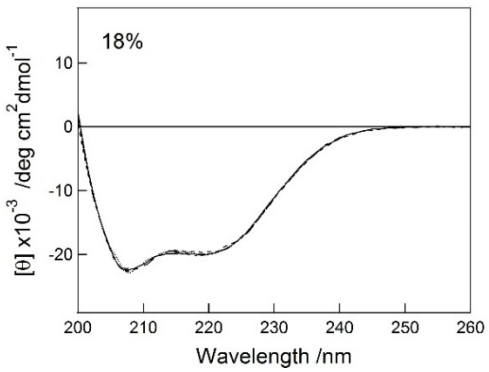
18%
[θ] x10^{-3} /deg cm^{2}dmol^{-1}
Wavelength /nm

H

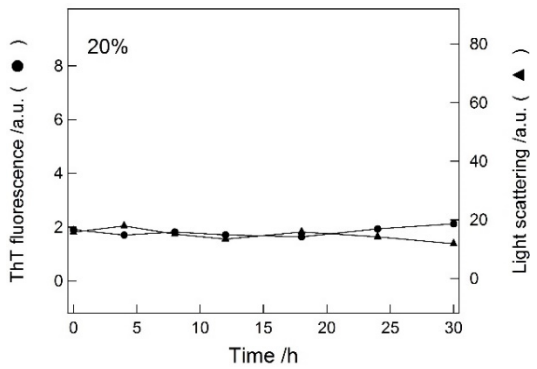
20%
ThT fluorescence /a.u. (●)
Light scattering /a.u. (▲)
Time /h

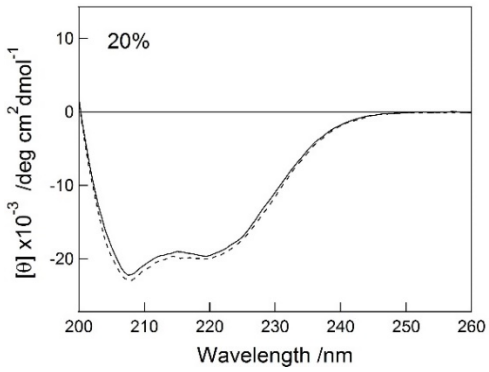
20%
[θ] x10^{-3} /deg cm^{2}dmol^{-1}
Wavelength /nm

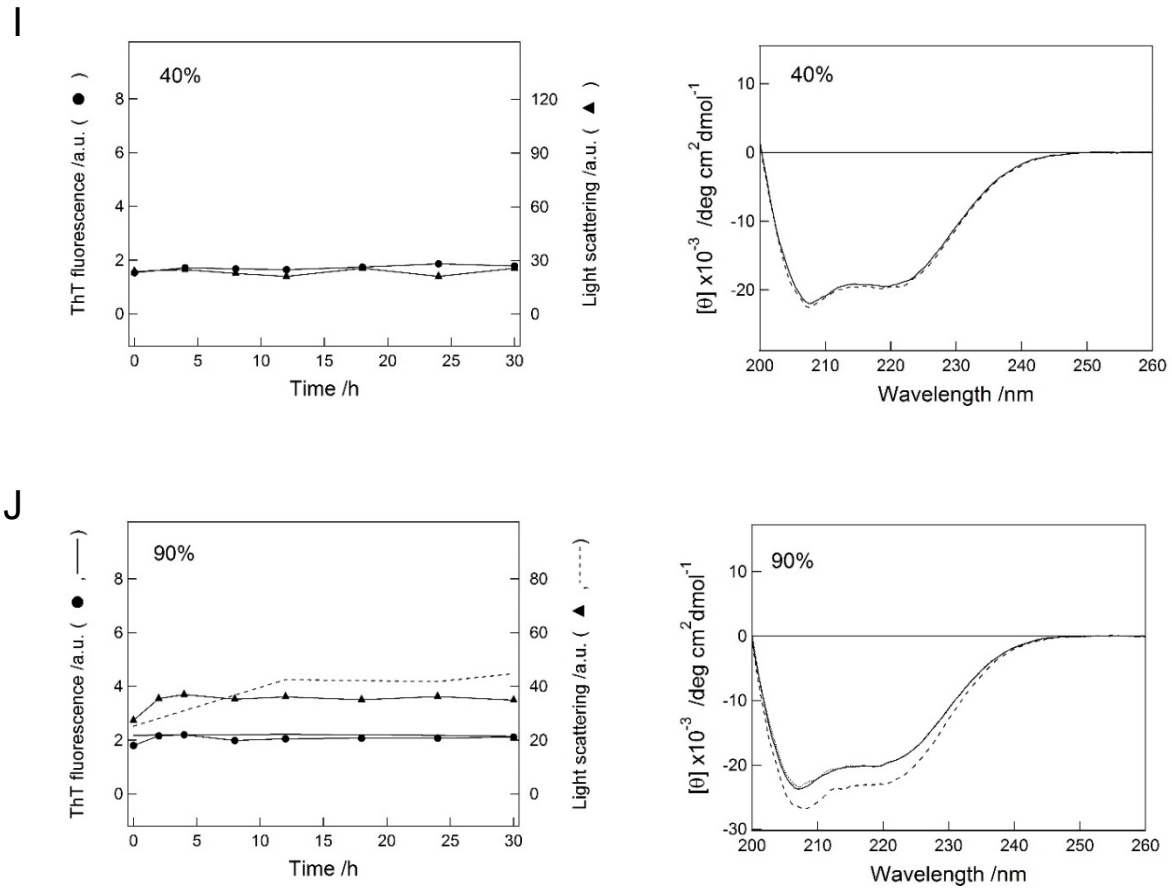

Figure 3. HFIP-dependent aggregation kinetics of lysozyme with and without agitation. Aggregation at 1.5 mg mL^{-1} lysozyme was monitored by ThT fluorescence and light scattering (left) and far-UV CD (right) in 6 (A), 8 (B), 10 (C), 12 (D), 14 (E), 16 (F), 18 (G), 20 (H), 40 (I), and 90% (J). ThT (left axis) and light scattering (right axis) intensities with sonication plus stirring (●, ▲), with stirring (○, Δ), and without agitation (solid lines, broken lines) were plotted as a function of incubation time. The far-UV CD spectra with sonication plus stirring (broken lines), with stirring (broken and dotted lines), and without agitation (dotted lines) were recorded at 48 h after sample preparation. Spectra measured immediately (~5 min) after samples had dissolved are shown for comparison (solid lines).

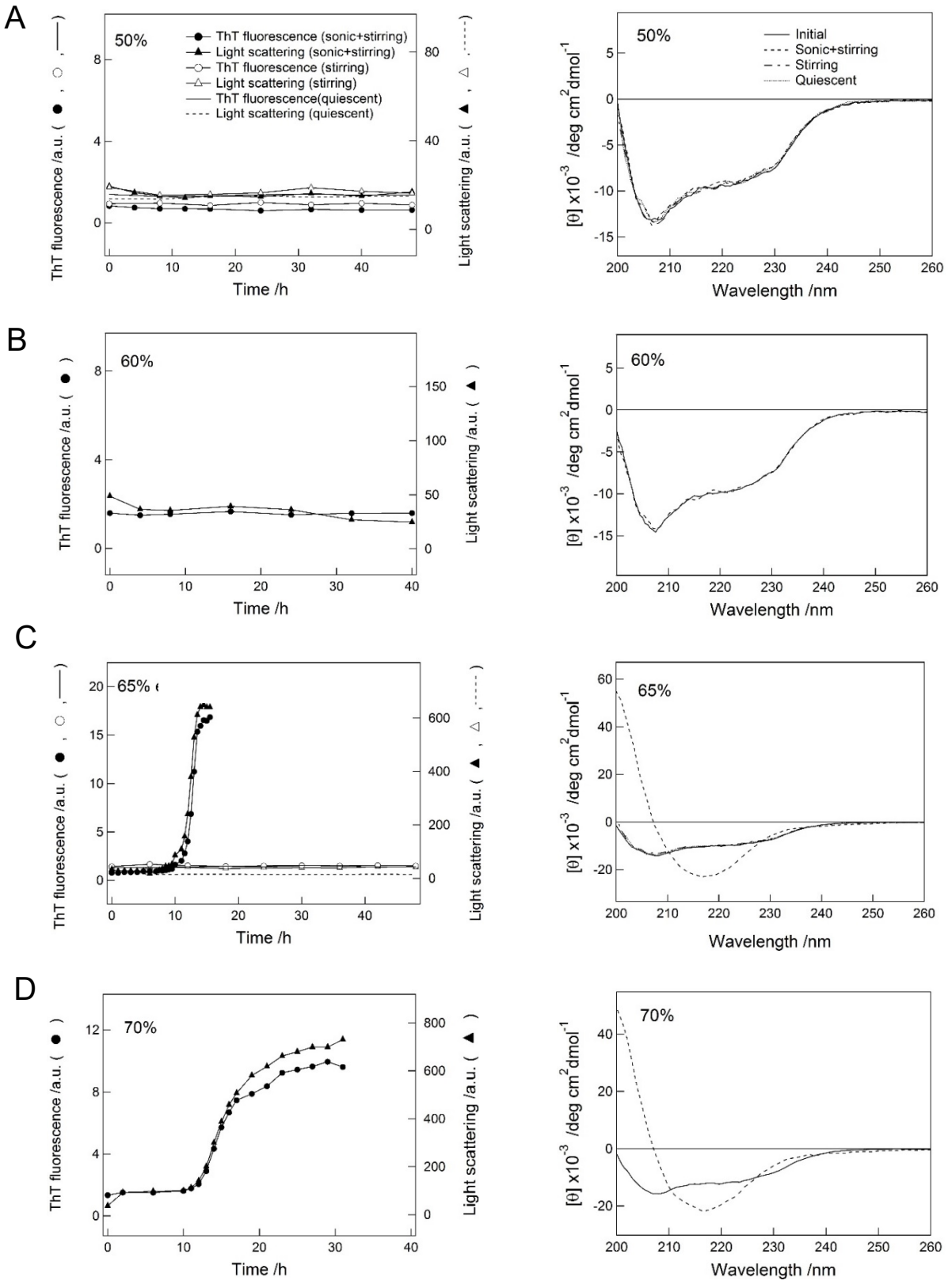
A
50%
ThT fluorescence (sonic+stirring)
Light scattering (sonic+stirring)
ThT fluorescence (stirring)
Light scattering (stirring)
ThT fluorescence(quiescent)
Light scattering (quiescent)
ThT fluorescence /a.u. (● , ○ , ——)
Light scattering /a.u. (▲ , △ , ----)
Time /h
50%
Initial
Sonic+stirring
Stirring
Quiescent
[θ] x10^{-3} /deg cm^{2}dmol^{-1}
Wavelength /nm
B
60%
60%
C
65%
65%
D
70%
70%

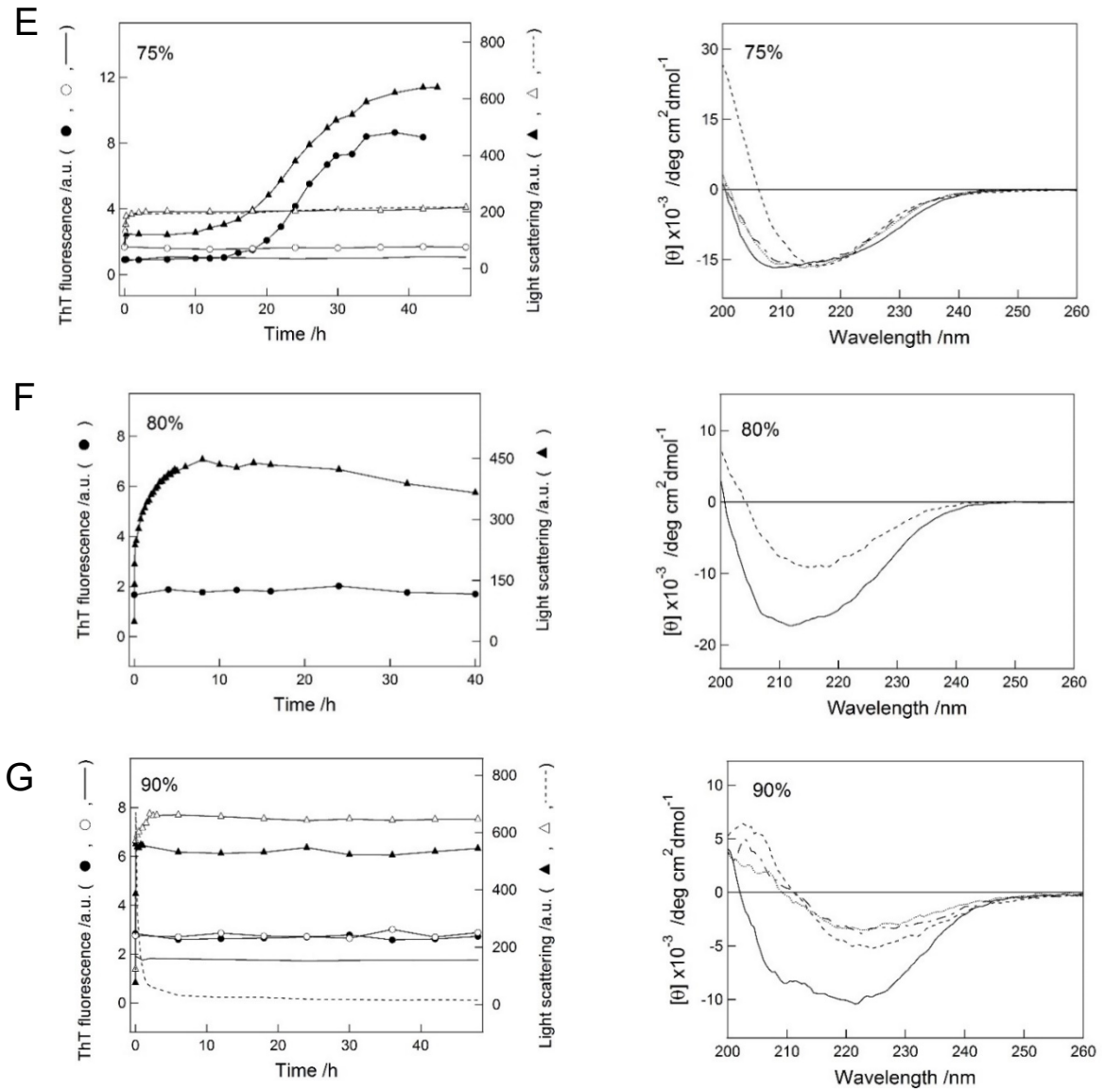

Figure 4. Ethanol-dependent aggregation kinetics of lysozyme with and without agitation. Formation of aggregates at 1.5 mg mL^{-1} lysozyme was monitored by ThT fluorescence and light scattering (left) and far-UV CD (right) in 50 (A), 60 (B), 65 (C), 70 (D), 75 (E), 80 (F) , and 90% (G). ThT (left axis) and light scattering (right axis) intensities with sonication plus stirring (●, ▲), with stirring (○, Δ), and without agitation (solid lines, broken lines) were plotted as a function of incubation time. The far-UV CD spectra with sonication plus stirring (broken lines), with stirring (broken and dotted lines), and without agitation (dotted lines) were recorded at 48 h after sample preparation. Spectra measured immediately (~5 mins) after samples had dissolved are shown for comparison (solid lines).

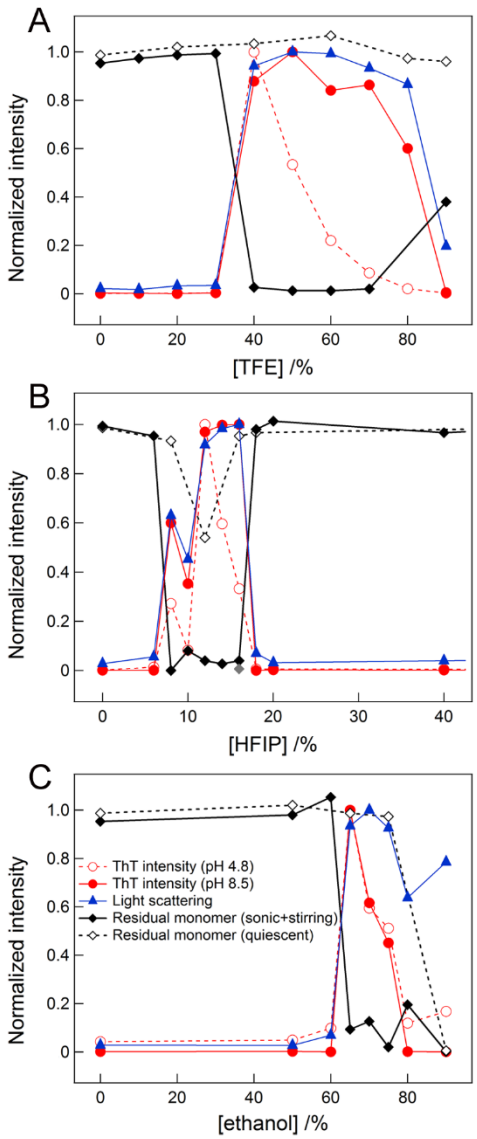

Figure 5. Solubility of lysozyme in water/alcohol mixtures. The concentrations of remaining monomers and the ThT and light scattering intensities of 1.5 mg mL^{-1} lysozyme after incubation were normalized and plotted against (A) TFE, (B) HFIP, and (C) ethanol concentrations. Residual monomers at pH 4.8 with sonication under stirring (⧫) and without agitation in the absence (◊) and presence (filled gray diamond) of seeds were quantified and plotted. ThT (red ○) and light-scattering (blue ▲) intensities at pH 4.8 obtained by real-time observations and the ThT intensity (red ●) at pH 8.5 were plotted against alcohol concentration.

Alcohol-Induced Transitions under Ultrasonication

The effects of agitation on the lysozyme solution at various concentrations of alcohol−water mixtures were examined (Figure 2−4). I used an attachment by which the ultrasonic pulses can be applied directly to the cuvette of the fluorescence spectrophotometer.[30] This attachment enabled the real-time monitoring of the effects of ultrasonication. I compared the effects of stirring the solution with the effects of ultrasonication plus stirring. The reaction kinetics were monitored by measuring ThT fluorescence at 480 nm and light scattering at 350 nm.

Upon stirring in the presence of 40% TFE, light scattering increased after a lag time of 10 h, followed by a moderate increase in ThT fluorescence with a lag time of around 20 h (Figure 2E). Ultrasonic pulses accelerated these changes: the increase in ThT fluorescence and light scattering occurred concomitantly at 8 h (Figure 2E). The final fluorescence intensity was much greater than that with stirring. Although no change was observed at 80% TFE under stirring even after 70 h, ultrasonication plus stirring caused an increase in ThT fluorescence and light scattering at 10 h (Figure 2I). The concomitant increase in ThT fluorescence and light scattering indicated a highly cooperative effect. Below 30% TFE, there was no change in light scattering after 48 h even with ultrasonication plus stirring (Figure 2A−D).

The products formed by applying ultrasonic pulses were examined by CD and AFM (Figure 2, Figure 6). The CD spectra in 40−80% TFE showed the formation of β-sheet dominated structures, and the AFM images showed that the major products had a fibrillar morphology, confirming that the ultrasonic pulses produced amyloid fibrils.

Fibrillation as described above is coupled with alcohol denaturation of the native state. To determine the role of denaturation, I conducted the same measurements except starting with lysozyme directly dissolved in 90% TFE at pH 4.8 and then diluted at respective TFE concentrations (Figure 7). The reactions monitored by light scattering and ThT fluorescence were similar over a wide range of

TFE concentrations although the lag time was shortened by 3 to 4 h. This indicated that even if the denaturation of the native state affects the lag time, the equilibrium between the soluble and fibrillar forms is independent of the method of sample preparation. The shorter lag time implies that additional conformational states exist before complete denaturation to the amyloid-competent TFE denatured state.

HFIP is an alcohol that is more effective than TFE in generating amyloid fibrils.6,10 At 16% HFIP, stirring produced amyloid fibrils with a lag time of 8 h has monitored with ThT fluorescence, which was preceded by an increase in light scattering (Figure 3F). It is noted that this lag time (~8 h) is similar to that in the presence of 40% TFE (Figure 2E), indicating that the apparent lag time is determined by the combined effect of the alcohol species and its concentration. Ultrasonication slightly shortened the lag time by ~1 h. Light scattering and ThT fluorescence increased steeply in comparison to stirring alone, indicating increased cooperativity. The formation of fibrils was confirmed from CD spectra and AFM images (Figure 3F, Figure 5G).

In 8−12% HFIP, the mixing of lysozyme with HFIP caused transient aggregation, which disappeared within 10 h (Figure 3B−D). Agitation of the solution by either stirring or ultrasonication plus stirring resulted in the formation of amyloid fibrils before the complete dissolution of aggregates. Because of the competition between the dissolution of aggregates and the formation of fibrils, light scattering showed a minimum at 2 h for 8% HFIP and at 1 h for 12% HFIP, the same time when the ThT fluorescence started to increase. It was noted that the far-UV CD spectrum at 8% HFIP showed a sudden decrease in the CD signal because of the formation of large aggregates (Figure 1B), leading to the low reproducibility of the CD signal. This was also true for the light-scattering intensity at 8% HFIP (Figure 3B). At other HFIP concentrations, the reproducibility was high for both CD and light-scattering signals.

The effects of ultrasonication on the lag time were weaker in the HFIP solutions than in the

TFE and ethanol solutions (see below). The absence of accelerating effects on fibrillation suggested that the transient aggregates, possibly present even in the 16% HFIP solution, include nucleus-competent oligomers.

I also examined the effects of agitation on lysozyme solution at various concentrations of ethanol (Figure 4). At 65% ethanol (Figure 4C), although stirring did not bring about apparent effects, ultrasonication plus stirring induced amyloid fibrillation at 10 h. At higher ethanol concentrations (above 80%), aggregation of the solution occurred quickly after preparation of the solution, and no clear effect of agitation was observed (Figure 4F,G). The products at 70−75% ethanol were a mixture of mature and protofibrils judging from the CD spectra and AFM images (Figure 4D,E, Figure 5K). At 80 and 90% ethanol, although the CD spectrum indicated the β-sheet-dominant structure, the AFM images revealed largely amorphous aggregates (Figure 4F,G, Figure 5L).

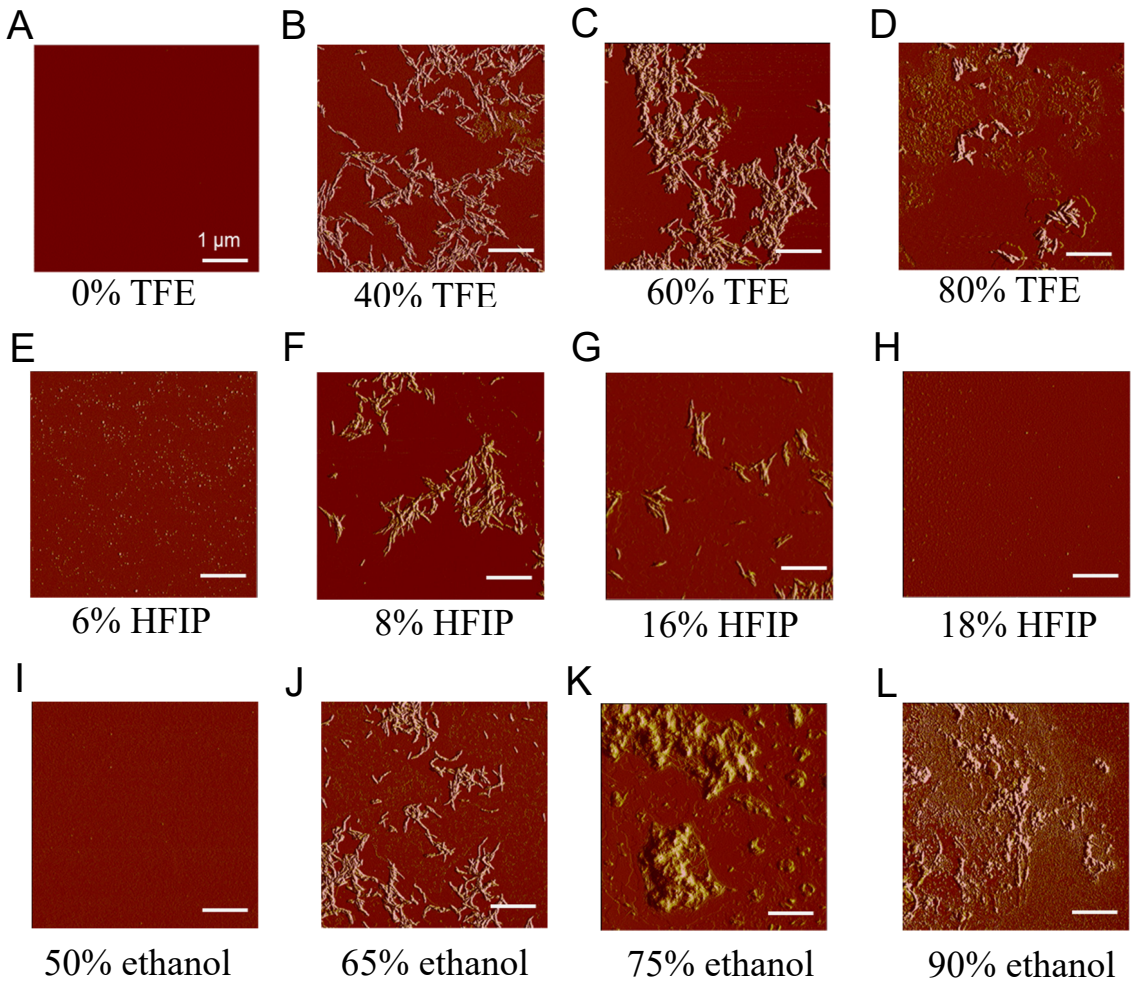

Figure 6. Aggregates of lysozyme formed under distinct alcohol conditions with sonication plus stirring examined by AFM. AFM images of 1.5 mg mL^{-1} lysozyme after treatment with sonication and stirring in 0 (A), 40 (B), 60 (C) and 80% (D) TFE; in 6 (E), 8 (F), 16 (G) and 18% (H) HFIP; in 50 (I), 65 (J), 75 (K), and 90% (L). The scale bars represent 1 μm. It should be noted that the molecular species of lysozyme at 8% HFIP are a coexistence of mature fibrils, protofibrils, and amorphous aggregates as shown in the phase diagram (Figure 13). Although mature amyloid fibrils are shown in the AFM images (F), the low CD signal intensity which is around 25% of the mature fibrils (Figure 3B) and the low ThT fluorescence which is around 60% of the mature fibrils (Figure 4B) suggest a mixture of protofibrils and amorphous aggregates.

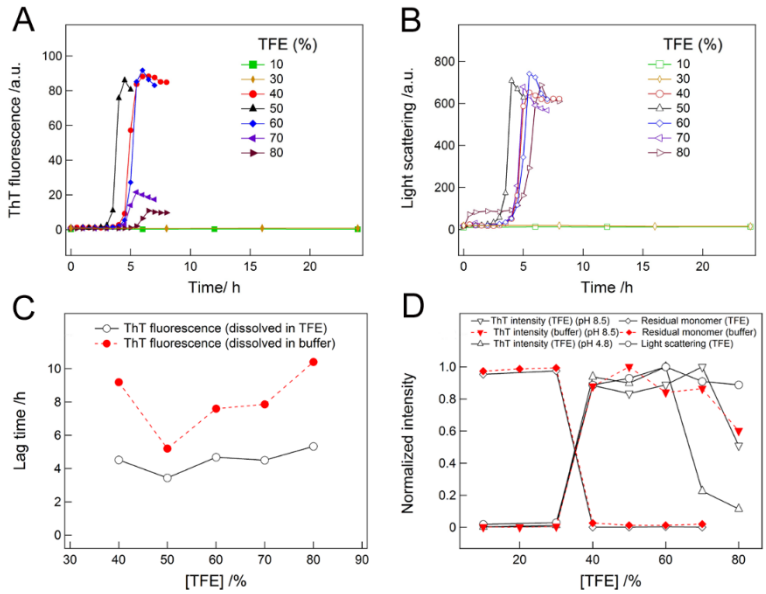

Figure 7. Effects of the method of sample preparation on aggregation kinetics and solubility of lysozyme in water/TFE mixtures. In these experiments, lysozyme was first dissolved with 90% TFE then diluted using 25 mM sodium acetate buffer (pH 4.8). (A,B) The aggregation kinetics of 1.5 mg mL^{-1} lysozyme during the 0-24 h incubation period was monitored by using the ThT assay (A) and light scattering (B) under sonication treatment with continuous stirring in real time. (C) The lag times of aggregation of lysozyme dissolved in TFE and then diluted with buffer (black) were compared with those of lysozyme dissolved in buffer to which TFE was then added (red). The lag times based on ThT intensity were plotted against TFE concentrations. (D) The concentrations of remaining monomers (diamonds) and the ThT (triangles) and light scattering (circles) intensities of 1.5 mg mL^{-1} lysozyme after 24 h-incubation were normalized and plotted against TFE concentrations. The results of standard experiments in which lysozyme was first dissolved in sodium acetate buffer and then TFE was added are shown by red symbols. The results of reverse experiments in which lysozyme was first dissolved in TFE and then diluted with buffer are shown by black symbols. The maximum ThT intensities in A were used for D.

Remaining Soluble Proteins

For the three types of alcohols, I examined the soluble protein concentration after incubation with or without agitation (Figure 5). When the ultrasonication-dependent bursts of signals ended, I stopped the ultrasonic irradiation and estimated the soluble protein concentration after centrifugation. When the ultrasonication-dependent burst reaction did not occur within 48 h, the soluble protein concentration was determined after the incubation periods as indicated in Figure 5.

For TFE and HFIP, after incubation for 48 h under quiescent conditions, the concentration was the same as the initial lysozyme concentration except for 12% HFIP, where some turbidity remained. As for ethanol above 80%, residual soluble lysozyme decreased, where amorphous aggregation continued.

For all three types of alcohols, after fibrillation induced by ultrasonication, the remaining soluble lysozyme was close to zero (Figure 5). The dependence of residual soluble proteins on the alcohol concentration exhibited an opposite profile to those of ThT fluorescence and light scattering, indicating that the formation of fibrils is linked to the decrease in soluble protein concentration. The same relationship between an increase in fibrillilation and a decrease in solubility was also observed at high concentrations of lysozyme: 5 and 10 mg mL^{-1} (Figures 8 and 9). Moreover, the dependence of residual soluble proteins on the TFE concentration was independent of the order of sample preparation (Figure 7D): the concentrations of residual soluble proteins were almost identical.

To address the oligomeric state of soluble proteins under supersaturation, I performed dynamic light scattering measurements at 1.5 mg mL^{-1} lysozyme (Figure 10). The distribution profile of species exhibited a single dominant peak with hydrodynamic radii of 1.5−1.9 nm in both the absence and presence of alcohol, indicating that the soluble lysozymes exist as monomers. The results are consistent with the report by Harper and Lansbury,[71] suggesting that dominant species in soluble fractions under supersaturation are monomers.

Chemical degradation of lysozyme after ultrasonication treatment was investigated by high-performance liquid chromatography (HPLC) and SDS−polyacrylamide gel electrophoresis (Figure 11). For both analyses, ultrasonic agitation was combined with continuous stirring using a stirring magnet at 600 rpm and subjected to cycles of ultrasonication for 1 min at 2 min intervals. The results of HPLC showed that at least 80% of the lysozyme remains intact after 24 h. SDS−polyacrylamide gel electrophoresis detected no degradation after 24 h. Taken together, the chemical degradation of lysozyme induced by ultrasonication is minimal and does not affect our interpretation.

At 16% HFIP, I performed the seeding experiments with 5% (w/w) fibril seeds added to the monomers (Figure 12). Light scattering and ThT fluorescence increased without a lag time. No residual monomer was detected after the ending fibril extension. These confirmed that the decrease in the quantity of monomers is not caused by the specific effects of ultrasonication but is a general consequence of amyloid fibrillation (Figure 5B and 12).

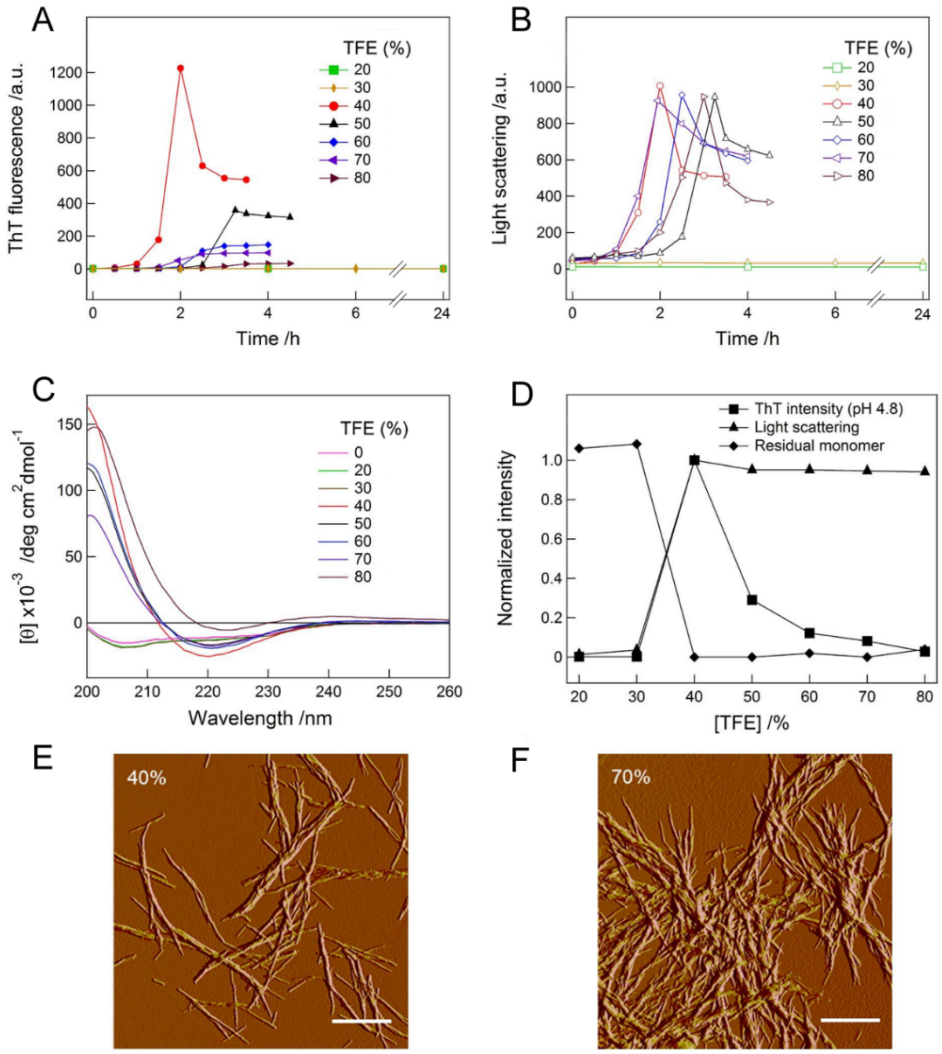

Figure 8. Aggregation kinetics and solubility of lysozyme at 5 mg mL^{-1} in water/TFE mixtures. (A,B) Amyloid fibrillation of lysozyme at 5 mg mL^{-1} monitored by ThT assay (A) and light scattering (B) in real time in 25 mM sodium acetate buffer (pH 4.8) under sonication treatment with continuous stirring. (C) The far-UV CD spectra of lysozyme solutions after incubation as shown in A. (D) Concentrations of remaining monomers (♦) and ThT (■) and light scattering (▲) intensities after incubation as shown in a Normalized values were plotted against TFE concentration. (E,F) AFM images of fibrils formed in 40 and 70% TFE. The scale bars indicate 1 μm.

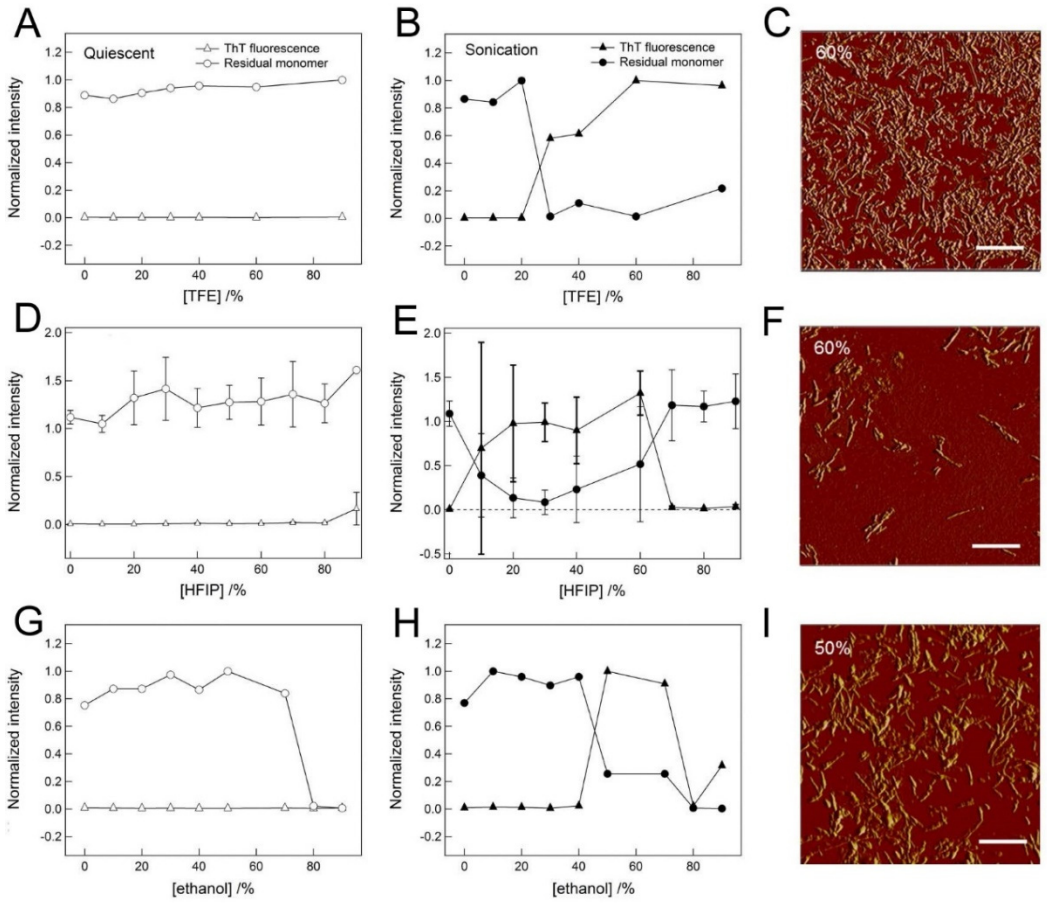

Figure 9. Alcohol concentration dependence of the amyloid fibrillation and solubility of lysozyme at 10 mg mL^{-1} in 25 mM sodium acetate buffer (pH 4.8). Aggregation was performed with microplates with a water bath-type ultrasonic transmitter (ELESTEIN SP070-PG-M; Elekon, Tokyo, Japan). The microplate was subjected to cycles of ultrasonication for 1 min at 9-min intervals, and maintained at 25 °C. Normalized values of ThT intensities (triangles) and residual monomers (circles) after incubation for 48 h in alcohol in the absence (A, D, G) and presence (B, C, E, F, H, I) of sonication treatment are shown. Error bars for the three independent sets of measurements are shown. AFM images of amyloid fibrils formed in 60% TFE (C) and HFIP (F) and in 50% ethanol (I). The scale bars indicate 1 μm.

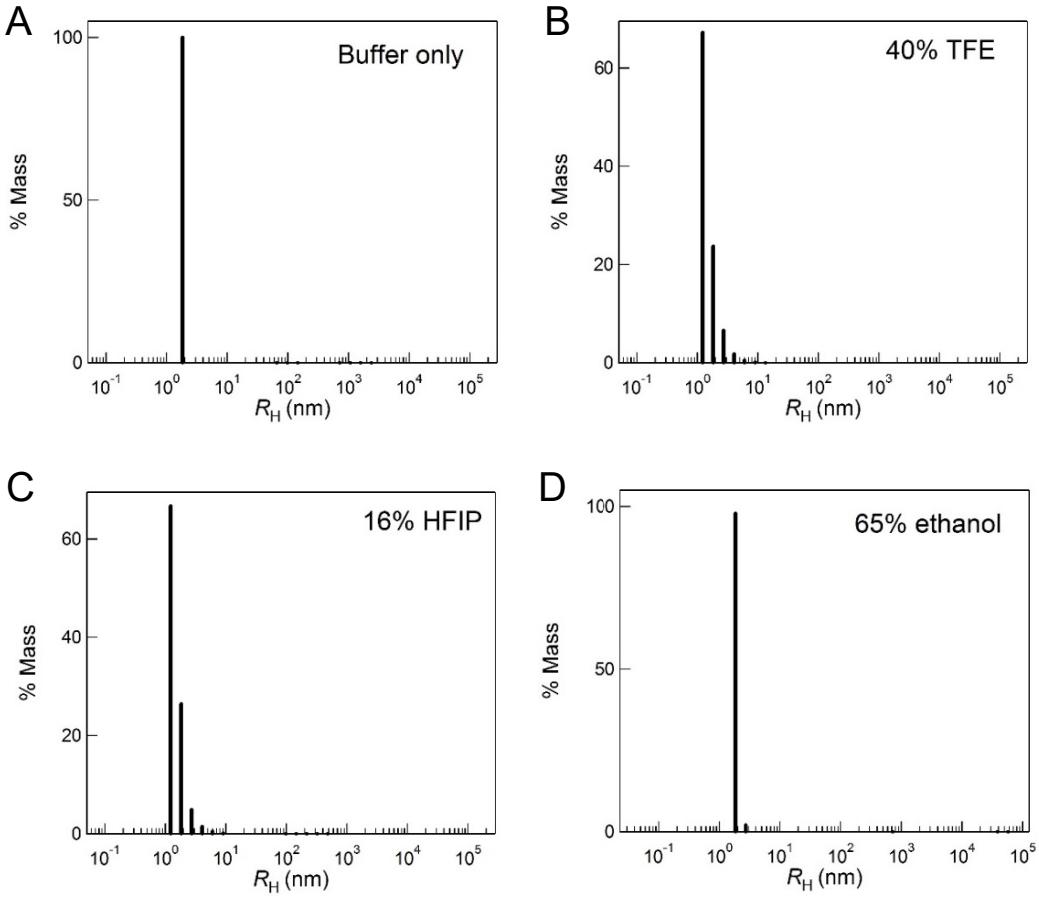

Figure 10. Dynamic light scattering measurements of lysozyme in alcohol/water mixtures. The hydrodynamic radius (R_H) of 1.5 mg mL^{-1} lysozyme in 25 mM sodium acetate buffer (pH 4.8) containing no alcohol (A), 40% TFE (B), 16% HFIP (C), and 65% ethanol (D) was 1.8, 1.5, 1.7, and 1.9 nm, respectively. Estimated relative amount of mass for each peak is represented by %Mass. The R_H values were obtained from averaging 20 individual measurements. Solvent parameters of water were used in all measurements. The R_H values in ethanol were corrected using viscosity of 65% ethanol. The results indicate that soluble lysozymes under supersaturation are monomers for the three types of alcohols. This is probably true even for the remaining soluble lysozymes after fibrillation.

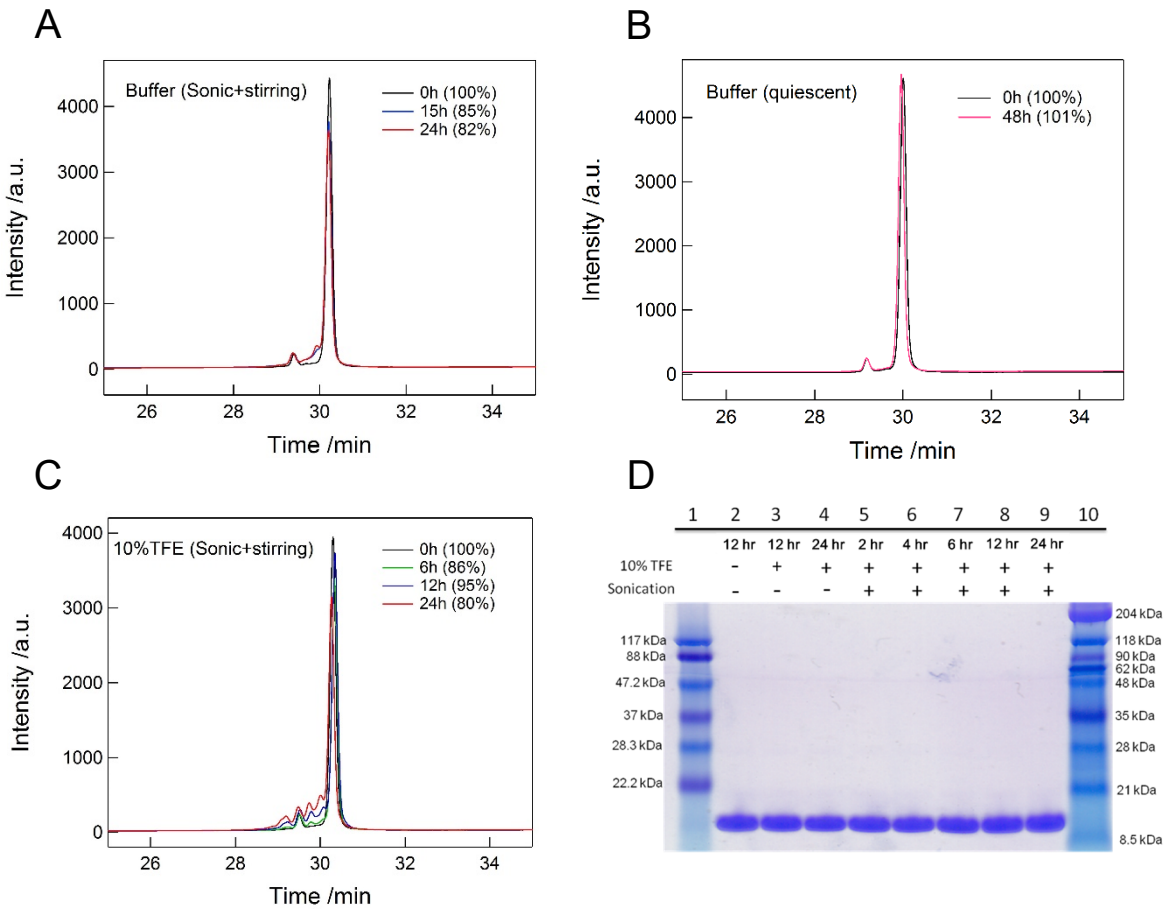

Figure 11. Effects of ultrasonication on the chemical structure of lysozyme monitored by HPLC (A-C) and SDS-PAGE (D). Chemical modification was monitored by elution profiles of analytical reverse-phase HPLC at 220 nm after incubation of lysozyme at 1.5 mg mL^{-1} in 25 mM sodium acetate buffer (pH 4.8) under no agitation (A), incubation under sonication plus stirring in 25 mM sodium acetate buffer (pH 4.8) (B) or incubation under sonication plus stirring in 25 mM sodium acetate buffer (pH 4.8) with 10% TFE (C). Incubation periods were 0 (black), 6 (green), 12 and 15 (blue), 24 (red), and 48 h (magenta). Relative peak heights compared with the peak height at 0 h are shown in percentage. (D) SDS-PAGE analyses of lysozyme at 1.5 mg mL^{-1} in 25 mM sodium acetate buffer (pH 4.8) with 10%TFE. The lysozyme solutions were incubated with and without treatment of sonication plus stirring for 2, 4, 6, 12, and 24 h. The first (1) and final lanes (10) indicate marker proteins for molecular weight.

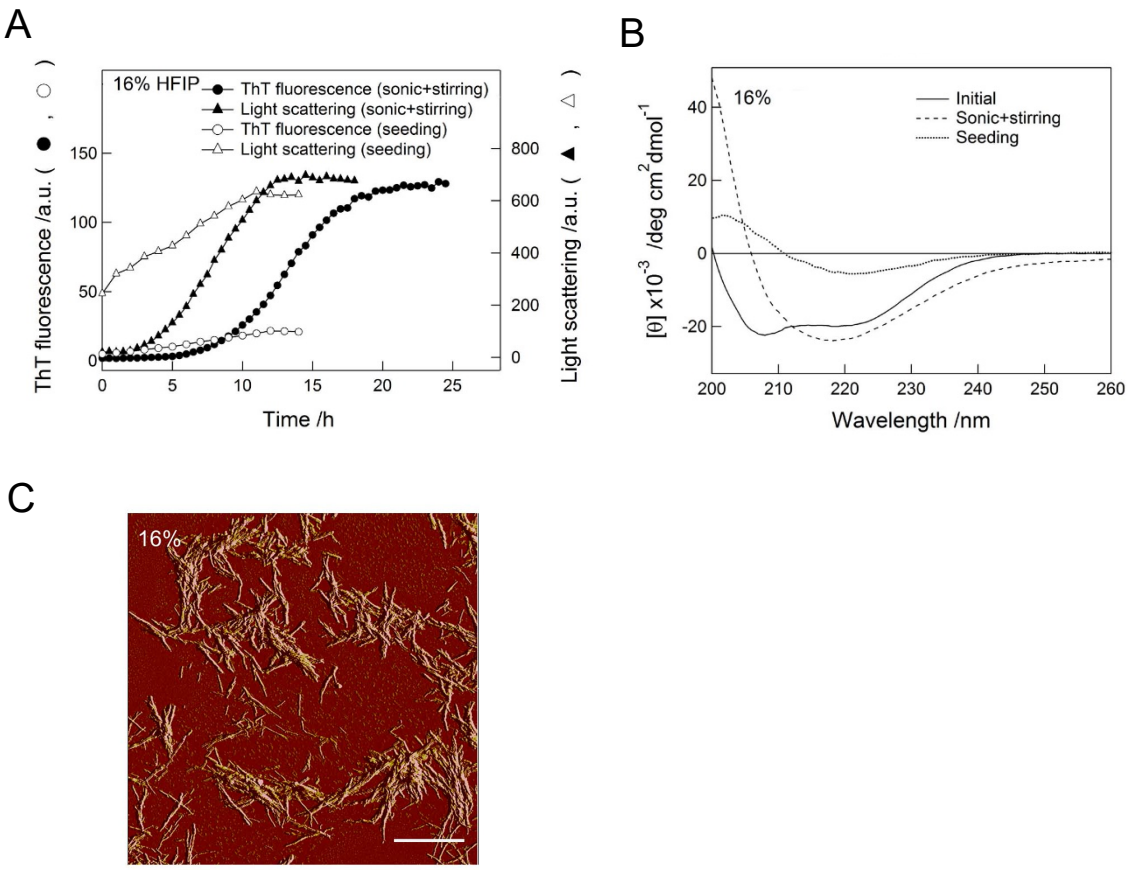

Figure 12. Seed-dependent fibril elongation. (A) Fibril elongation of 1.5 mg mL^{-1} lysozyme in the presence of 5% (w/w) fibril seeds with stirring in 16% HFIP and 25 mM sodium acetate buffer (pH 4.8) was monitored by the ThT (○) and light scattering (Δ) intensity. The results of ThT (●) and light scattering intensities (▲) with sonication plus stirring are shown for comparison. (B) Far-UV CD spectra of lysozyme solutions subjected to sonication plus stirring (broken line) and incubated in the presence of 5% fibril seeds (solid line) were recorded. Spectra (solid line) measured soon (~5 mins) after samples had dissolved are shown for comparison. The same data in Figure 2B were used for A and B. (C) The AFM images of amyloid fibrils of lysozyme formed in the presence of 5% fibril seeds in 16% HFIP. The scale bars indicate 1 μm.

Phase Diagram Dependent on Protein and Alcohol Concentrations

Because formations of amyloid fibrils or amorphous aggregates are intermolecular reactions, the alcohol-induced solidification over soluble states will depend on the protein concentration. I examined ultrasonication-dependent fibrillation at 5 mg mL^{-1} for the three alcohols and at 10 mg mL^{-1} for TFE (Figures 8 and 9) using a microplate and a bath-type ultrasonicator. As expected, the higher the protein concentration, the larger the range of alcohol concentration inducing the ultrasonication-dependent transitions. At higher lysozyme concentrations, the formation of gels (i.e., viscous aggregates with light transparency) sometimes occurred. Various types of conformational states including amorphous aggregates, amyloid fibrils, and native structure may participate in the formation of gels, although the exact mechanism of gelation is unclear.

On the basis of the alcohol-dependent transitions of lysozyme at different protein concentrations, I constructed phase diagrams of conformational states (Figure 13). For the three alcohols, an increase in protein concentration enlarged the region of amyloid fibrils. As for TFE, amorphous and gel regions existed at higher TFE concentrations. As for ethanol, a mixture of protofibrils and amorphous aggregates prevailed above 80%. The phase diagram shows that the equilibrium conformation of lysozyme is determined by combined effects of protein concentration and solubility at various water/alcohol mixtures. This leads to a V-shaped region of amyloid fibrillation, the bottom concentration of which depends on the hydrophobicity of alcohols (i.e., HFIP < TFE < ethanol). Importantly, these phase diagrams were disclosed only after overcoming the metastability by ultrasonication and enable us easily to predict the phase behavior of lysozyme with respect to the changes in environmental conditions.

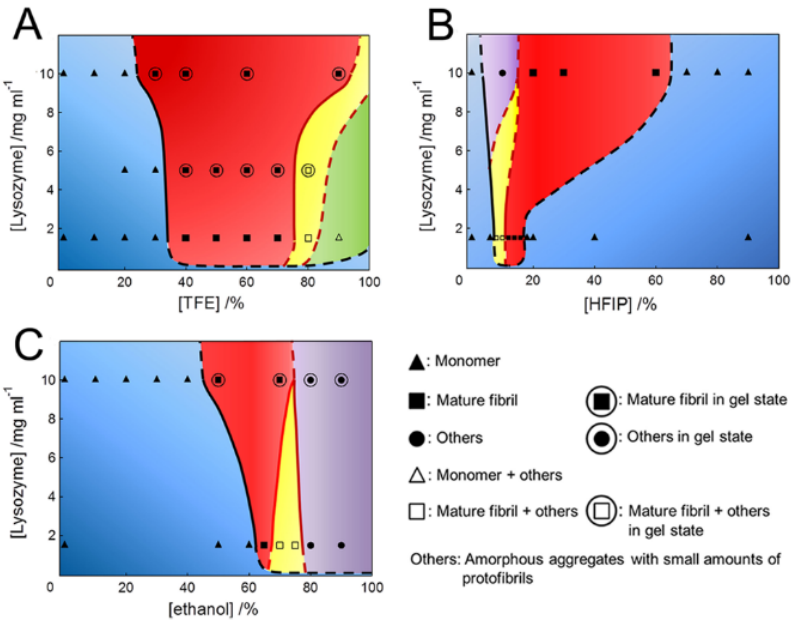

Figure 13. Phase diagrams of lysozyme in water/alcohol mixtures of (A) TFE, (B) HFIP, and (C) ethanol. Blue, monomers; red, amyloid fibrils; yellow, dominantly mature fibrils with a small quantity of amorphous aggregates and protofibrils; magenta, amorphous aggregates with a small quantity of protofibrils; and green, monomers with a small quantity of protofibrils. Dominant species detected at 1.5, 5, and 10 mg mL^{-1} and various alcohol concentrations are indicated by symbols. Molecular species in gel states are highlighted by open circles on the symbols.

2-4. Discussion

Decreased Solubility of Proteins in Alcohol/Water Mixtures

Alcohols are hydrophobic solvent dissolving protein hydrophobic groups. Because peptide bonds are polar, they tend to be excluded from hydrophobic alcohols. Consequently, alcohols denature the proteins by destabilizing hydrophobic interactions and stabilize the "open helical conformations" by strengthening the hydrogen bonds.[31, 35] However, water is a polar solvent forming hydrogen bonds with peptide groups and tends to exclude hydrophobic groups of proteins. When the intramolecular hydrophobic interactions of proteins are stronger than the solvation effects, proteins fold, forming native structures with increased solubility. Thus, both water and alcohols are good solvents for polypeptides although the conformation of polypeptides changes so as to decrease the overall free energy. Then what is the solubility of polypeptides in water/alcohol mixtures?

There is evidence that the solubility of polypeptides decreases in water/alcohol mixtures where the concentration range depends on the alcohol species. Ethanol-dependent precipitation is a routine method for fractioning serum proteins.[78] Relatively high concentrations of ethanol are known to induce fibrillar aggregates.[79-81] For TFE and HFIP, only moderate concentrations are effective for inducing fibrillar aggregates (Figures 5 and 13). 2-Methyl-2,4-pentanediol has been used to induce protein crystals.[82] In this article, I showed that the concentration of monomers decreases significantly under the conditions where fibrils form (Figure 5). Thus, I can conclude that fibrillation is coupled with the decreased solubility of proteins at certain concentrations of alcohol/water mixtures.

Mechanism of the Decreased Solubility

Why does the solubility decrease in alcohol/water mixtures, in particular, with TFE and HFIP? These highly fluorinated alcohols are known to form dynamic clusters over a certain range of

concentration.[34] These hydrophobic clusters probably interact with hydrophobic regions of proteins, inducing extensive hydrophobic interactions among solvents and solutes, resulting in a decrease in the equilibrium solubility. Further increases in the TFE or HFIP concentration increase the hydrophobicity enough to accommodate the hydrophobic polypeptides, causing redissolution at high concentrations. Whereas HFIP showed a clear minimum in solubility at 8−16%, the minimum for TFE shifted to the higher concentration range of 40−70% (Figures 5 and 13). In the case of ethanol with moderate alcohol effects, only the decrease in solubility is evident.

A similar mechanism will apply for the effects of SDS. SDS around the CMC has been known to induce protein aggregation and amyloid fibrillation.[41, 66, 73, 83-88] Because SDS has a hydrophobic tail, it tends to interact with other SDS molecules. Slightly below the CMC, the interactions are dynamic and unstable. In the presence of hydrophobic solutes such as denatured proteins, marginal and dynamic clusters of SDS also interact with denatured proteins, producing larger aggregates. As for some proteins and peptides, amyloid fibrils are more stable than amorphous aggregates, eventually leading to the formation of fibrils. Above the CMC, SDS can form stable micelles so that peptides or proteins become fully accommodated on or in SDS micelles, forming open helical structures[31, 35] similar to those formed in the presence of high concentrations of TFE or HFIP.

Impact of Supersaturation

Although the equilibrium solubility shows a minimum at moderate concentrations of alcohol/water mixtures, supersaturation prevents the smooth conversion of soluble lysozyme to aggregated forms (Figure 5). For both TFE and HFIP, agitation of the solution is essential to provoke aggregation. Under certain conditions, stirring of the solution is not enough and an intensive agitation by ultrasonication is required to surmount the metastability of supersaturation. Seeding with preformed fibrils was also effective at overcoming the metastability (Figure 5B, Figure 12). Because the chemical

decomposition of lysozyme was minimal (Figure 11), agitation by ultrasonication works effectively to minimize the effect of supersaturation as confirmed in previous studies.[59, 76]

I previously showed that whereas supersaturation is essential for the formation of crystal-like amyloid fibrils, the formation of glassy amorphous aggregation occurs without supersaturation and thus without a high free energy barrier.[30, 76] Indeed, ethanol above 80% induced amorphous aggregation rapidly even under quiescent conditions, consistent with the above view of crystalline amyloid fibrils versus glassy amorphous aggregates.

Although various kinds of agitation can overcome the metastability of supersaturation, additive effects of ultrasonication on stirring indicate that ultrasonication is particularly effective at subduing supersaturation. Ultrasonication produces cavitation bubbles. It is likely that both stirring and ultrasonication produce a water/air interface on which nucleus-competent aggregates form. In addition, ultrasonication produces shearing forces that are due to the rigorous local flow of solvent accompanied by the formation and disappearance of cavitation bubbles. Although ultrasonication produces OH radicals potentially causing various chemical reactions, the chemical damage to lysozyme under our experimental conditions was minimal. In addition, ultrasonication-induced heating is not a dominant factor because the temperature increase was kept to a minimum by using a temperature-controlled water bath and a long quiescent period (2 and 9 min) between 1 min periods of ultrasonic radiation.[30, 59]

Although the solubility of proteins decreases at moderate concentrations of TFE or HFIP, metastability prevents the conversion of monomers to crystal-like amyloid fibrils. The persistence of supersaturation can be disclosed by observing the effects of ultrasonication. Combining the results of this study, I propose a protein misfolding funnel (Figure 14) contrasting with a classical protein folding funnel in which the combined effects of entropy and energy terms without kinetic trapping establish a funnel-like energy landscape with mimimal frustration.[89, 90] The funnel shape defined by equilibrium

solubility depends on the type of alcohols. When the precipitates are glassy amorphous aggregates, they appear spontaneously with a decrease in solubility. When the precipitates are crystals or crystal-like amyloid fibrils, metastability seals the funnel. Strong agitation opening the seal is essential to disclosing the misfolding funnels.

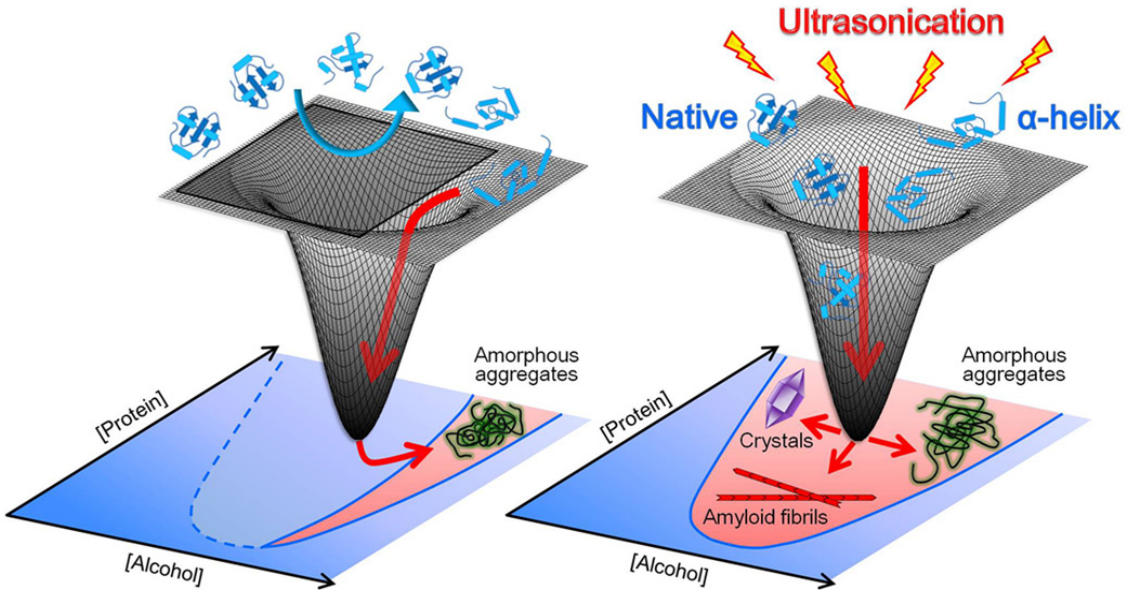

Figure 14. Solubility- and supersaturation-dependent protein misfolding funnels. The funnel shape defined by the equilibrium solubility depends on the type of alcohol. For HFIP and TFE, funnels are formed at around 12−16 and 40−80%, respectively. When the precipitates are crystals or crystal-like amyloid fibrils, metastability seals the funnel (left) and strong agitation such as ultrasonication (right) is essential to opening the funnel. When the precipitates are glassy amorphous aggregates, they appear spontaneously (left). The HFIP- and protein-concentration-dependent phase diagrams under supersaturation (left) and under equilibrium with ultrasonication (right) are shown at the bottom.

Chapter 3. Amorphous aggregation of cytochrome *c* with inherently low amyloidgenicity is characterized by the metastability of supersaturation and the phase diagram

3-1. Introduction

A failure in quality control is mostly accompanied by the formation of insoluble protein aggregates. Two types of aggregates are generally formed over the solubility limit and are discriminated by their conformational uniqueness, morphologies, and aggregation mechanisms.[30, 36, 91-93] One type of aggregate is the amyloid fibril. Mature amyloid fibrils comprise several protofilaments that accommodate ordered β-sheets stabilized by backbone hydrogen bonds between adjacent monomers.[15] The other form is the amorphous aggregate, which displays no characteristic morphology.[30, 36, 94]

In previous chapter, it has been shown that lysozyme whose amyloidgenic mutants in human are involved in hereditary systemic amyloidosis aggregated into distinct aggregates depending on alcohol concentration. Disease-unrelated myoglobin has been also shown to form amorphous aggregates and amyloid fibrils in the presence and absence of heme, respectively.[95, 96] Furthermore, apomyoglobin formed not only amyloid-like fibrils, but also amorphous aggregates in a manner that depended on the ligand species.[97] The lack of studies on the aggregation of proteins that accommodate cofactors and/or metals, and the similarity of Cyt*c* to myoglobin prompted us to investigate the aggregation behavior of Cyt*c*.

Cyt*c* shares several common features with myoglobin in that, for example, the two proteins are small α-helical globular proteins and contain a hydrophobic prosthetic group of heme for their functions.[98, 99] Moreover, in spite of extensive studies on the folding and function of Cyt*c*,[100-106] its aggregation behavior remains poorly understood. Previous studies reported that the release of Cyt*c* due to mitochondrial dysfunction was associated with Parkinson's disease[107] and apoptosis[103, 104], and

also that oligomeric Cyt*c* disrupted cell membranes,[108] implying a relationship between Cyt*c* aggregation and cytotoxicity.

I herein investigated the aggregation of Cyt*c* using an alcohol/water mixture and ultrasonication in an attempt to reveal intrinsic amyloidogenicity.[76, 91, 92] I also addressed the biological implications of Cyt*c* aggregation based on the physiologically relevant and distinct conformational states of holo and apo Cyt*c*. The aggregation of Cyt*c* and its fragment has also been discussed in terms of metastability and the degree of supersaturation. I proposed that the amorphous aggregation of proteins may be viewed as a generic property of proteins, and that a phase diagram constructed by a macroscopic view of thermodynamic solubility with the incorporation of a microscopic view of the secondary structure content of monomers and aggregates is useful for understanding the aggregation behaviors of proteins.

3-2. Materials and Methods

Chemicals. ThT and horse heart Cyt*c* were obtained from Wako Pure Chemical Industries, Ltd. (Osaka, Japan). Two types of alcohol, TFE and HFIP, $FeCl_3 \cdot 6H_2O$, and other reagents were purchased from Nacalai Tesque (Kyoto, Japan). The peptide fragment LIAYLK was synthesized by Toray Research Center, Inc. (Tokyo, Japan).

Preparation of holo Cytc (holoCytc), apo Cytc (apoCytc), and a fragment of Cytc. Silver-bound apo Cyt*c* (Ag-apoCyt*c*) and apoCyt*c* were prepared using horse heart Cytc based on the method proposed by Fisher et al.[100] The preparation of Ag-apoCyt*c* was initiated by adding silver sulphate (Ag_2SO_4) to holoCyt*c* in deionized water. The mixture was incubated at 40 °C overnight to ensure the replacement of thioether bonds between the heme moeity and two cysteine residues (Cys 14 and Cys 17) with silver mercaptide bonds between the thiol groups and Ag. After centrifugation at 22,300 *g* to remove the heme aggregates that precipitated, the supernatants of Ag-apoCyt*c* were collected and passed through a size exclusion column equilibrated with deionized water to further eliminate the remaining heme moieties.

ApoCyt*c* was prepared by adding 1 M dithiothreitol (DTT) and 6 M guanidine chloride to Ag-apoCyt*c* solutions in order to dissociate Ag from Ag-apoCyt*c* at 25 °C for 3 h in the dark. After removing the greenish yellow precipitates of Ag by centrifugation at 22,300 *g* for 30 min, the transparent supernatants of apoCyt*c* solutions were collected and then applied to a size exclusion column equilibrated with deionized water to exchange with salt-free water.

The concentrations of all Cyt*c* samples were determined with the molar extinction coefficients: 1.06×10^5 M^{-1} cm^{-1} at 410 nm for holoCyt*c*[109] and 1.09×10^4 M^{-1} cm^{-1} at 280 nm for Ag-apoCyt*c* and apoCyt*c*.[110] The samples of Ag-apoCyt*c* and apoCyt*c* were stored at -20 °C after lyophilization. Due to its slow dissolution, Ag-apoCyt*c* in deionized water was mostly used for various

measurements without lyophilization.

The concentration of the LIAYLK fragment was spectroscopically determined based on a molar extinction coefficient of 1490 M^{-1} cm^{-1} at 280 nm, which was calculated based on the sequence.[111]

Fluorescence spectroscopy. The tryptophan fluorescence values of holoCyt*c*, Ag-apoCyt*c*, and apoCyt*c* were measured with excitation at 295 nm using a Hitachi F4500 fluorescence spectrophotometer (Hitachi, Tokyo, Japan) at 37 °C. Emission profiles from 300 to 400 nm were recorded. The slit widths of excitation and emission were 5 and 10 nm, respectively. The protein concentration and path length of the quartz cuvette were 0.1 mg ml^{-1} and 0.5 cm, respectively.

Measurements of one-dimensional proton NMR. One-dimensional proton (^1H) NMR spectra of holoCyt*c*, Ag-apoCyt*c*, and apoCyt*c* were obtained using the AVANCE II-800 spectrometer (Bruker BioSpin, Germany) equipped with a cryogenic probe at 37 °C. A standard pulse sequence with water suppression by excitation sculpting (zgesgp from Bruker Topspin using the standard parameter set) was employed. Samples in deionized water containing 0.24 mg ml^{-1} of protein and 10% D_2O were used. Data were processed using TopSpin 3.2 (Bruker BioSpin, Germany).

Preparation of samples of Cytc and its fragment to monitor aggregation. HoloCyt*c*, apoCyt*c*, and the LIAYLK fragment at 15, 6, and 2 mg ml^{-1}, respectively, were initially dissolved in sodium acetate buffer (pH 4.8) with proper molar concentrations. The final concentration of sodium acetate was adjusted to 25 mM with the desired alcohol or iron concentrations. Ag-apoCyt*c* in deionized water was mixed with sodium acetate buffer (pH 4.8) and alcohols (TFE or HFIP) in order to reach the final concentration of 25 mM sodium acetate and desired alcohol or iron concentrations. The alcohol concentrations in this study were expressed by volume/volume (v/v). Further pH adjustments were not performed on the addition of alcohols to protein solutions.

Samples were incubated with and without ultrasonication at 37 °C. Regarding ultrasonic

irradiation, sample solutions in 1.5-ml Eppendorf tubes were placed at the center of a water bath-type ultrasonic transmitter (ELESTEIN SP070-PG-M; Elekon, Tokyo, Japan), and subjected to cycles of ultrasonication at 37 °C for 1 min at 2-min intervals throughout the experiments.

ThT assay and determination of residual monomer concentrations. A 5-μL aliquot of the sample solutions after reactions was mixed with 1 mL of 5 μM ThT in the 50 mM glycine-NaOH buffer (pH 8.5) as described in our previous studies.[91, 92] The ThT fluorescence intensity at 485 nm, excited at 445 nm, was measured using a Hitachi F4500 fluorescence spectrophotometer at 37 °C.

After being incubated, samples were centrifuged at 21,500 *g* for 30 min. The supernatants were collected and assayed spectrophotometrically using the absorbance and molar extinction coefficients described above.

Circular dichroism (CD) measurements. CD measurements were performed on a Jasco J820 spectropolarimeter (Tokyo, Japan) at 37 °C. The far-UV CD spectra of holoCyt*c*, Ag-apoCyt*c*, apoCyt*c*, and LIAYLK in 25 mM sodium acetate (pH 4.8) containing various alcohol concentrations were measured using a quartz cuvette with a 0.1-cm pathlength. The secondary structure content was estimated from the far-UV CD spectra by the BeStSel algorithm.[112]

Regarding near-UV CD experiments, protein samples were measured in 25 mM sodium acetate buffer (pH 4.8) without alcohol in a quartz cuvette with a 1-cm light path. A cell holder equipped with a water circulator was used to keep the sample temperature constant at 37 ℃. Spectra were presented as mean residue ellipticity, [θ] (deg cm^2 $dmol^{-1}$), after subtraction of the solvent background.

AFM measurements. Sample solutions after reactions were subjected to a 20-fold dilution. A 20-μL aliquot was then applied to a freshly-cleaved mica plate. After 1 min, the residual solution was blown off with compressed air and air-dried. Nano Scope IIIa (Bruker, Germany) was used for imaging, as reported previously.[92]

Fourier-transform infrared (FTIR) spectroscopy. FTIR measurements were carried out on a Bruker Equinox 55 (Bruker, Germany) instrument equipped with an MCT detector in CaF_2 cells with 100-μm teflon spacers. A total of 128 scans were accumulated in the 400-4000 cm^{-1} region with a 1-cm^{-1} resolution. In order to avoid the contribution of water vapor peaks to the spectra, the instrument was purged with dry-air. Cyt*c* samples were prepared either by dissolving the lyophilized protein in D_2O buffer or spinning down the sample prepared in normal buffers repeatedly in a TLA-100 (Beckman, USA) ultracentrifuge at 100,000 *g* and redissolving the pellet in a buffer containing D_2O. A protein concentration of approximately 4 mg ml^{-1} was used in the measurements. pD was determined before the addition of alcohol, as pD = pD* + 0.4, where pD* is the pH meter reading and 0.4 is the correction for the isotope effect. The recorded spectra were corrected by the subtraction of appropriate buffer spectra and the removal of remaining vapor peaks.

In order to estimate the secondary structure, peak fitting of the amide I' band (1600-1700 cm^{-1}) by Gaussian-shaped components was performed as described earlier.[26, 92, 93] The position and number of components were determined from the second derivative analysis of spectra. The width of the Gaussian curves was maximized in 15 cm^{-1}. Secondary structures were assigned to the corresponding components based on a previous study.[26] Fitting was carried out in the 1570-1730 cm^{-1} wavenumber range in order to appropriately treat the borders of the amide I region. Regarding comparisons of the spectral shape, spectra were normalized to have the same area in the 1600-1700 cm^{-1} region.

Isothermal titration calorimetry (ITC). Each Cyt*c* solution in 25 mM sodium acetate (pH 4.8) was degassed for 3 min before being loaded into the calorimeter. Calorimetric experiments were performed with a VP-ITC instrument (Malvern, UK) at 37 °C. In the injection syringe, 1 mM $FeCl_3 \cdot 6H_2O$ dissolved in 25 mM sodium acetate (pH 4.8) was titrated into 30 μM Cyt*c* (holoCyt*c* or apoCyt*c*) in the ITC cell. Titration experiments consisted of 40 injections spaced at intervals of 600

sec. The injection volume was 2 μl for the first injection and 7 μl for the remaining injections. The cell was continuously stirred at 307 rpm. Data was processed using the MicroCal Origin 7.0 software.

3-3. Results

Conformational characterization of the three Cytc types

In order to investigate the aggregation propensity of Cyt*c*, I first prepared the two apo forms of Cyt*c* from holoCyt*c*: apoCyt*c*, which was lacking heme held through two thioether bonds to cysteine 14 and 17, and Ag-apoCyt*c*, in which Ag atoms bound to cysteines instead of heme. I then performed a structural characterization of the three types of Cyt*c* using several approaches including CD, fluorescence, infrared, and solution-state NMR spectroscopies (Figure 1).

The far-UV CD spectrum of holoCyt*c* showed the typical pattern of an α-helix-rich conformation with a minimum at approximately 220 nm (Figure 1A). ApoCyt*c* and Ag-apoCyt*c* showed a minimum at approximately 200 nm without a characteristic peak, indicating that the secondary structures were largely unfolded, which is consistent with previous reports.[100, 105] The profile of the near-UV CD of holoCyt*c* displayed a unique spectrum with several peaks, suggesting that holoCyt*c* retained three-dimensional conformations. The low amplitudes of apoCyt*c* and Ag-apoCyt*c* in the near-UV spectra suggested that the two apo forms were mostly disordered (Figure 1B). The far- and near-CD spectra of the two apo proteins were slightly different.

The single tryptophan fluorescence of holoCyt*c* did not show an emission profile due to efficient energy transfer from the excited tryptophan at position 59 to the porphyrin ring (Figure 1C). This result indicated that interior heme was in close proximity to tryptophan in compactly-folded states.[100] However, the apo proteins both showed intense fluorescence, indicating the absence of heme. Wavelengths at the maximum intensity were different: 347 nm for apoCyt*c* and 341 nm for Ag-apoCyt*c*. Therefore, based on the blue shift from 347 to 341 nm, it was conceivable that tryptophan 59 was buried in a more hydrophobic environment upon the binding of Ag.

FTIR spectroscopy was also used for investigating structural states. The amide I region

(1600-1700 cm^{-1}) of the infrared spectra, which was mainly due to C=O stretching of the peptide backbone, was previously shown to be sensitive to the secondary structure.[113] HoloCyt*c* had a high α-helix content (Figure 1D and Table 1). The spectral maximum of the apo forms was shifted to the lower wavenumber region, revealing a more disordered structure. A comparison of Ag-apoCyt*c* and apoCyt*c* revealed a difference manifested in a higher β-sheet content with the appearance of the signal of an antiparallel β-sheet at approximately 1684 cm^{-1} (Figure 1D and Table 1).

One-dimensional ^{1}H NMR spectra provided further information on the distinct structural states of Cyt*c*s (Figure 1E, F). The spectrum of holoCyt*c* showed the wide distribution of peaks spanning from ~6 to ~10 ppm, suggesting folded structures (Figure 1E). On the other hand, apo proteins showed the narrow distribution of NMR peaks centered at ~8.5 ppm, indicative of largely unstructured states. Chemical shifts in the higher field region (< 0 ppm) arose from the hyperfine shift due to the iron of the heme (Figure 1F). Thus, the absence of hyperfine-shifted peaks in the apo proteins demonstrated the absence of heme. Although the global pattern of the spectra of two apo proteins was similar, some chemical shift regions such as 7.5-8.5 ppm and 1.0-1.5 ppm showed marked differences. Thus, the unfolded conformations of the apo forms were different, as was also revealed by CD, fluorescence, infrared data, and NMR results.

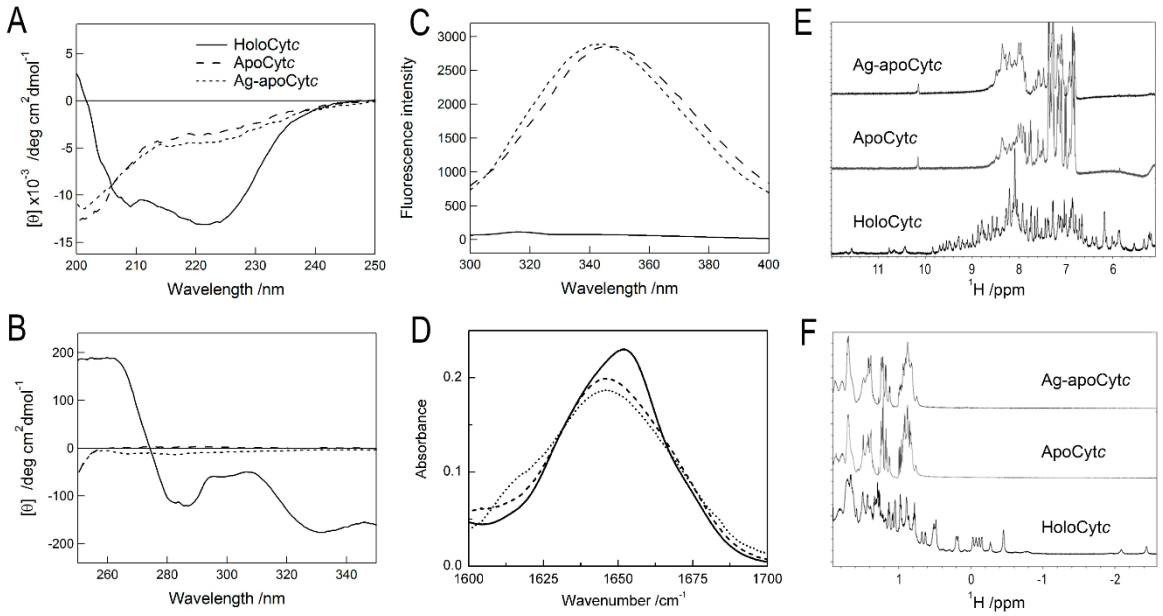

Figure 1. Structural characterization of the three Cyt*c* types**.** (A-D) CD spectra in the far (A) and near UV regions (B), emission profiles of tryptophan fluorescence (C), and infrared spectra in the amide I region (D) of holoCyt*c* (solid line), apoCyt*c* (dashed line), and Ag-apoCyt*c* (dotted line) in 25 mM sodium acetate buffer (pH 4.8) are shown (A-C), and in the same buffer in D_2O at 25 °C (D). (E,F) One-dimensional proton NMR spectra of the three Cyt*c* types in deionized water are displayed with corresponding labeling. Low and high field regions are separately presented for the main chain and aromatic residues (E) and the methyl groups of side chains for simplicity (F).

Table 1. Secondary structure analysis of various forms of Cyt*c* by infrared spectroscopy

HoloCyt*c*														
No alcohol			20% TFE (10 min)			20% TFE (15 h)			10% HFIP (10			10% HFIP (15 h)		
cm^{-1}	frac.[a]	str.[b]	cm^{-1}	frac.	str.	cm^{-1}	frac.	str.	cm^{-1}	frac.	str.	cm^{-1}	frac.	str.
1630	0.24	B	1628	0.13	B	1628	0.11	B	1630	0.07	B	1630	0.03	B
1642	0.18	R	1642	0.11	R	1641	0.11	R	1638	0.12	R/B	1637	0.28	R/B
1655	0.44	H	1651	0.64	H/R[c]	1650	0.66	H/R	1650	0.73	H/R	1652	0.61	H/R
1674	0.13	T	1675	0.12	T	1675	0.13	T	1677	0.08	T	1677	0.07	T
ApoCyt*c*														
No alcohol			30% TFE (10 min)			30% TFE (15 h)			10% HFIP (10			10% HFIP (15 h)		
1635	0.09	B	1624	0.05	B	1617	0.11	B	1631	0.04	B	1632	0.10	B
1646	0.53	R	1632	0.12	B	1638	0.35	R/B	1640	0.07	R/B	1638	0.03	R/B
1652	0.19	H	1649	0.76	R/H	1647	0.14	R	1648	0.78	R/H	1645	0.26	R
1672	0.19	T	1675	0.12	T	1654	0.21	H	1676	0.11	T	1651	0.48	H/R
						1673	0.19	T				1674	0.13	T
						1694	0.01	AP						
Ag-apoCyt*c*														
No alcohol			10% TFE (10 min)			10% TFE (15 h)			4% HFIP (10 min)			4% HFIP (15 h)		
1638	0.52	R/B	1617	0.13	B	1617	0.19	B	1617	0.14	B	1617	0.24	B
1646	0.05	R	1638	0.39	R/B	1638	0.40	R/B	1638	0.33	R/B	1638	0.26	R/B
1652	0.15	H	1650	0.24	R/H	1650	0.21	R/H	1649	0.32	R/H	1648	0.27	R/H
1669	0.28	T	1669	0.23	T	1671	0.19	T	1670	0.21	T	1654	0.01	H
1684	0.01	AP	1684	0.01	AP	1694	0.01	AP	1685	0.01	AP	1672	0.22	T
												1686	0.01	AP

Experiments were performed in D_2O containing 25 mM sodium acetate (pD 4.8) in the absence or presence of the given percentage of TFE or HFIP. Baseline- and vapor-corrected spectra were fit by Gaussians positioned at wavenumbers determined from the second derivatives of the spectra. [a]The fraction of the component and [b]assigned secondary structure are presented. The following abbreviations were used: B, β-sheet; H, α-helix; R, random coil; T, turn; AP, high frequency component suggesting the presence of an antiparallel β-sheet. [c]In several cases, it was difficult to distinguish a β-sheet from a random coil or a helix from a random coil when they were largely overlapping. In such cases, both structures were indicated.

Observation of holoCytc aggregation in alcohol and water mixtures

I examined the TFE- and HFIP-induced structural transitions of holoCyt*c* and its aggregation behaviors using CD spectroscopy and ultrasonication (Figures 2A-D and 3). A series of far-UV CD spectra of holoCyt*c* at various TFE concentrations were obtained just after sample preparation. CD spectra showed conformational transitions from the native states to TFE-induced helical states with an increase in TFE concentrations from 0 to 70%. In the absence of TFE, the CD spectrum of native holoCyt*c* displayed a pattern of α-helix-rich proteins with minima at 208 and 222 nm (Figure 1A). However, the spectrum at a TFE concentration of 20% showed a large increase in the CD signal at 208 nm (Figure 2A), which was suggestive of marked increases in α-helical structures, whereas the addition of TFE at a concentration of 10% TFE did not change the spectrum (Figures 2B and 3B). Increases in the concentration of TFE strengthened internal hydrogen bonds, thereby reorganizing structures to denatured states with open helical conformations, as was previously observed in our alcohol-induced conformational transitions of lysozyme[91] and insulin.[92] An increase in the concentration of TFE to 40% further increased the CD signal at 208 nm, and no significant changes were observed in CD spectra at higher TFE concentrations (Figures 2B and 3C-E). Thus, the conformational transition of holoCyt*c* occurred between TFE concentrations of 10 and 40% before the incubation, as shown in the transition curve against TFE concentrations (Figure 2B).

The far-UV CD spectra of holoCyt*c*, which was incubated for 15 h in the absence and presence of ultrasonication, were obtained at each TFE concentration (Figures 2A and 3). Ultrasonication is one of the most efficient inducers of amyloid fibrillation, which reveals the phenotype of protein aggregates in equilibrium.[76, 91, 92] Although slight changes were observed in spectra with the ultrasonication treatment at several TFE concentrations, no significant changes occurred in the CD spectra (Figure 2A). The concentrations of residual monomers after the incubation with ultrasonic irradiation were similar to those before the incubation (Figure 2B). A similar behavior

was observed using FTIR spectroscopy.

HoloCyt*c* exhibited some conformational changes upon the addition of TFE at a concentration of 20%. However, no further transition was observable after a 15-h incubation (Figures 4A). No aggregates were detectable on AFM images, consistent with the low ThT intensity (Figure 5A). These results indicated the absence of structural changes and aggregate formation of holoCyt*c*, even after the treatment with ultrasonication.

HFIP is also employed to examine the relationship between alcohol-induced structural changes and aggregation (Figures 2C and 3F-L). HFIP induced structural transitions to α-helix-rich states at lower concentrations than those of TFE, ranging from 4 to 20% (Figure 2D). The pattern of the spectrum at a HFIP concentration of 8% was similar to that at a TFE concentration of 20%, however, the lower CD signal resulted from rapid aggregation and precipitation (see below) (Figure 3G). This aggregation behavior was also observed at HFIP concentrations of 10, 12, and 16% (Figures 2C and 3H, I).

Further incubations at these HFIP concentrations led to decreases in CD signals, which stemmed from the progression of aggregation coupled with the precipitation of holoCyt*c* regardless of ultrasonication. The AFM images obtained showed amorphous aggregates without fibrillar species (Figures 5B, C) and the concentrations of the residual monomers and intensity of ThT fluorescence were markedly low (Figures 2D and 5B, C).

In contrast, at HFIP concentrations of 4% and higher in the range of 20-70%, no changes in CD spectra or the concentration of residual monomers were detected after a 15-h incubation with and without ultrasonication (Figures 2D, 3F, and J-L), which indicated that holoCyt*c* aggregates had not been formed.

I then investigated the effect of a HFIP concentration of 10% on holoCyt*c* by FTIR spectroscopy. A clear spectral change towards a more disordered structure was detected upon the

addition of HFIP (Figures 4B and Table 1). Precipitation was observed during the incubation, however, it did not result in significant changes in the spectral shape, suggesting that the structures in soluble monomers and insoluble amorphous aggregates were similar in the presence of a HFIP concentration of 10%

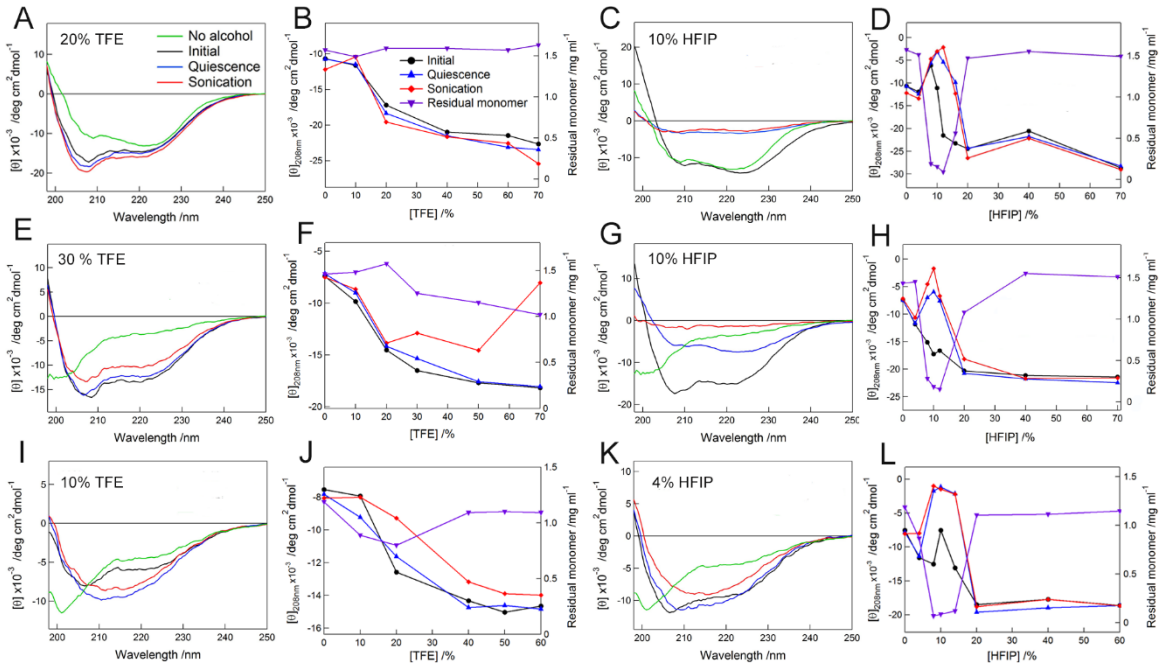

Figure 2. TFE or HFIP-dependent conformational transitions of the three Cyt*c* types with and without ultrasonication as monitored by CD spectroscopy. (A-L) The far-UV CD spectra and CD intensities at 208 nm of holoCyt*c* (A-D), apoCyt*c* (E-H), and Ag-apoCyt*c* (I-L) at the desired alcohol concentrations were recorded after a 5-min (black line and circle) and 15-h incubation following sample preparation without (blue line and triangle) or with ultrasonication (red line and circle), respectively. For comparison, the spectra of each Cyt*c* in the absence of alcohol are presented (green line). The concentrations of residual monomers (the right axis) after the treatment with ultrasonication in B, D, F, H, J, and L are also shown with the purple line and inverted triangle.

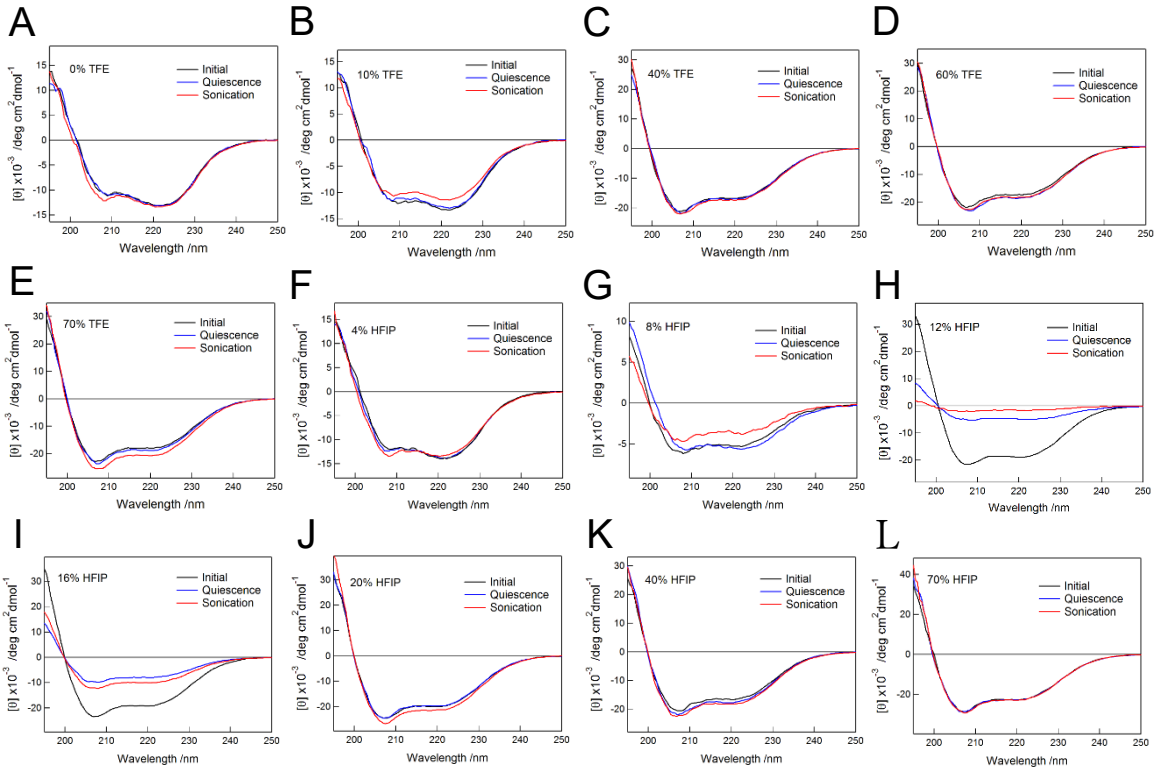

Figure 3. Alcohol-dependent aggregation of holoCyt*c* monitored by far-UV CD. Far-UV CD spectra of holoCyt*c* at ~5 mins (black lines) and 15 h when incubated without (blue lines) and with ultrasonication (red lines) after sample preparation were determined in the presence of TFE concentrations of 0% (A), 10% (B), 40% (C), 60% (D), 70% (E); or HFIP concentrations of 4% (F), 8% (G), 12% (H), 16% (I), 20% (J), 40% (K), and 70% (L).

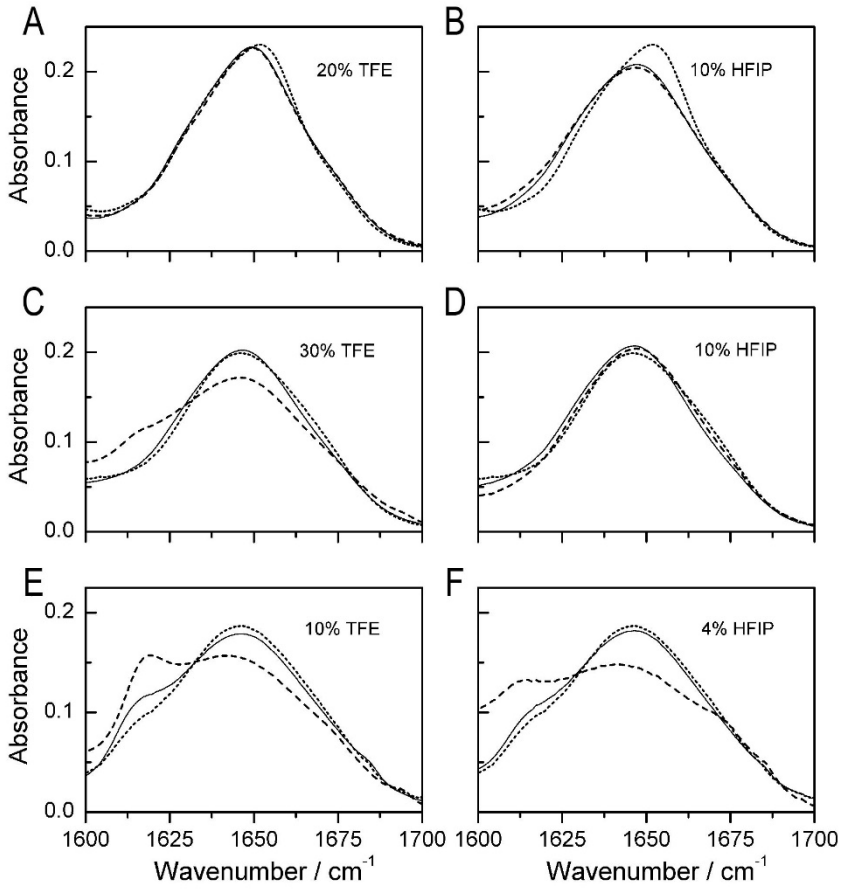

Figure 4. TFE or HFIP induced conformational changes in Cyt*c*s as followed by FTIR spectroscopy. (A-F) Infrared spectra in the amide I region are presented for holoCyt*c* (A, B), apoCyt*c* (C, D), and Ag-apoCyt*c* (E, F). Spectra measured after sample preparation (~10 min) and after a 15-h incubation with ultrasonication are presented with solid and dashed lines, respectively. As a comparison, the spectra of the corresponding Cyt*c* forms in the absence of alcohol are also presented (dotted lines). Experiments were performed in D_2O and in 25 mM sodium acetate buffer (pD 4.8) in the presence of TFE or HFIP as indicated in the panels.

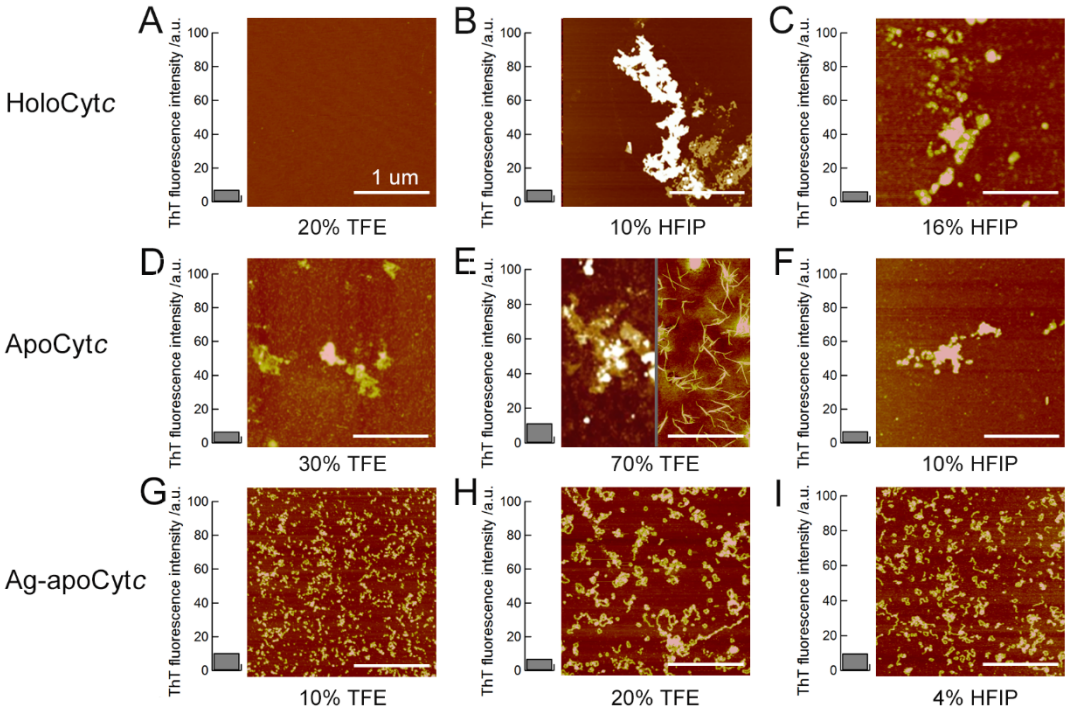

Figure 5. Morphological and tinctorial characterization of Cyt*c* aggregates formed after the ultrasonication treatment. (A-I) AFM images (right) and the ThT fluorescence of Cyt*c* (left) under distinct alcohol concentrations are shown for holoCyt*c* (A-C), apoCyt*c* (D-F), and Ag-apoCyt*c* (G-I). The concentrations of TFE or HFIP used are displayed below the AFM images. The white scale bars indicate 1 μm.

Investigation of the aggregation propensity of Cytc through the removal of heme

I examined changes in the structure and aggregation properties of apoCyt*c* as a function of TFE (0, 10, 20, 30, 50, and 70%) and HFIP (0, 4, 8, 12, 20, 40, and 70%) concentrations in the absence and presence of ultrasonication (Figures 2E-H and 6). Increases in TFE concentrations from 0 to 70% were accompanied by the conformational transition of apoCyt*c* from random coils to α-helices, as observed by increases in CD signals at 208 nm (Figures 2E, F, and 6A-E). The structural transition was in the TFE concentration range of 10-50% (Figure 2F), which was similar to that of holoCyt*c* (Figure 2B). An incubation for 15 h without ultrasonication did not change the CD spectra, which indicated that the conformations at each TFE concentration were stable (Figures 2E, F and 6A-E).

A 15-h incubation under the ultrasonication treatment with a TFE concentration greater than 30% decreased ellipticity with the loss of 20-30% of soluble proteins (Figures 2F and 6D, E), which suggested the formation of aggregates. I performed AFM measurements and the ThT assay in order to investigate aggregation (Figures 5D, E). At TFE concentrations of 30, 50, and 70%, the AFM image obviously showed the formation of amorphous aggregates with low ThT fluorescence (Figures 5D, E left), which indicated the absence of mature amyloid fibrils. However, although ThT fluorescence was low at a TFE concentration of 70% and similar to that at 30%, the AFM image sometimes also showed the formation of amyloid fibrils (Figure 5E, right). Considering a typical CD spectrum, which represented α-helical structures, it was conceivable that amyloid fibrils formed on the mica surface when AFM samples were being prepared. Accordingly, I concluded that apoCyt*c* formed amorphous aggregates in solutions at a TFE concentration greater than 30%.

Infrared spectroscopy of apoCyt*c* in the presence of a TFE concentration of 30% indicated a small abrupt change in the spectral shape upon the addition of TFE and an increase in the β-sheet content upon aggregation, which was accelerated by ultrasonication with the appearance of the high frequency antiparallel β-sheet component (Figures 4C and Table 1). I noted that the protein

concentration applied was higher (4 mg ml^{-1}) in these experiments, which increased the fraction of aggregates, than in CD measurements.

Because around 70% of the total concentration of monomers remained after the formation of aggregates (Figure 2F), approximately 30% monomers formed aggregates. It is conceivable that decreases in the CD intensity at 70% TFE arose from large aggregates. However, FTIR results revealed information on the secondary structures of aggregates irrespective of the size of aggregates.

The addition of HFIP also more effectively induced a conformational transition and the aggregation of apoCyt*c* than TFE (Figures 2G, H, and 6F-K). As HFIP concentrations were increased, unfolded apoCyt*c* was converted to an α-helix-rich conformation with a minimum at 208 nm. This apparent transition was observed in a HFIP concentration range of 4-20% (Figure 2H), which again indicated the stronger effects of HFIP than TFE. At HFIP concentrations of 4 and 20-70%, no significant changes were observed in the CD spectra after a 15-h incubation, even with the ultrasonic treatment, or in the concentrations of residual monomers, which suggested that apoCyt*c* remained soluble without aggregation.

However, apoCyt*c* was more likely to aggregate at HFIP concentrations of 8-12% (Figures 2G, and 6G, H). After a quiescent incubation of 15 h at HFIP concentrations of 8 and 10%, the CD spectrum of apoCyt*c* showed a minimum at approximately 225 nm with a decrease in ellipticity at 208 nm, which was not a typical CD spectrum of the cross-β structures of mature amyloid fibrils (Figures 2G and 6G). Ultrasonication with the same incubation period induced further decreases in CD signals with the same pattern of the spectrum to that recorded before the incubation, which revealed the formation of different types of amorphous aggregates generated without ultrasonication. The formation of amorphous aggregates at a HFIP concentration of 10% was also revealed based on decreases in the concentrations of residual monomers (Figure 2H), low ThT fluorescence, and the observation of amorphous aggregates in the AFM image (Figure 5F). In the infrared spectrum of

apoCyt*c* in the presence of a HFIP concentration of 10%, I did not observe a significant increase in the β-sheet content, even if the aggregation process was clear with the accumulation of insoluble material. This also indicated the formation of amorphous aggregates in the presence of HFIP (Figures 4D and Table 1).

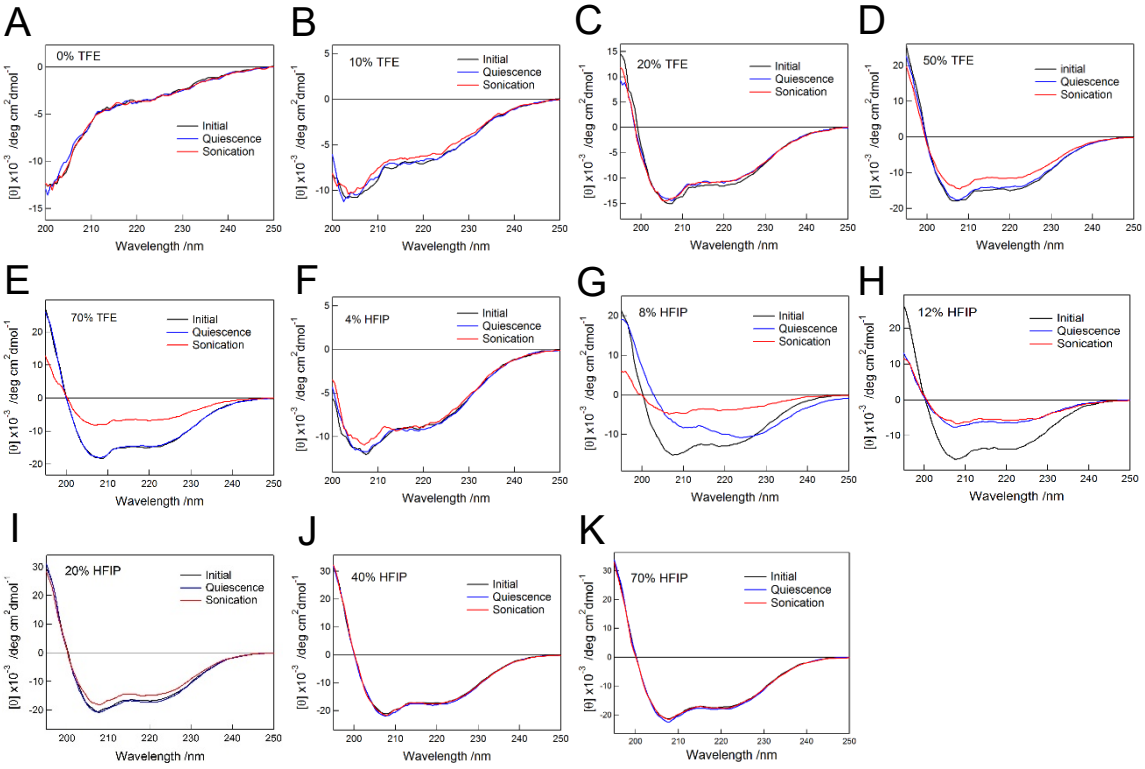

Figure 6. Alcohol-dependent aggregation of apoCyt*c* monitored by far-UV CD. Far-UV CD spectra of apoCyt*c* at ~5 mins (black lines) and 15 h when incubated without (blue lines) and with ultrasonication (red lines) after sample preparation were determined in the presence of TFE concentrations of 0% (A), 10% (B), 20% (C), 50% (D), 70% (E); or HFIP concentrations of 4% (F), 8% (G), 12% (H), 20% (I), 40% (J), and 70% (K).

Investigation of the aggregation of Ag-bound apoCytc

Structural transitions in Ag-apoCyt*c* that depended on TFE concentrations (10, 20, 40, 50, and 60%) and ultrasonication were initially examined (Figures 2I, J, and 7A-E). Changes in initial CD spectra obtained after sample preparation and cooperative transition were similar to those of apoCyt*c*. Increases in TFE concentrations induced alcohol-denatured α-helix-rich structures with a minimum at approximately 208 nm, and transition was observed between TFE concentrations of 10 and 40%. Although no significant changes were noted in CD spectra at TFE concentrations of 40, 50, and 60% regardless of the ultrasonic treatment, marked changes were detected at TFE concentrations of 10 and 20% after a 15-h incubation (Figures 2I and 7B).

Under a quiescent incubation with TFE at a concentration of 10%, the CD spectrum showed a single minimum at approximately 215 nm, which represented the formation of β-structure-rich conformations. The incubation with ultrasonication did not markedly change the CD spectrum. The AFM image suggested the formation of short curvilinear fibrillar aggregates, i.e., immature fibrils or protofibrils (Figure 5G). Since the amount of residual monomers was reduced to 80%, approximately 20% of the protein molecules were considered to aggregate into fibrillar aggregates. I then examined the time-dependent aggregation of Ag-apoCyt*c* in TFE at concentration of 10% (Figure 8). The intensity of ThT fluorescence and light scattering gradually increased without a lag time. No significant difference was observed in kinetics in the absence or presence of ultrasonication, suggestive of aggregation of non-mature amyloid fibrils.[114] These results indicated the formation of the immature fibrils of Ag-apoCyt*c* at a TFE concentration of 10%.

The aggregation behaviors of Ag-apoCyt*c* in TFE at a concentration of 20% were similar to those at 10% (Figures 5H and 7B). Although a quiescent incubation for 15 h did not change the CD spectrum, ultrasonication altered the CD spectrum of unfolded Ag-apoCyt*c* to that of a fibrillar conformation with a single minimum at approximately 215 nm (Figure 7B). AFM images revealed the

formation of thin and flexible fibrillar aggregates (Figure 5H), which was consistent with the tinctorial property of the low ThT fluorescence of immature fibrillar aggregates.[114] Although a large amount of monomers were still soluble, approximately 20% monomers were incorporated into fibrillar aggregates (Figure 2J).

In the presence of a TFE concentration of 10% at a higher protein concentration (4 mg ml^{-1}), Ag-apoCyt*c* exhibited an altered infrared spectrum with an increased β-sheet content, which indicated an antiparallel β-sheet. The sample incubated under ultrasonication showed further increases in the β-sheet content with the growth of a component at 1617 cm^{-1} in the spectrum (Figure 4E and Table 1), which was consistent with the CD results. The formation of an antiparallel β-sheet was previously reported in the immature fibrils of β_2-microglobulin, while the mature fibrils of proteins often consisted of a parallel β-structure.[26, 112]

HFIP also effectively induced structural transition and clarified the aggregation tendencies of Ag-apoCyt*c* in the concentration range of 0-60% (Figures 2K, L, and 7F-K). As the HFIP concentration increased, HFIP-induced structural transitions to the α-helix with a minimum at 208 nm were observed in the CD spectra. At HFIP concentrations of 20, 40, and 60%, CD spectra obtained promptly after sample preparation were similar to those after a 15-h incubation with and without ultrasonication (Figure 7I-K).

Ag-apoCyt*c* was still soluble even after ultrasonication with a HFIP concentration greater than 20%. I investigated the aggregation propensity of Ag-apoCyt*c* at a HFIP concentration less than 20% in more detail (4, 8, 10, and 14%). Aggregation was pronounced at low HFIP concentrations. CD spectra that suggested the formation of aggregates after an incubation for 15 h were obtained at HFIP concentrations of 4, 8, 10, and 14%. At 4%, the CD spectrum that showed a minimum at approximately 210 nm was changed to that of β-structures. An incubation combined with the ultrasonic treatment resulted in the CD spectrum of a typical β-structure (Figure 2K) with a decrease in the concentration

of residual monomers to 80% (Figure 2L). Furthermore, since the intensity of ThT fluorescence was very low and thin and flexible fibrillar aggregates were observed in the AFM image (Figure 5I), I concluded that fibrillar aggregates formed at a HFIP concentration of 4%. On the other hand, the CD signals and concentration of residual monomers at 8, 10, and 14% were markedly decreased and this may have been due to the formation of amorphous aggregates (Figures 2L and 7F-H). Infrared spectroscopy of Ag-apoCyt*c* at a concentration of 4 mg ml^{-1} in HFIP at a concentration of 4% verified the formation of a β-sheet rich structure, which was consistent with the CD measurements (Figures 4F and Table 1).

Compared to Ag ions, weak interactions of iron ions (Figure 9) which are physiologically more relevant than Ag did not change the secondary structures of the two types of Cyt*c* (holoCyt*c* and apoCyt*c* (Figure 10) and did not influence aggregation behaviors by keeping solubility of each Cyt*c* (Figure 10), implying that binding affinity for metal ions and structural changes by ion binding would be also important for aggregation.

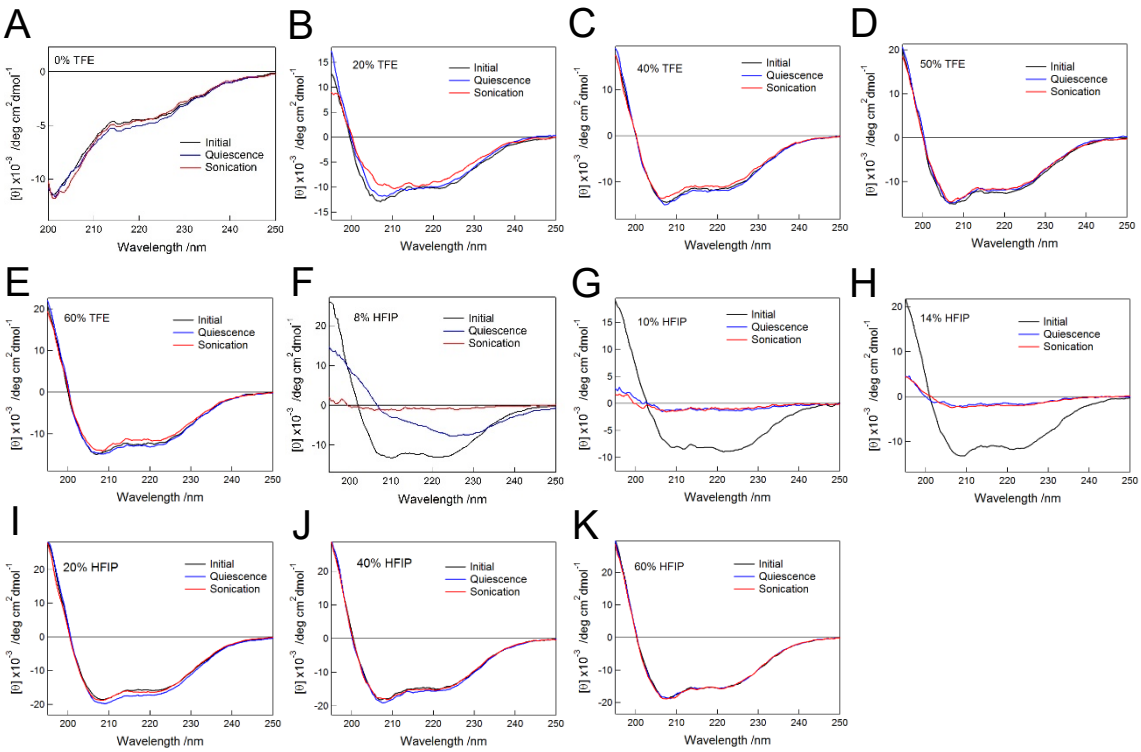

Figure 7. Alcohol-dependent aggregation of Ag-apoCyt*c* monitored by far-UV CD. Far-UV CD spectra of Ag-apoCyt*c* at ~5 mins (black lines) and 15 h when incubated without (blue lines) and with ultrasonication (red lines) after sample preparation were determined in the presence of TFE concentrations of 0% (A), 20% (B), 40% (C), 50% (D), 60% (E); or HFIP concentrations of 8% (F), 10% (G), 14% (H), 40% (I), 20% (J), and 70% (K).

A

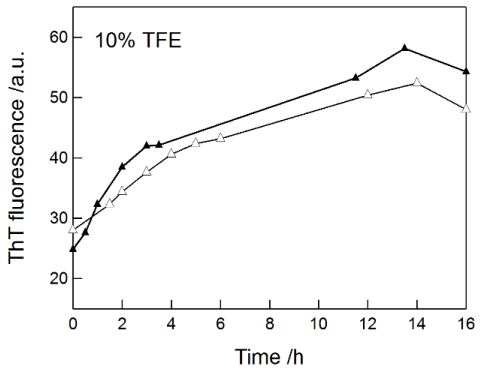

B

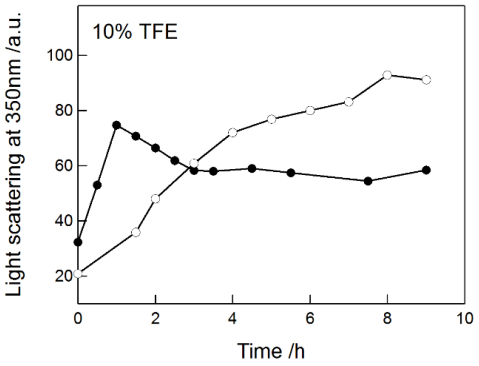

Figure 8. Aggregation kinetics of Ag-apoCyt*c* at a TFE concentration of 10%. The process of Ag-apoCyt*c* aggregating into protofibrils was monitored by ThT fluorescence (A) and light scattering (B) with (▲, ●) and without sonication (Δ, ○).

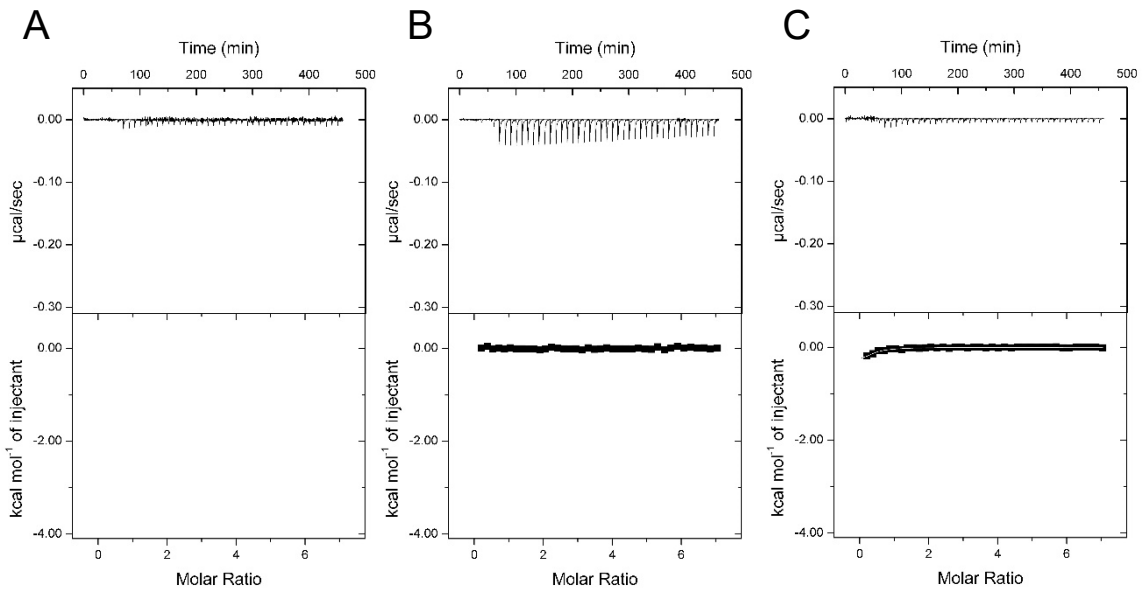

Figure 9. Intermolecular interactions between the two types of Cyt*c* and iron examined by ITC. (A-C) ITC thermograms of the titration of Fe^{3+} to 25 mM sodium acetate buffer (pH 4.8) (A), holoCyt*c* (B), and apoCyt*c* (C) are shown in the upper panel. Normalized heat values were plotted against the molar ratio ([Fe^{3+}]/[Cyt*c*]) in the lower panel. Thermodynamic parameters of iron binding to Cyt*c* could not be determined due to too weak intermolecular interaction.

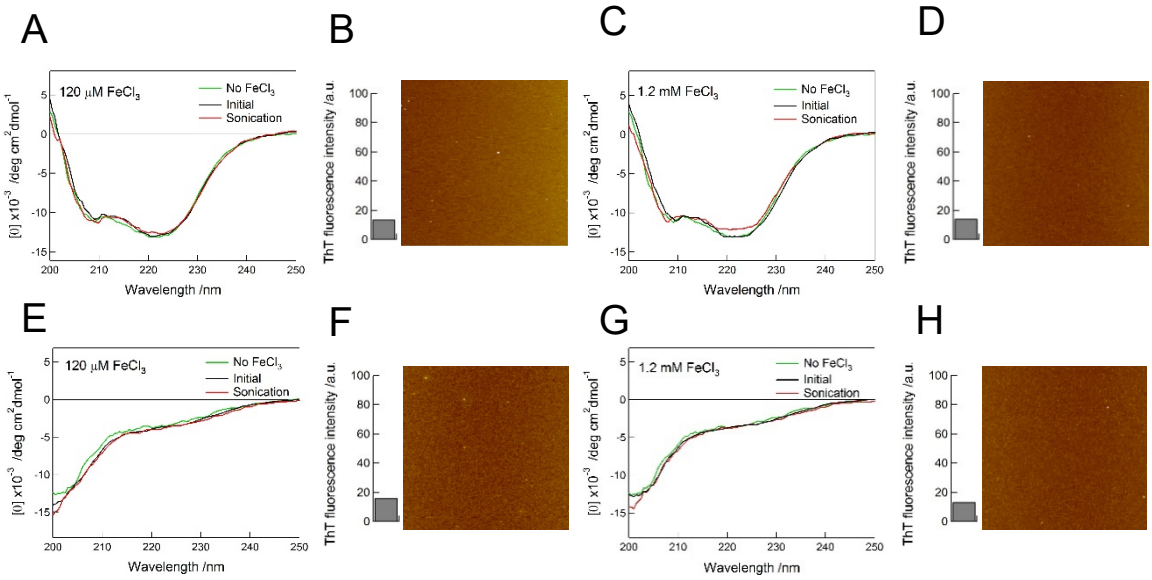

Figure 10. Effects of iron on the aggregation of the physiologically relevant two types of Cyt*c* monitored by far-UV CD, ThT fluorescence, and AFM. (A, C, E, and G) Far-UV CD spectra of holoCyt*c* (A, C) and apoCyt*c* (E, G) in the presence of 120 μM (A and E) or 1.2 mM (C and G) iron ions are shown. The CD spectra were recorded at ~5 mins (black lines) and 15 h when incubated with ultrasonication (red lines) after sample preparation. For comparison, the spectra of each Cyt*c* in the absence of iron ions are also presented (green line). The concentration of Cyt*c* for incubation was 120 μM. (B, D, F, and H) The ThT fluorescence (left) and AFM images and of Cyt*c* (right) in the presence of 120 μM (B and F) or 1.2 mM (D and H) irons after 15 h incubation with ultrasonication. The white scale bars indicate 1 μm.

The predicted amyloidgenic fragment of Cytc did not form amyloid fibrils

Eisenberg and co-workers hypothesized that practically every protein contains amyloidogenic segments.[14] In order to investigate the amyloid-forming capability of specific regions of Cyt*c* which might be concealed by other regions, I evaluated the aggregation propensity of Cyt*c* residues using various computational algorithms, which were mainly based on the physicochemical properties of amino acid residues (Figure 11). Three out of the ten algorithms, including Waltzt,[13] did not identify any amyloidogenic regions in Cyt*c*.

By considering the charged residue for the solubility of a fragment and the aromatic residue for the concentration determination using spectroscopy, I selected the region L94- K99 (LIAYLK) from the three best predicted aggregation-prone regions (residues K8-K13, M80-G84, and L94-K99) (Figure 12A). As expected, the far-UV CD spectrum of the L94-K99 fragment exhibited the typical profile of unfolded proteins in the absence of alcohol (Figure 12B). Increases in the concentration of TFE or HFIP from 0 to 40% led to increases in the CD signals at approximately 218 nm with a low amplitude, which suggested a transition to β- sheet-rich structures (Figures 12 and 13). Due to the short length of the fragment (6 residues), small soluble aggregates of β-strands formed through intermolecular interactions.

No significant changes were observed in the CD spectra after a 15-h incubation in the absence or presence of ultrasonication, whereas those at HFIP concentrations of 4 and 20% were distinct. Furthermore, the concentration of residual monomers did not show a significant decrease (Figure 12D, H) and no particles were detected in AFM images (Figure 12E, I), indicating that large aggregates had not formed. Markedly low ThT fluorescence suggested that the L94-K99 fragment did not form amyloid fibrils (Figure 12E, I).

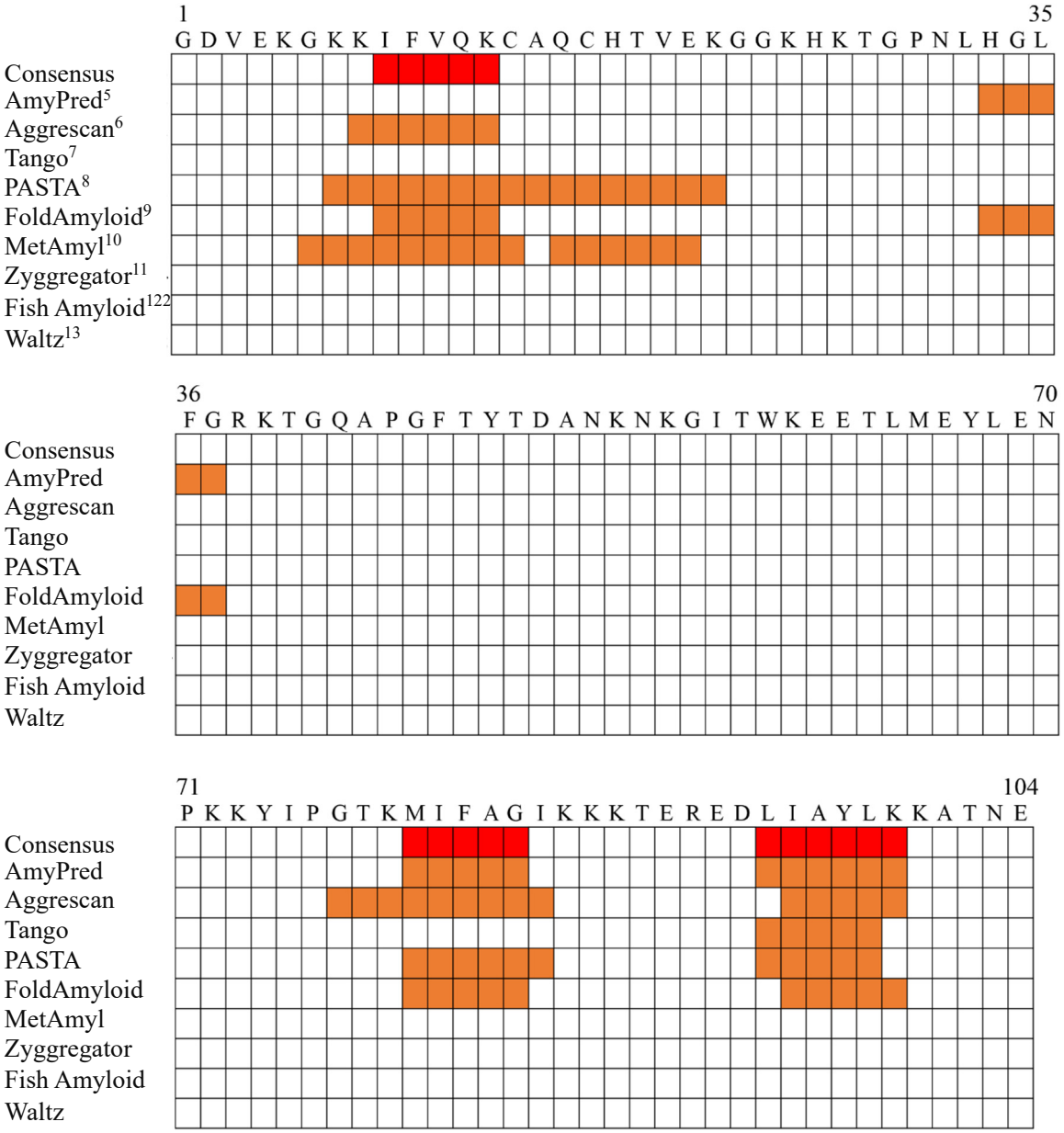

Figure 11. Predictions of aggregation-prone regions in horse heart Cyt*c* using various computational algorithms. An orange color indicates the predicted regions prone to form amyloid fibrils. Default values and thresholds were used for predictions. A red color indicates the consensus region with amyloidgenicity between different algorithms.

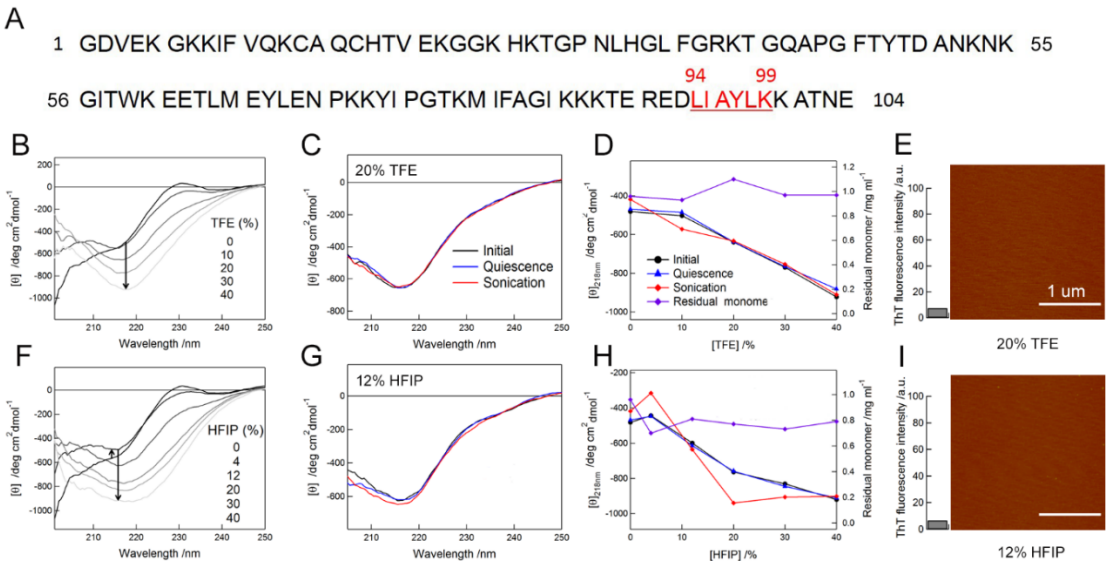

Figure 12. TFE or HFIP-dependent conformational transitions of the Cyt*c* fragment with and without ultrasonication as monitored by CD spectroscopy. (A) The amino acid sequence of horse heart Cyt*c* is shown. The residues corresponding to the fragment used here are marked in a red color and residue number. (B, F) The far-UV CD spectra of the LIAYLK fragment measured immediately (5 min) after sample preparation at TFE concentrations of 0, 10, 20, 30, and 40% (B) or at HFIP concentrations of 0, 4, 12, 20, 30, and 40% (F). (C, G) The far-UV CD spectra at a TFE concentration of 20% (C) and a HFIP concentration of 12% (G) were obtained after a 5-min (black curve) and 15-h incubation following sample preparation in the absence (blue curve) and presence of ultrasonication (red curve). (D, H) CD signals at 208 nm (left axis) and the concentration of residual monomers (right axis) were plotted against the concentrations of TFE (D) and HFIP (H), respectively. (E, I) AFM images of fragments after the ultrasonication treatment at a TFE concentration of 20% (E) and a HFIP concentration of 12% (I). The white scale bars indicate 1 μm.

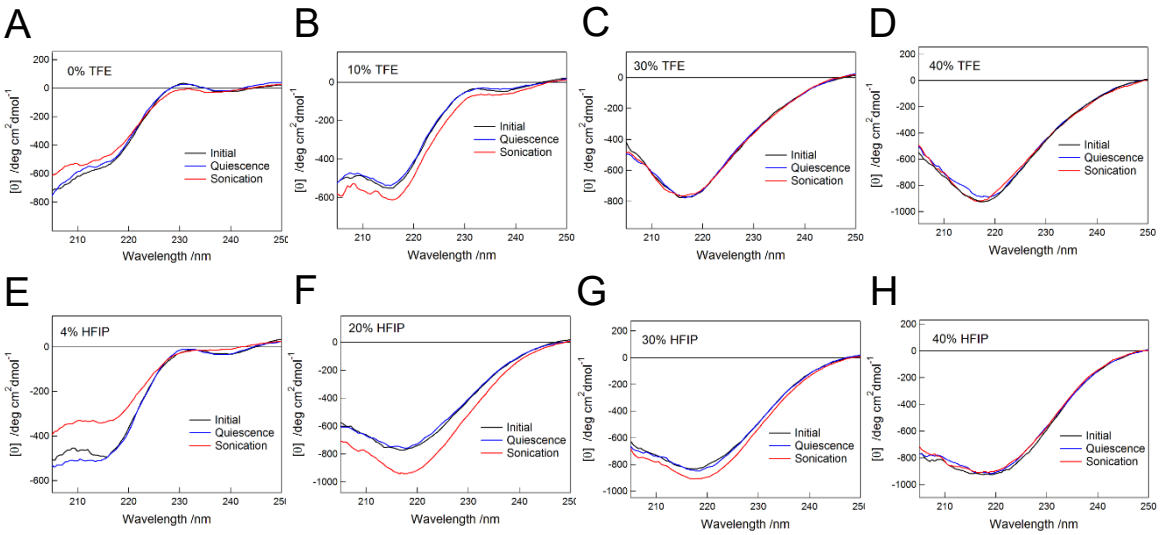

Figure 13. Alcohol-dependent aggregation of LIAYLK monitored by far-UV CD. Far-UV CD spectra of LIAYLK at ~5 mins (black lines) and 15 h when incubated without (blue lines) and with ultrasonication (red lines) after samples preparation were determined in the presence of TFE concentrations of 0% (A), 10% (B), 30% (C), 40% (D); or HFIP concentrations of 4% (E), 20% (F), 30% (G), and 40% (H).

3-4. Discussion

Amorphous aggregation of Cytc with inherently low amyloidogenicity and its biological implications

Cyt*c* is a multi-functional protein for electron transfer[102, 106] and signal transduction of apoptosis.[103, 104] Functional native Cyt*c* which consists of structural ensembles in bulk solution samples nonfunctional unfolded conformations, which are more prone to aggregation than folded states. Thus, misfolding and aggregation deactivate Cyt*c* by shifting the equilibrium to non-native conformations, thereby disrupting protein homeostasis in cells. ApoCyt*c* prepared here represented a heme-free apo form of unfolded Cyt*c* that exists during the biogenesis and maturation of Cyt*c*.[115] Ag-apoCyt*c* may reflect a conformational state where metal ions strongly bound to apoCyt*c*. Therefore, an investigation on Cyt*c* aggregation is important for obtaining a deeper understanding of the folding and function of Cyt*c* based on protein and redox homeostasis.

By using two biologically relevant molecular species of Cyt*c* and apo Cyt*c* mimicking metal-bound states, I revealed the detailed aggregation behaviors of Cyt*c* with alcohol and ultrasonication. Regardless of the distinct conformations of monomers depending on the TFE concentration (Figures 2B and 14A left panel), no aggregates formed due to the high solubility of holoCyt*c* (see the final part of discussion), however, a propensity for amorphous aggregation was observed in HFIP-mixed solutions (Figures 2D and 14A right panel). Although no clear definition on the type of protein aggregates is available, for simple comparison, I here define that amorphous aggregates include partially structured aggregates such as oligomers with β structures and protofibrils and soluble aggregates with the small size and molecular weights, and exclude mature amyloid fibrils based on their kinetic aspects.[30, 91, 92, 116] The low aggregation propensity of holoCyt*c* implied that once Cyt*c* matured to a holo form, it exhibited increased folding efficiency by minimizing irreversible aggregation.

Reinforced hydrophobic interactions among denatured holoCyt*c* with a hydrophobic heme induced rapid amorphous aggregation due to the formation of a large number of hetero-nuclei (Figure 14A right panel). Similarly, recent studies have also shown that the addition of heme altered the aggregation pathway of α-synuclein from amyloid fibrillation to oligomer-like amorphous aggregation[117] and favored the formation of amorphous aggregates of apomyoglobin by inhibiting of amyloid fibrillation.[96] This amorphous aggregation was often observed at high concentrations of neutral or kosmotropic salts[30, 116] and high temperatures.[118]

ApoCyt*c* largely increased the propensity for amorphous aggregation (Figures 2F, J, and 14B). The removal of heme significantly disrupted the native conformation of Cyt*c* (Figure 1) and markedly increased hydrophobicity by exposing a large number of hydrophobic residues in the interior of Cyt*c* and around heme. Ag-apoCyt*c* also showed large changes in aggregation behavior with an increased propensity for fibrillar aggregates. The binding of Ag was suggested to have altered the conformation of apoCyt*c* (Figure 1) to be more appropriate for the formation of fibrillar aggregates. This may imply that biased hydrophobic forces to induce amorphous aggregation were reduced by structural changes.

Solid surfaces showed a similar effect to metals. The formation of amyloid-like fibrils in the AFM image (Figure 5E, right) may be explained by the adapted conformation of apoCyt*c* to the rugged surfaces of the mica for productive nucleation of amyloid fibrillation. Similarly, membrane mimetics and the addition of SDS induced the formation of the amyloid-like fibrils of Cyt*c*.[119, 120] The extensive ultrasonic treatment of the three Cyt*c* types did not induce the formation of mature amyloid fibrils (Figure 14), however, ultrasonication is highly effective for revealing the hidden propensity of amyloid formation by promoting productive nucleation.[30, 76, 91, 92] Even the fragment of Cyt*c*, which was predicted to be the most amyloidogenic region (Figure 11 and 12A), did not form mature amyloid fibrils (Figure 12).

Taken together, these results suggested an intrinsically low propensity for the amyloid fibrillation of Cyt*c* and implied that amorphous aggregates including partially structured aggregates such as oligomers and protofibrils and soluble aggregates were more likely to be formed than amyloid fibrils. Since amorphous aggregation is stochastically easier than amyloid formation, the formation of amorphous aggregates may also be viewed as a generic property of proteins. Furthermore, since amyloid fibrils are more stable than amorphous aggregates,[116, 121] the amyloid fibrillation of Cyt*c*, which decreases the turnover of Cyt*c*, is disadvantageous for maintaining proteostasis. The well-designed maturation process of Cyt*c* may attempt to circumvent the binding of metals or membranes to apoCyt*c* in order to decrease amyloidogenicity. The inherently low amyloidogenicity of Cyt*c* may eventually be beneficial for homeostasis in cells.[122, 123]

Finally, the comparison of aggregation of Cyt*c* and myoglobin will be interesting and useful for understanding general aspects of heme-containing α-helical proteins. As apomyoglobin forms amorphous aggregates, protofibrils, and mature fibrils by controlling the solvent conditions such as pH and temperature and adding small hydrophobic ligands or salts,[95-97] apoCyt*c* may form mature amyloid fibrils under certain conditions.

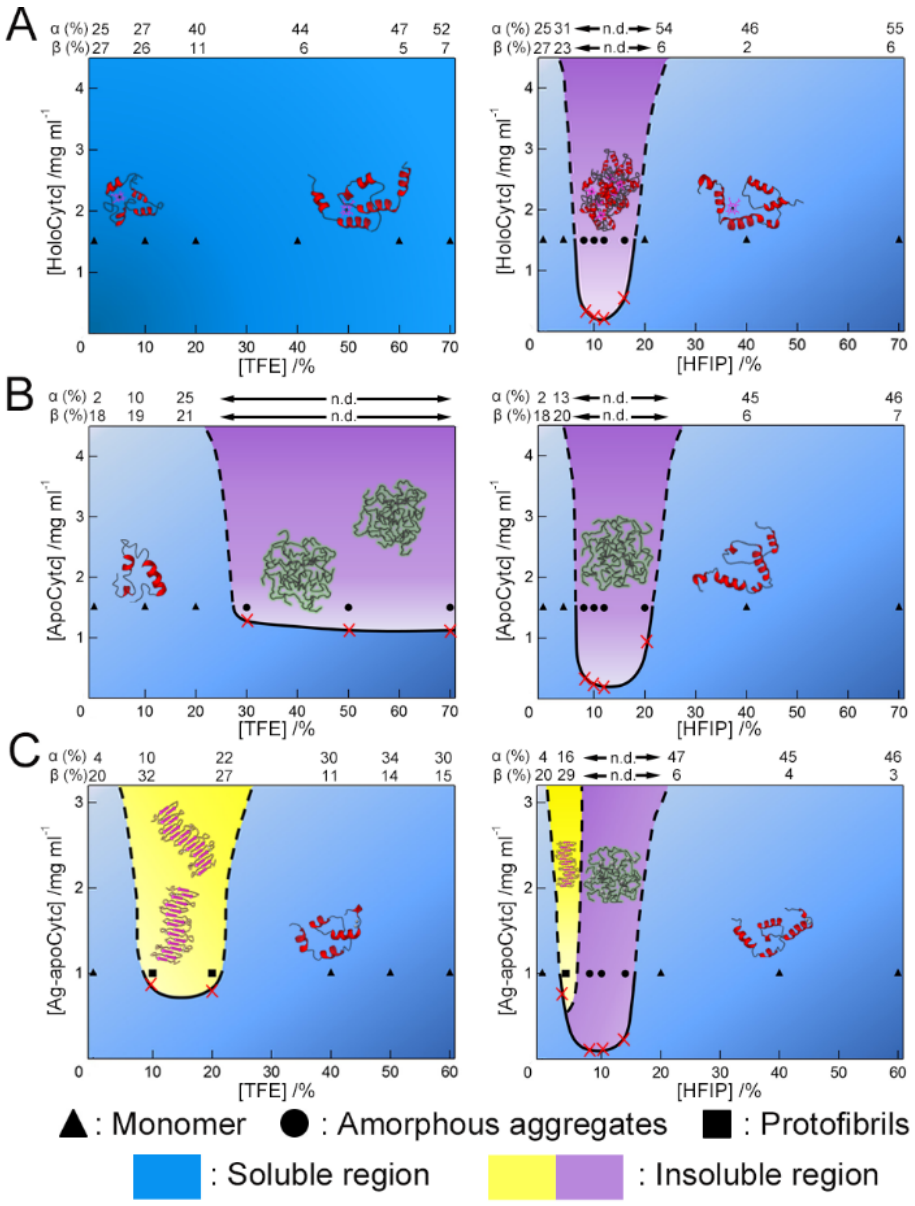

Figure 14. Comprehensive phase diagrams of Cyt*c* aggregation. (A-C) The phase states of holoCyt*c* (A), apoCyt*c* (B), and Ag-apoCyt*c* (C) in the water/alcohol mixture after the ultrasonication treatment. The soluble and insoluble solid states are represented by symbols as well as a color code and its gradation. The triangles (▲), circles (●), and rectangles (■) display monomers, amorphous aggregates, and fibrillar aggregates, respectively. Red symbols (×) indicate the concentrations of residual monomers. In order to obtain a better understanding, the regions of soluble monomers, amorphous

aggregates, and fibrillar aggregates are also represented in blue, magenta, and yellow, respectively. The denser a color, the more possible the existence of a molecular species. The curves at each phase diagram indicate solubility curves. The solid and dashed lines signify high and low reliabilities, respectively, based on the actual data obtained experimentally in the present study. The molecular species that existed at each condition are schematically shown. The secondary structure contents of the three Cyt*c* types after ultrasonication, which were predicted from the CD spectra by the BeStSel algorithm,[112] are shown at the top of each phase diagram. α and β indicate the contents of the α-helix and β-sheet in percentages, respectively. ″n.d.″ is shown in cases, in which the secondary structure content was not be predicted due to the low CD intensity from aggregation and precipitation.

The metastability of supersaturation-discriminated protein aggregation: amorphous aggregation and amyloid fibrillation

Phase transitions in soluble proteins to solids such as protein aggregates occur when protein concentrations exceed their solubility limit (Figures 2 and 14).[30, 71, 91, 92] Thus, decreases in solubility are a fundamental driving force for a phase transition, as shown in the solubility curves of Cyt*c*, lysozyme, and insulin in phase diagrams (see the next section) (Figures 14 and 15). The physical phenomenon of the metastability of supersaturation needs to be considered in phase transition because aggregation occurs by overcoming supersaturated states in which proteins maintain soluble states, even over the solubility limit (Figure 15A, C).

Although the degree of supersaturation continues to increase with elevations in protein concentrations,[124] the metastability of supersaturation for productive nucleation, which corresponds to a kinetic energy barrier, is maximal just above the solubility limit and decreases with higher protein concentrations. The higher metastability of supersaturation with a low degree of supersaturation maintains kinetically-trapped soluble states, while the lower metastability with a high degree of supersaturation leads to amorphous aggregation including partially structured aggregates. The probability of productive nucleation is maximal at a balanced metastability and degree of supersaturation. Therefore, the metastability of supersaturation plays a key role in kinetically dominating nucleation-dependent amyloid fibrillation. Although the degree of supersaturation was predictable when aggregates, amorphous aggregates or amyloid fibrils, formed (Table 2), no clear correlation between aggregation propensity and the degree of supersaturation was observed, which suggests that the metastability of supersaturation is a more critical factor than the degree of supersaturation in determining the aggregation and aggregate type.

Strong agitation such as ultrasonication effectively induces amyloid fibrils by disrupting the metastability of supersaturation, thereby revealing the true equilibrium between fibrils and residual

monomers (Figure 15B, D). However, amorphous aggregation including partially structured aggregates generally occurs more rapidly than amyloid fibrillation without a recognizable lag time in typical experimental time scales due to the low metastability of supersaturation, as observed in the kinetics of the fibrillar aggregation of Ag-apoCyt*c* in 10% TFE (Figure 8), thereby kinetically discriminating amyloid fibrillation and amorphous aggregation.[30, 91, 92] Therefore, low amyloidogenicity vs. a higher propensity for the amorphous aggregation of Cyt*c* is explained by the low metastability of supersaturation. Metal or membrane binding may increase the metastability of supersaturation for productive nucleation of amyloid formation with balancing the degree of supersaturation.

Proper H-bond networks play an essential role in the formation of nuclei with critical sizes by overcoming hydration energy.[125] Balanced hydrophobic and electrostatic intermolecular forces as well as structural properties to compensate for the entropic costs of molecular associations are also determining factors for productive nucleation. These factors may control the metastability of supersaturation. Hydrophobic interactions that are too strong form non-productive nuclei with less H-bonds in an irregular manner, which are incompatible with the well-ordered structure of amyloid fibrils. Strong repulsive electrostatic interactions increase solubility while favoring hydration energy. The amorphous aggregation of the Cyt*c* fragment suggested that the prediction of the metastability of supersaturation is not easy based on the primary sequence alone since the sequence analysis of Cyt*c* is based on algorithms trained to recognize amyloid propensity in metal-free proteins. Metastability of supersaturation in metalloproteins might be different from that of metal- or cofactor-free proteins.

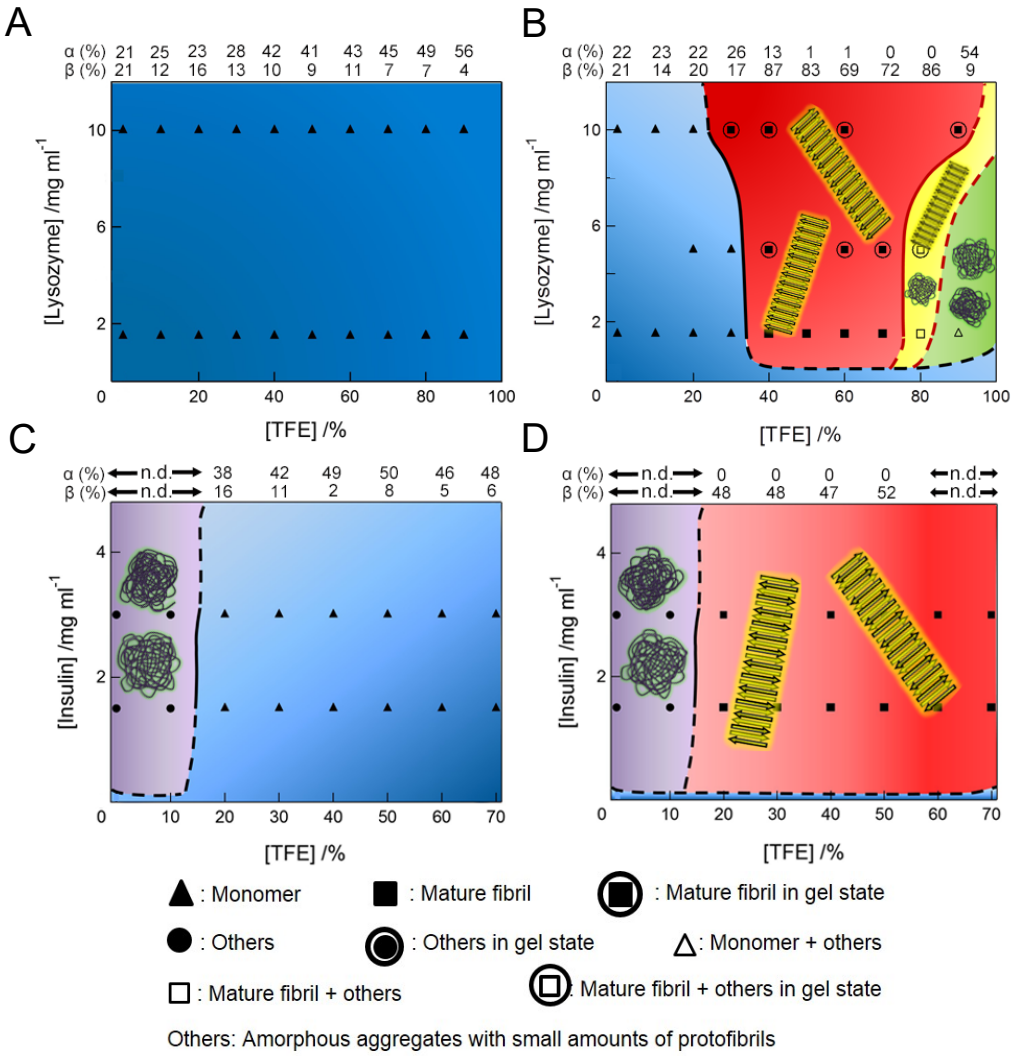

Figure 15. Phase diagrams of the aggregation of lysozyme and insulin in TFE/water mixtures. Phase diagrams of lysozyme (A and B) and insulin (C and D) at pH 4.8 before (A and C) and after ultrasonication (B and D) in TFE/water mixtures. Dominant species detected at various TFE concentrations are indicated by symbols. The secondary structure contents of lysozyme and insulin, predicted by the BeStSel algorithm[112] from far-UV CD spectra, at 1.5 mg ml^{-1} are noted at the top of the phase diagrams. α and β indicate the α-helical and β-sheet contents, respectively. Ambiguous results due to aggregation and precipitation are marked with "n.d." The phase diagram of lysozyme after ultrasonication (B) was reproduced with slight modifications (Chapter 2 Figure 13) and the figures (A, C, and D) were newly constructed based on our previous findings.[91, 92]

Table 2. Summary of the degree of supersaturation of protein solutions

			Degree of supersaturation (σ)
HoloCyt*c*	No alcohol		n.d.
	TFE	10%	n.d.
		20%	n.d.
		40%	n.d.
		60%	n.d.
		70%	n.d.
	HFIP	4%	n.d.
		8%	6.9
		10%	8.7
		12%	15.7
		16%	1.7
		20%	n.d.
		40%	n.d.
		70%	n.d.
ApoCyt*c*	No alcohol		n.d.
	TFE	10%	n.d.
		20%	n.d.
		30%	0.2
		50%	0.3
		70%	0.5
	HFIP	4%	n.d.
		8%	4.4
		10%	7.3
		12%	9.0
		20%	0.4
		40%	n.d.
		70%	n.d.
Ag-apoCyt*c*	No alcohol		n.d.
	TFE	10%	0.1
		20%	0.3
		40%	n.d.
		50%	n.d.
		60%	n.d.
		4%	0.2

Lysozyme	HFIP	8%	14.0
		12%	10.8
		14%	7.3
		20%	n.d.
		40%	n.d.
		60%	n.d.
	No alcohol		n.d.
	TFE	10%	n.d.
		20%	n.d.
		30%	n.d.
		40%	36.5
		50%	74.0
		60%	74.0
		70%	79.0
		80%	n.d.
		90%	1.6
Insulin	No alcohol		23.8
	TFE	10%	66.3
		20%	47.8
		30%	156.1
		40%	1413.2
		50%	87.4
		60%	n.d.
		70%	51.4

The degree of supersaturation (σ) of the three types of Cyt*c*s, lysozyme, and insulin in 25 mM sodium acetate buffer (pH 4.8) with and without the given percentage of TFE or HFIP was predicted by the following equation:

$$\sigma = (C - C^*) / C^*$$

where C and C^* are the protein concentration used and the protein solubility, respectively. C^* corresponds to the concentration of residual protein monomers at the end of aggregation reaction. “n.d.” is shown in cases, in which the protein solutions are unsaturated or the concentration of residual monomers cannot be determined. Our previous results were used for the calculation of lysozyme[91] and insulin.[92]

Phase diagrams provide a comprehensive understanding of protein aggregation

Phase diagrams are schematic representations that comprehensively illustrate the physical state of solutes depending on ambient conditions. Thus, they have been widely employed to explain the processes and conditions of protein crystallization.[67, 125, 126] In recent studies, I successfully showed that phase diagrams are a powerful tool for describing protein aggregation using lysozyme (Chapter 2 Figure 13) and insulin[92] in alcohol/water mixtures. Phase diagrams provided a macroscopic view of protein aggregation based on the solubility and metastability of supersaturation and illustrated the context-dependent types of aggregates. Ultrasonication interrupted the high metastability of supersaturation, which trapped soluble lysozyme and insulin at certain alcohol concentrations (Figure 15A, C), and, thus, amyloid fibrils formed in equilibrium (Figure 15B, D), whereas amorphous aggregates including partially structured aggregates rapidly formed and did not depend on the ultrasonic treatment (Figure 15C, D).

I herein constructed phase diagrams for the aggregation of the three Cyt*c* types (Figure 14A-C) in order to clearly illustrate the aggregation behavior of Cyt*c*. Aggregation patterns and solubility curves differed depending on the type and concentration of alcohol as well as the type of Cyt*c*. Although the alcohol concentrations at which aggregates formed and the types of aggregates in HFIP mixtures were all similar (Figure 14 right panels), those in TFE-mixed solutions were markedly different (Figure 14 left panels).

HoloCyt*c* showed high solubility at all TFE concentrations with no aggregation or amorphous aggregation at HFIP concentrations of 8%-16% (Figure 14A). ApoCyt*c* exhibited amorphous aggregation at TFE concentrations greater than 30% and HFIP concentrations of 8%-20% (Figure 14B). Partially structured fibrillar aggregates of Ag-apoCyt*c* formed at TFE concentrations of 10%-20% and at a HFIP concentration of 4% with amorphous aggregation at HFIP concentrations of 4-14% (Figure 14C). As shown in the phase diagrams of the three Cyt*c* types in TFE/water mixtures,

the transition from folded states to unfolded states clearly decreased the solubility of Cyt*c*, resulting in the aggregation of two apo forms. On the other hand, the aggregation-driving capability of HFIP was much stronger than that of TFE with lower protein solubility resulting in lower residual monomer concentrations in HFIP solutions. The alcohol concentration ranges promoting aggregation were wider in TFE solutions. Thus, protein solubility, a fundamental thermodynamic factor in protein aggregation, is closely related to conformational states of proteins which alter the phase diagram of protein aggregation.

In order to link a microscopic structural property to a macroscopic property of the solubility and aggregation pattern, I plotted the content of helical and β structures against alcohol concentrations (Figures 14 and 15). A comparison of the phase diagrams of Cyt*c*, lysozyme, and insulin showed that no clear correlation existed between the content of α-helices or β-strands and the propensity for aggregation was obtained. Hence, these results demonstrated that local microscopic differences in protein conformations, even with a similar secondary structure content and solubility, were also important for determining the aggregation pathway between amorphous aggregation, including fibrillar aggregates, and amyloid fibrils.

A phase diagram-based investigation of protein aggregation will be useful in other aggregation studies by revealing aggregation behavior and will also be beneficial for the development of effectors of aggregation by controlling the solubility/metastability of supersaturation and inducing selectively-desired aggregates based on the hydrophobic and electrostatic balance. Atomic-level approaches such as NMR spectroscopy and molecular dynamic simulations will be useful for obtaining deeper insights into the relation between protein conformations and types of aggregates.

Chapter 4. Conclusion

In the last decade, protein aggregation has become increasingly a hot topic in diverse research fields due to its ability to cause a number of severe human pathologies and its potential applications to biological and bioinspired materials. So far, most of studies have been focused on how environmental factors, including temperature, organic solvent, liposome surface, etc., regulate protein aggregation based on microscopic viewpoints. In contrast, understanding of the mechanism underlying protein aggregation from macroscopic viewpoints is still limited. In this thesis, I examined the aggregation of lysozyme (Chapter 2) and Cytc (Chapter 3) in alcohol/water mixtures and provided new macroscopic insights into protein aggregation.

In the second chapter, I revealed that the presence of moderate concentrations of alcohol, in particular TFE or HFIP, decreased markedly solubility of lysozyme with the concurrent alcohol-induced denaturation. However, the metastability of supersaturation kept denatured lysozyme soluble. Disrupting metastability using strong agitation like ultrasonication resulted in the production of crystal-like amyloid fibrils. The concept of solubility and supersaturation-trapped amyloid fibrillation will be generally applied to amyloidogenesis even under physiological conditions. In contrast, at high concentrations of ethanol, amorphous aggregation of lysozyme occurred rapidly due to low metastability of supersaturation. On the basis of this new view, I further proposed a protein misfolding funnel which is useful for explaining aggregation of proteins. This protein misfolding funnel will also be applicable for preparing crystalline precipitates of native proteins.

In the third chapter, I demonstrated the intrinsically low tendency of amyloid formation of Cyt*c*. Cyt*c* and its segment over the solubility limit, i.e., in supersaturated states, formed easily amorphous aggregates and protofibrils without appreciable lag time due to the low metastability of supersaturation. In spite of similar solubility among three types of Cyt*c*, each type of Cyt*c* showed distinct aggregating behaviors as macroscopically represented in the phase diagram of Cyt*c* aggregation, which suggested that a microscopically different conformation of Cyt*c* was also a critical

factor to determine the aggregation pathway. Thus, I proposed that the phase diagram which incorporated macroscopic and microscopic characters of proteins provided straightforward understanding of protein misfolding and aggregation.

Although lysozyme and Cyt*c* are obviously different proteins with distinct amino acid sequences, function and structures, their aggregation behaviors share a general mechanism: the concentration of proteins which exceeds over its solubility limit is a thermodynamic prerequisite for protein aggregation and the metastability of supersaturation is a critical kinetic determinant for the formation of mature amyloid fibrils. Finally, I expect that the macroscopic mechanism of protein aggregation proposed here will be common to aggregation of other proteins and peptides, and will contribute to the deeper understanding of protein aggregation from a new perspective.

References

1. C. B. Anfinsen, *Science*, 1973, **181**, 223-230.
2. F. Chiti and C. M. Dobson, *Annu. Rev. Biochem.*, 2006, **75**, 333-366.
3. J. D. Sipe, M. D. Benson, J. N. Buxbaum, S. Ikeda, G. Merlini, M. J. Saraiva and P. Westermark, *Amyloid*, 2012, **19**, 167-170.
4. C. M. Dobson, *Nature*, 2003, **426**, 884-890.
5. A. C. Tsolis, N. C. Papandreou, V. A. Iconomidou and S. J. Hamodrakas, *PLoS One*, 2013, **8**, e54175.
6. O. Conchillo-Sole, N. S. de Groot, F. X. Aviles, J. Vendrell, X. Daura and S. Ventura, *BMC Bioinformatics*, 2007, **8**, 65.
7. A. M. Fernandez-Escamilla, F. Rousseau, J. Schymkowitz and L. Serrano, *Nat Biotechnol.*, 2004, **22**, 1302-1306.
8. A. Trovato, F. Seno and S. C. Tosatto, *Protein Eng. Des. Sel.*, 2007, **20**, 521-523.
9. S. O. Garbuzynskiy, M. Y. Lobanov and O. V. Galzitskaya, *Bioinformatics*, 2010, **26**, 326-332.
10. M. Emily, A. Talvas and C. Delamarche, *PLoS One*, 2013, **8**, e79722.
11. G. G. Tartaglia, A. P. Pawar, S. Campioni, C. M. Dobson, F. Chiti and M. Vendruscolo, *J. Mol. Biol.*, 2008, **380**, 425-436.
12. P. Gasior and M. Kotulska, *BMC Bioinformatics*, 2014, **15**, 54.
13. S. Maurer-Stroh, M. Debulpaep, N. Kuemmerer, M. Lopez de la Paz, I. C. Martins, J. Reumers, K. L. Morris, A. Copland, L. Serpell, L. Serrano, J. W. Schymkowitz and F. Rousseau, *Nat. Methods*, 2010, **7**, 237-242.
14. L. Goldschmidt, P. K. Teng, R. Riek and D. Eisenberg, *Proc. Natl. Acad. Sci. U.S.A.*, 2010, **107**, 3487-3492.
15. D. Eisenberg and M. Jucker, *Cell*, 2012, **148**, 1188-1203.
16. J. L. Jimenez, E. J. Nettleton, M. Bouchard, C. V. Robinson, C. M. Dobson and H. R. Saibil, *Proc. Natl. Acad. Sci. U.S.A.*, 2002, **99**, 9196-9201.
17. F. E. Cohen and J. W. Kelly, *Nature*, 2003, **426**, 905-909.
18. V. N. Uversky and A. L. Fink, *Biochim. Biophys. Acta*, 2004, **1698**, 131-153.
19. T. P. Knowles and R. Mezzenga, *Adv. Mater.*, 2016, **28**, 6546-6561.
20. S. Bolisetty and R. Mezzenga, *Nat. Nanotechnol.*, 2016, **11**, 365-371.
21. C. Li and R. Mezzenga, *Nanoscale*, 2013, **5**, 6207-6218.
22. D. M. Fowler, A. V. Koulov, C. Alory-Jost, M. S. Marks, W. E. Balch and J. W. Kelly, *PLoS Biol.*, 2006, **4**, e6.

23. D. M. Fowler, A. V. Koulov, W. E. Balch and J. W. Kelly, *Trends Biochem. Sci.*, 2007, **32**, 217-224.
24. S. K. Maji, M. H. Perrin, M. R. Sawaya, S. Jessberger, K. Vadodaria, R. A. Rissman, P. S. Singru, K. P. Nilsson, R. Simon, D. Schubert, D. Eisenberg, J. Rivier, P. Sawchenko, W. Vale and R. Riek, *Science*, 2009, **325**, 328-332.
25. G. Bhak, J. Lee, T. H. Kim, S. Lee, D. Lee and S. R. Paik, *Biochem. J.*, 2014, **464**, 259-269.
26. J. Kardos, D. Okuno, T. Kawai, Y. Hagihara, N. Yumoto, T. Kitagawa, P. Zavodszky, H. Naiki and Y. Goto, *Biochim. Biophys. Acta*, 2005, **1753**, 108-120.
27. C. J. Roberts, T. K. Das and E. Sahin, *Int. J. Pharm.*, 2011, **418**, 318-333.
28. M. Sugiyama, N. Fujii, Y. Morimoto, K. Itoh, K. Mori, T. Fukunaga and N. Fujii, *Chem. Biodivers.*, 2010, **7**, 1380-1388.
29. A. Soragni, S. Yousefi, C. Stoeckle, A. B. Soriaga, M. R. Sawaya, E. Kozlowski, I. Schmid, S. Radonjic-Hoesli, S. Boutet, G. J. Williams, M. Messerschmidt, M. M. Seibert, D. Cascio, N. A. Zatsepin, M. Burghammer, C. Riekel, J. P. Colletier, R. Riek, D. S. Eisenberg and H. U. Simon, *Mol. Cell*, 2015, **57**, 1011-1021.
30. Y. Yoshimura, Y. X. Lin, H. Yagi, Y. H. Lee, H. Kitayama, K. Sakurai, M. So, H. Ogi, H. Naiki and Y. Goto, *Proc. Natl. Acad. Sci. U.S.A.*, 2012, **109**, 14446-14451.
31. K. Shiraki, K. Nishikawa and Y. Goto, *J. Mol. Biol.*, 1995, **245**, 180-194.
32. N. Hirota, K. Mizuno and Y. Goto, *Protein Sci.*, 1997, **6**, 416-421.
33. M. Buck, *Q. Rev. Biophys.*, 1998, **31**, 297-355.
34. D. P. Hong, M. Hoshino, R. Kuboi and Y. Goto, *J. Am. Chem. Soc.*, 1999, **121**, 8427-8433.
35. M. Hoshino, Y. Hagihara, D. Hamada, M. Kataoka and Y. Goto, *FEBS Lett.*, 1997, **416**, 72-76.
36. K. Yanagi, M. Ashizaki, H. Yagi, K. Sakurai, Y. H. Lee and Y. Goto, *J. Biol. Chem.*, 2011, **286**, 23959-23966.
37. E. J. Cohn, W. L. Hughes, Jr. and J. H. Weare, *J. Am. Chem. Soc.*, 1947, **69**, 1753-1761.
38. M. Okuda, Y. Uemura and N. Tatsumi, *Prep. Biochem. Biotechnol.*, 2003, **33**, 239-252.
39. S. Yamamoto, I. Yamaguchi, K. Hasegawa, S. Tsutsumi, Y. Goto, F. Gejyo and H. Naiki, *J. Am. Soc. Nephrol.*, 2004, **15**, 126-133.
40. F. Chiti, N. Taddei, M. Bucciantini, P. White, G. Ramponi and C. M. Dobson, *EMBO J.*, 2000, **19**, 1441-1449.
41. K. Yamaguchi, H. Naiki and Y. Goto, *J. Mol. Biol.*, 2006, **363**, 279-288.
42. V. L. Anderson, W. W. Webb and D. Eliezer, *Phys. Biol.*, 2012, **9**, 056005.
43. I. Pallares, J. Vendrell, F. X. Aviles and S. Ventura, *J. Mol. Biol.*, 2004, **342**, 321-331.
44. S. Srisailam, T. K. Kumar, D. Rajalingam, K. M. Kathir, H. S. Sheu, F. J. Jan, P. C. Chao and C. Yu, *J. Biol. Chem.*, 2003, **278**, 17701-17709.

45. E. Rennella, A. Corazza, S. Giorgetti, F. Fogolari, P. Viglino, R. Porcari, L. Verga, M. Stoppini, V. Bellotti and G. Esposito, *J. Mol. Biol.*, 2010, **401**, 286-297.
46. Y. Fezoui and D. B. Teplow, *J. Biol. Chem.*, 2002, **277**, 36948-36954.
47. E. Chatani, H. Yagi, H. Naiki and Y. Goto, *J. Biol. Chem.*, 2012, **287**, 22827-22837.
48. S. Kumar and J. B. Udgaonkar, *Biochemistry*, 2009, **48**, 6441-6449.
49. A. Sekhar and J. B. Udgaonkar, *Biochemistry*, 2011, **50**, 805-819.
50. G. Plakoutsi, N. Taddei, M. Stefani and F. Chiti, *J. Biol. Chem.*, 2004, **279**, 14111-14119.
51. C. J. Barrow, A. Yasuda, P. T. Kenny and M. G. Zagorski, *J. Mol. Biol.*, 1992, **225**, 1075-1093.
52. H. Shao, T. Nguyen, N. C. Romano, D. A. Modarelli and J. R. Parquette, *J. Am. Chem. Soc.*, 2009, **131**, 16374-16376.
53. D. Ivnitski, M. Amit, O. Silberbush, Y. Atsmon-Raz, J. Nanda, R. Cohen-Luria, Y. Miller, G. Ashkenasy and N. Ashkenasy, *Angew. Chem. Int. Ed. Engl.*, 2016, **55**, 9988-9992.
54. S. Manchineella, V. Prathyusha, U. D. Priyakumar and T. Govindaraju, *Chemistry*, 2013, **19**, 16615-16624.
55. H. Naiki, N. Hashimoto, S. Suzuki, H. Kimura, K. Nakakuki and F. Gejyo, *Amyloid*, 1997, **4**, 223-232.
56. Y. Yoshimura, K. Sakurai, Y. H. Lee, T. Ikegami, E. Chatani, H. Naiki and Y. Goto, *Protein Sci.*, 2010, **19**, 2347-2355.
57. P. B. Stathopulos, G. A. Scholz, Y. M. Hwang, J. A. Rumfeldt, J. R. Lepock and E. M. Meiering, *Protein Sci.*, 2004, **13**, 3017-3027.
58. Y. Ohhashi, M. Kihara, H. Naiki and Y. Goto, *J. Biol. Chem.*, 2005, **280**, 32843-32848.
59. E. Chatani, Y. H. Lee, H. Yagi, Y. Yoshimura, H. Naiki and Y. Goto, *Proc. Natl. Acad. Sci. U.S.A.*, 2009, **106**, 11119-11124.
60. K. Sakamoto, M. Kamiya, M. Imai, K. Shinzawa-Itoh, T. Uchida, K. Kawano, S. Yoshikawa and K. Ishimori, *Proc. Natl. Acad. Sci. U.S.A.*, 2011, **108**, 12271-12276.
61. H. Ogi, Y. Tomiyama, Y. Shoji, T. Mizugaki and M. Hirao, *Jpn. J. Appl. Phys.*, 2006, **45**, 4678-4683.
62. H. Kitayama, Y. Yoshimura, M. So, K. Sakurai, H. Yagi and Y. Goto, *Biochim. Biophys. Acta*, 2013, **1834**, 2640-2646.
63. J. R. Thomas, *J. Phys. Chem*, 1959, **63**, 1725-1729.
64. E. Webster, *Ultrasonics*, 1963, **1**, 39-48.
65. E. K. Hill, B. Krebs, D. G. Goodall, G. J. Howlett and D. E. Dunstan, *Biomacromolecules*, 2006, **7**, 10-13.
66. S. Yamamoto, K. Hasegawa, I. Yamaguchi, S. Tsutsumi, J. Kardos, Y. Goto, F. Gejyo and H. Naiki, *Biochemistry*, 2004, **43**, 11075-11082.

67. P. G. Vekilov, *J. Phys. Condens. Matter*, 2012, **24**, 193101.
68. D. Erdemir, A. Y. Lee and A. S. Myerson, *Acc. Chem. Res.*, 2009, **42**, 621-629.
69. F. Oosawa and M. Kasai, *J. Mol. Biol.*, 1962, **4**, 10-21.
70. S. Auer and D. Kashchiev, *Proteins*, 2010, **78**, 2412-2416.
71. J. D. Harper and P. T. Lansbury, Jr., *Annu. Rev. Biochem.*, 1997, **66**, 385-407.
72. H. Yoshikawa, A. Hirano, T. Arakawa and T. Shiraki, *Int. J. Biol. Macromol.*, 2012, **50**, 865-871.
73. J. Stohr, N. Weinmann, H. Wille, T. Kaimann, L. Nagel-Steger, E. Birkmann, G. Panza, S. B. Prusiner, M. Eigen and D. Riesner, *Proc. Natl. Acad. Sci. U.S.A.*, 2008, **105**, 2409-2414.
74. C. N. Pace, S. Trevino, E. Prabhakaran and J. M. Scholtz, *Philos. Trans. R. Soc. Lond. B Biol. Sci.*, 2004, **359**, 1225-1234; discussion 1234-1225.
75. M. So, H. Yagi, K. Sakurai, H. Ogi, H. Naiki and Y. Goto, *J. Mol. Biol.*, 2011, **412**, 568-577.
76. Y. Yoshimura, M. So, H. Yagi and Y. Goto, *Jpn. J. Appl. Phys.*, 2013, **52**, 07HA01.
77. K. C. Aune and C. Tanford, *Biochemistry*, 1969, **8**, 4579-4585.
78. E. J. Cohn, L. E. Strong, W. L. Hughes, D. J. Mulford, J. N. Ashworth, M. Melin and H. L. Taylor, *J. Am. Chem. Soc.*, 1946, **68**, 459-475.
79. S. Goda, K. Takano, Y. Yamagata, R. Nagata, H. Akutsu, S. Maki, K. Namba and K. Yutani, *Protein Sci.*, 2000, **9**, 369-375.
80. Y. Yonezawa, S. Tanaka, T. Kubota, K. Wakabayashi, K. Yutani and S. Fujiwara, *J. Mol. Biol.*, 2002, **323**, 237-251.
81. M. Holley, C. Eginton, D. Schaefer and L. R. Brown, *Biochem. Biophys. Res. Commun.*, 2008, **373**, 164-168.
82. K. Y. Huang, G. A. Amodeo, L. Tong and A. McDermott, *Protein Sci.*, 2011, **20**, 630-639.
83. A. C. Ferreon, Y. Gambin, E. A. Lemke and A. A. Deniz, *Proc. Natl. Acad. Sci. U.S.A.*, 2009, **106**, 5645-5650.
84. L. Giehm, C. L. Oliveira, G. Christiansen, J. S. Pedersen and D. E. Otzen, *J. Mol. Biol.*, 2010, **401**, 115-133.
85. R. C. Rivers, J. R. Kumita, G. G. Tartaglia, M. M. Dedmon, A. Pawar, M. Vendruscolo, C. M. Dobson and J. Christodoulou, *Protein Sci.*, 2008, **17**, 887-898.
86. J. Lind, E. Lindahl, A. Peralvarez-Marin, A. Holmlund, H. Jornvall and L. Maler, *FEBS J.*, 2010, **277**, 3759-3768.
87. A. Wahlstrom, L. Hugonin, A. Peralvarez-Marin, J. Jarvet and A. Graslund, *FEBS J.*, 2008, **275**, 5117-5128.
88. S. Kumar, V. K. Ravi and R. Swaminathan, *Biochem. J.*, 2008, **415**, 275-288.
89. J. D. Bryngelson, J. N. Onuchic, N. D. Socci and P. G. Wolynes, *Proteins*, 1995, **21**, 167-195.

90. H. Nymeyer, A. E. Garcia and J. N. Onuchic, *Proc. Natl. Acad. Sci. U.S.A.*, 1998, **95**, 5921-5928.
91. Y. Lin, Y. H. Lee, Y. Yoshimura, H. Yagi and Y. Goto, *Langmuir*, 2014, **30**, 1845-1854.
92. H. Muta, Y. H. Lee, J. Kardos, Y. Lin, H. Yagi and Y. Goto, *J. Biol. Chem.*, 2014, **289**, 18228-18238.
93. M. Adachi, M. So, K. Sakurai, J. Kardos and Y. Goto, *J. Biol. Chem.*, 2015, **290**, 18134-18145.
94. W. Hoyer, T. Antony, D. Cherny, G. Heim, T. M. Jovin and V. Subramaniam, *J. Mol. Biol.*, 2002, **322**, 383-393.
95. M. Fandrich, M. A. Fletcher and C. M. Dobson, *Nature*, 2001, **410**, 165-166.
96. C. Iannuzzi, S. Vilasi, M. Portaccio, G. Irace and I. Sirangelo, *Protein Sci.*, 2007, **16**, 507-516.
97. M. Azami-Movahed, S. Shariatizi, M. Sabbaghian, A. Ghasemi, A. Ebrahim-Habibi and M. Nemat-Gorgani, *Int. J. Biochem. Cell Biol.*, 2013, **45**, 299-307.
98. G. W. Bushnell, G. V. Louie and G. D. Brayer, *J. Mol. Biol.*, 1990, **214**, 585-595.
99. S. R. Hubbard, W. A. Hendrickson, D. G. Lambright and S. G. Boxer, *J. Mol. Biol.*, 1990, **213**, 215-218.
100. W. R. Fisher, H. Taniuchi and C. B. Anfinsen, *J. Biol. Chem.*, 1973, **248**, 3188-3195.
101. Y. Goto, Y. Hagihara, D. Hamada, M. Hoshino and I. Nishii, *Biochemistry*, 1993, **32**, 11878-11885.
102. G. A. Mines, T. Pascher, S. C. Lee, J. R. Winkler and H. B. Gray, *Chem. Biol.*, 1996, **3**, 491-497.
103. P. Li, D. Nijhawan, I. Budihardjo, S. M. Srinivasula, M. Ahmad, E. S. Alnemri and X. Wang, *Cell*, 1997, **91**, 479-489.
104. G. C. Brown and V. Borutaite, *Biochim. Biophys. Acta*, 2008, **1777**, 877-881.
105. D. Hamada, M. Hoshino, M. Kataoka, A. L. Fink and Y. Goto, *Biochemistry*, 1993, **32**, 10351-10358.
106. A. Kowalsky, *J. Biol. Chem.*, 1969, **244**, 6619-6625.
107. M. Hashimoto, A. Takeda, L. J. Hsu, T. Takenouchi and E. Masliah, *J. Biol. Chem.*, 1999, **274**, 28849-28852.
108. S. Junedi, K. Yasuhara, S. Nagao, J. Kikuchi and S. Hirota, *Chembiochem*, 2014, **15**, 517-521.
109. E. Margoliash and N. Frohwirt, *Biochem. J.*, 1959, **71**, 570-572.
110. O. Daltrop and S. J. Ferguson, *J. Biol. Chem.*, 2003, **278**, 4404-4409.
111. S. C. Gill and P. H. von Hippel, *Anal. Biochem.*, 1989, **182**, 319-326.
112. A. Micsonai, F. Wien, L. Kernya, Y. H. Lee, Y. Goto, M. Refregiers and J. Kardos, *Proc. Natl.*

Acad. Sci. U.S.A., 2015, **112**, E3095-3103.
113. M. Jackson and H. H. Mantsch, *Crit. Rev. Biochem. Mol. Biol.*, 1995, **30**, 95-120.
114. Y. H. Lee, E. Chatani, K. Sasahara, H. Naiki and Y. Goto, *J. Biol. Chem.*, 2009, **284**, 2169-2175.
115. J. M. Stevens, D. A. Mavridou, R. Hamer, P. Kritsiligkou, A. D. Goddard and S. J. Ferguson, *FEBS J.*, 2011, **278**, 4170-4178.
116. T. Ikenoue, Y. H. Lee, J. Kardos, H. Yagi, T. Ikegami, H. Naiki and Y. Goto, *Proc. Natl. Acad. Sci. U.S.A.*, 2014, **111**, 6654-6659.
117. E. Y. Hayden, P. Kaur, T. L. Williams, H. Matsui, S. R. Yeh and D. L. Rousseau, *Biochemistry*, 2015, **54**, 4599-4610.
118. S. Benjwal, S. Verma, K. H. Rohm and O. Gursky, *Protein Sci.*, 2006, **15**, 635-639.
119. J. M. Alakoskela, A. Jutila, A. C. Simonsen, J. Pirneskoski, S. Pyhajoki, R. Turunen, S. Marttila, O. G. Mouritsen, E. Goormaghtigh and P. K. Kinnunen, *Biochemistry*, 2006, **45**, 13447-13453.
120. S. Haldar, P. Sil, M. Thangamuniyandi and K. Chattopadhyay, *Langmuir*, 2015, **31**, 4213-4223.
121. S. W. Chen, S. Drakulic, E. Deas, M. Ouberai, F. A. Aprile, R. Arranz, S. Ness, C. Roodveldt, T. Guilliams, E. J. De-Genst, D. Klenerman, N. W. Wood, T. P. Knowles, C. Alfonso, G. Rivas, A. Y. Abramov, J. M. Valpuesta, C. M. Dobson and N. Cremades, *Proc. Natl. Acad. Sci. U.S.A.*, 2015, **112**, E1994-2003.
122. W. E. Balch, R. I. Morimoto, A. Dillin and J. W. Kelly, *Science*, 2008, **319**, 916-919.
123. A. Mordas and K. Tokatlidis, *Acc. Chem. Res.*, 2015, **48**, 2191-2199.
124. J. Hofrichter, P. D. Ross and W. A. Eaton, *Proc. Natl. Acad. Sci. U.S.A.*, 1976, **73**, 3035-3039.
125. D. Gebauer, M. Kellermeier, J. D. Gale, L. Bergstrom and H. Colfen, *Chem. Soc. Rev.*, 2014, **43**, 2348-2371.
126. N. Asherie, *Methods*, 2004, **34**, 266-272.

List of publications

Main works

1. Lin, Y.,* Lee, Y.-H.,* Yoshimura, Y., Yagi, H., and Goto, Y.
   Solubility and supersaturation-dependent protein misfolding revealed by ultrasonication.
   Langmuir, **30**, 1845-1854 (2014)
   *Lin, Y. and Lee, Y.-H. contributed equally to this work

2. Lin, Y., Kardos, J., Imai, M., Ikenoue, T., Kinoshita, M., Sugiki, T., Ishimori, K., Goto, Y. and Lee, Y.-H.
   Amorphous aggregation of cytochrome *c* with inherently low amyloidogenicity is characterized by the metastability of supersaturation and the phase diagram.
   Langmuir, **32**, 2010-2022 (2016)

Collaborations

3. Yoshimura, Y., Lin, Y., Yagi, H., Lee, Y.-H., Kitayama, H., Sakurai, K., So, M., Ogi, H., Naiki, H., and Goto, Y.
   Distinguishing crystal-like amyloid fibrils and glass-like amorphous aggregates from their kinetics of formation.
   Proc. Natl. Acad. Sci. U. S. A., **109**, 14446-14451 (2012)

4. Muta. H., Lee, Y.-H., Kardos, J., Lin, Y., Yagi, H., and Goto, Y.
   Supersaturation-limited amyloid fibrillation of insulin revealed by ultrasonication.
   J. Biol. Chem., **289**, 18228-18238 (2014)

5. Kinoshita, M., Kim, J.Y., Kume, S., Lin, Y., Mok, K.H., Kataoka, Y., Ishimori, K., Markova, N., Kurisu, G., Hase, T. and Lee, Y.-H.
   Energetic basis on interactions between ferredoxin and ferredoxin $NADP^+$ reductase at varying physiological conditions.
   Biochem. Biophys. Res. Commun., **482**, 909-915 (2017)

6. Kinoshita, M., Kim, J.Y., Lin, Y., Markova, N., Hase, T. and Lee, Y.-H.
Biochemical and Biophysical Methods to Examine Effects of Site-directed Mutagenesis on Enzymatic Activities and Interprotein Interactions.
Methods in Molecular Biology (*In Vitro* Mutagenesis: Methods and Protocol)., **1498**, 439-460 (2017)

7. Ikenoue, T., Lin, Y., Kinoshita, M., Sakurai, K., Goto, Y. and Lee, Y.-H.
Molecular Structure of Amyloid Fibrils Revealed by Thermodynamics.
Protein-Protein Interactions (PPIs): Types, Methods for Detection and Analysis., 81-96 (2017)